The impact of atomic and electronic structure modifications on magnetoelastic coupling of epitaxial Fe films and Fe/Au/Fe trilayers investigated by stress measurements

Dissertation

zur Erlangung des
Doktorgrades der Naturwissenschaften (Dr. rer. nat.)

der

Naturwissenschaftlichen Fakultät II
Chemie, Physik und Mathematik

der Martin-Luther-Universität
Halle-Wittenberg,

vorgelegt von

FRAU KENIA NOVAKOSKI FISCHER
geb. am 16 September 1986 in Criciúma, Brazil

- PD Dr. Dirk Sander
- Prof. Dr. Wolf Widdra
- Prof. Dr. Reinhold Koch

Verteidigt am: 02 Februar 2018

Abstract

Epitaxial atomic layers are often in a strain-state, which is determined by the lattice misfit to the substrate. This misfit gives rise to a biaxial stress state within the film, and it contributes significantly to the magnetic anisotropy via magnetoelastic coupling. Film stress induced by lattice strain and magnetoelastic stress upon magnetization of a ferromagnetic film are experimentally accessible by the minute stress-induced curvature of a thin substrate. The cantilever bending technique is an experimental method to measure film stress with high sensitivity and accuracy. In this work I use an optical beam deflection technique to measure the stress during epitaxial growth of atomic layers and the magnetoelastic stress of nm thin films upon a magnetization reorientation. This thesis presents the first observation of stress change during deposition of a transition metal on the topological insulator Bi2Se3(0001). The film stress varies with growth temperature. Surface analysis by diffraction experiments indicates the formation of FeSe nanocrystals on Bi2Se3. Surprisingly, the driving force for the stress change during formation of FeSe on Bi2Se3 is the structural and atomic re-arrangement upon nanocrystal formation, rather than misfit strain. I measure film stress during the deposition of Fe on Au and Ag single crystal substrates with an (001) surface orientation. I study the influence of thickness, lattice strain, and interface formation on the magnetoelastic coupling of Fe films with few monolayer thickness. I use the stress measurements to monitor interface formation, intermixing, segregation and to explore the impact of quantum well states in a nonferromagnetic spacer layer on magnetoelasticity in adjacent Fe layers. A novel approach to control the magnetoelastic coupling of a thin film by modifying its surface and interface structure by noble gas ion bombardment is presented. An important result of this thesis is discovery of a non-monotonic, almost oscillatory variation of magnetoelastic coupling in Fe films upon variation of the Au spacer layer thickness in the Fe/Au/Fe/Au(001) system. This result is discussed in view of quantum well states (QWS) in the Au spacer layer. These results provide new and first insights into the correlation between electronic confinement and magnetoelastic properties on the nanoscale.

Kurzfassung

Epitaktische Atomlagen sind oftmals in einem Dehnungszustand, der durch die Gitterfehlpassung zum Substrat gegeben ist. Diese Dehnung führt zu einer biaxialen Filmspannung. Diese Dehnung trägt maßgeblich zur magnetischen Anisotropie der Atomlage, vermittelt durch die magnetelastische Kopplung, bei. Filmspannungen beim Wachstum und magnetoelastische Spannungen bei Magnetisierungsänderungen sind experimentell zugänglich durch die von ihnen verursachte Krümmung dünner Substrate. Die Biegebalkenmethode erlaubt es, diese Spannung sehr empfindlich und genau zu messen. In dieser Arbeit wird eine optische Biegebalkenmethode eingesetzt, um Filmspannungen beim epitaktischen Wachstum von Atomlagen und magnetoelastische Spannungen von Nanometer-dünnen Filmen zu messen. In dieser Arbeit werden die ersten Messungen von Filmspannungen beim Abscheiden von Fe auf dem topologischen Isolator Bi2Se3(0001) vorgestellt. Die Filmspannungen hängen sehr stark von der Substrattemperatur beim Abscheiden ab. Die Oberflächenanalyse mit Beugungsmethoden zeigt die Bildung von FeSe Nanokristallen auf Bi2Se3. Überraschenderweise stellen hier strukturelle Umordnungen und atomare Reorganisation während des Abscheidens die Hauptursache für die Fe-induzierten Spannungen dar, während die Fehlpassung die gemessenen Spannungen nicht erklären kann. Ich messe die Filmspannungen während des Wachstums von Fe auf Au- und Ag-Einkristallen mit (001) Oberflächenorientierungen. Ich untersuche dabei den Einfluss von Filmdicke, Gitterdehnung und Grenzflächenbildung auf die magnetoelastische Kopplung der Fe-Filme der dicke einiger Atomlagen. Ich nutze die Spannungsmessung um die Grenzflächenbildung, Interdiffusion, Segregation und den Einfluss von Quantentrogzuständen in nichtferromagnetischen Zwischenschichten auf die Magnetoelastizität benachbarter Fe-Lagen zu charakterisieren. Ein neuer Ansatz zur Beeinflussung der magnetoelastischen Kopplung in dünnen Filmen durch Modifikation von Oberflächen und Grenzflächen durch Ionenbeschuss mit Edelgasen wird vorgestellt. Ein wichtiges Ergebnis meiner Arbeit ist die Entdeckung einer nichtmonotonen, fast oszillatorischen, Änderung der magnetoelastischen Kopplung in Fe- Atomlagen durch die Variation der Schichtdicke einer Au-Zwischenlage im System Fe/Au/Fe/Au(001). Das Ergebnis wird im Bild von Quantentro-

gzuständen in der Au- Zwischenschicht diskutiert. Diese Ergebnisse liefern neue und erste Einblicke in die Korrelation zwischen elektronischen Quantentrogzuständen und Magnetoelastizität auf der Nanoskala.

Contents

Chapter 1

Introduction

The study of magnetic properties of ultrathin films has been the focus of intensive research in the past few decades. It brought significant contributions to the understanding of the physical mechanism which led to the developments of magnetic random-access memory and high-density magnetic storage [1–4]. The magnetic anisotropy plays a key role for the magnetic properties of thin films. The magnetic properties of thin films often deviate from the bulk behavior. This deviation is due to the low dimensionality of the system, where the formation of interfaces and growth-induced lattice strain impact magnetism [5,6].

As films become thinner the overall properties are more governed by interface and surface properties, this is evident in multilayer systems [7–10]. Furthermore, thin films are usually supported by a substrate, which leads to film stress due to epitaxial strain induced by lattice mismatch. Epitaxial strain in a thin film is the origin for a large contribution to the total magnetic anisotropy, as induced by magnetoelastic coupling. Magnetoelastic coupling is responsible for magnetostriction, i.e. the change of length of a sample upon magnetization, and this phenomenon opened new possibilities for applications as sensors and actuators [11–19].

It has been found that the specific atomic structure and elemental composition at the interface of thin films influence drastically their magnetic properties. Here, alloys of transition metals, such as Fe-Ga, show an increased magnetostrictive response [20, 21], where an elastic softening upon alloy formation is a new aspect.

In this thesis, I study the influence of interface/surface effects and lattice strain of atomic layers on the magnetoelastic coupling of films with few monolayer thickness. Several phenomenological models have been proposed to explain experimental observations of magnetoelasticity of thin films, due to the presence of surface effects on the magnetoelastic coupling coefficient [22, 23],

but most fail to explain the change of sign or deviation from the bulk value of magnetoelastic coupling coefficients [22]. A lattice strain-dependent correction was proposed, giving a favorable description of some systems [24, 25]. However, it cannot be generalized [26]. Therefore, further experimental data are called for to obtain a broader picture of the properties which impact magnetoelasticity of thin films.

The stress change in a thin film can be experimentally accessed by the cantilever bending beam technique [27–29]. The detection is based on the optical deflection of a single laser beam, or of several lasers beams, reflected off the cantilever surface. It is a very sensitive technique to measured films stress and magnetoelastic stress driven down to the monolayer thickness regime [30]. This is the main technique employed in my thesis. I exploit this method to measure the epitaxial stress during film growth and the change of stress induced by a switching of the magnetization direction in the films to measure magnetoelastic coupling coefficients.

Chapter 4 of this thesis presents the first observation of stress change during deposition of a transition metal on the topological insulator $Bi_2Se_3(0001)$. The atomic structure and electronic properties of Bi_2Se_3, including a prominent topological insulator character, are well known [31, 32]. Here, I investigate deposition of Fe on Bi_2Se_3 by cantilever stress measurements for different growth temperature. Additional surfaces analysis techniques were employed to understand the origin of the stress change. FeSe nanocrystals on Bi_2Se_3 are formed. Surprisingly, the driving force for the stress change during formation of FeSe on Bi_2Se_3 is the structural and atomic arrangement rather than the simple epitaxial stress.

Chapters 5 and 6 focus on systems, which present complicated growth processes, but are composed of single metals, Fe/Ag(001) and Fe/Au(001). The complicated interface formation in these systems has been studied in depth in recent years [33–43]. Also, Fe/Ag(001) and Fe/Au(001) are prototypes for modified magnetic and electronic properties of thin films as driven by quantum well states [9, 10, 44–47]. I use the epitaxial stress results as an indicator to optimize the interfaces and film flatness in order to study interlayer exchange coupling and quantum well states. In this thesis, a novel approach to control the magnetoelastic coupling of a thin film by modifying its surface and interface structure is introduced. For this purpose, the thermal induced interface intermixing is studied.

An important result of this thesis is the remarkable oscillatory magnetoelasticity in Fe films upon variation of adjacent Au layer in the trilayer Fe/Au/Fe. This result is described to quantum well states (QWS) in the Au spacer layer of the prototype system Fe/Au/Fe.

Our results provide new insights into a correlation between electronic

confinement and magnetoelastic properties. This has never been observed before. The results presented in this thesis shed new light onto a fundamental understanding of the magnetoelatic property of strained thin films and multilayers on the electronic level.

The thesis is organized as follows. Chapter 2 illustrates introductory basic theoretical concepts of film stress and magnetoelastic coupling. The concepts involved in the interlayer exchange coupling of ferromagnetic (FM) / nonmagnetic (NM) / ferromagnetic (FM) system modulated by QWS in the NM layer are elucidated. Chapter 3 describes the methods and techniques used in this work. The first experimental determination of Young's modulus of Bi_2Se_3 is presented. The preparation of samples for the systems used in this thesis are described. The experimental results are presented in Chapters 4, 5, 6, and 7. Chapter 4 presents the results on stress and structure of Fe and FeSe on $Bi_2Se_3(0001)$. Experimental results of Fe on Ag(001) follow in Chapter 5, where structural and magnetic properties are presented. Chapter 6 presents the results of Fe on Au(001), with structural and magnetic investigations in order to gain insights into the correlation of epitaxial strain and magnetic behavior. Chapter 7 focuses on the results on the trilayer Fe/Au/Fe on Au(001). The first measurement of stress change upon formation of the Au surface reconstruction during film growth is presented. Chapter 7 also reports the results of the magnetoelastic coupling (ME) and magnetic-crystalline anisotropy (MA) of Fe/Au/Fe trilayers. Experimental evidence for periodic oscillations of MA and ME, induced by the QWS, is presented. This provides the first experimental indication of the influence of electronic confinement on the magnetoelasticity of thin films. All experimental results are thoroughly discussed in Chapter 8, and conclusions and future prospects are presented in Chapter 9.

Chapter 2

Basic concepts and background

In this chapter I present the physical concepts which are exploited in this work. Epitaxial growth and the interfacial structure formed in thin films influence their magnetic properties. In this thesis, I investigate the structure and interface formation of ferromagnetic thin films on a metallic substrate via stress change. With this purpose, Section 2.1 presents an overview understanding of elastic properties, strain and stress, in epitaxial film growth.

The magnetic properties of these films were studied in view of the epitaxial strain and interface formation. Here, I focus on the magnetoelastic coupling of thin films and the interlayer exchange coupling in a trilayer system. In Section 2.2, I detail the magnetoelastic concepts and the relation between magnetoelastic coupling in thin films and the magnetostriction effect described for bulk samples. Finally, Section 2.3 introduces the intelayer exchange coupling (IEC) effect in a trilayer system composed by ferromagnetic(FM) / nonmagnetic(NM) / ferromagnetic(FM) materials.

2.1 Stress and strain in epitaxial ultrathin films

The concepts of solid surfaces and interfaces are the starting point to define stress and strain. The interface is the boundary region between two regions occupied by different materials. It is defined by a small number of atomic layers in spatial contact, where properties deviate from the respective bulk materials. A particular type of interface in a solid is its surface, which separates the material from the surrounding environment.

A film deposited on a substrate has a solid-solid and a solid-vacuum interface. For films in the single atomic layers thickness regime the properties of the film may be determined by the properties of its interfaces. The thermodynamic description of surfaces was developed by Gibbs [48], he was the

first to point out the difference of surface stress and surface free energy.

The surface free energy γ is the excess free energy associated with the existence of a surface. It is described as the reversible work per area to create a surface. On the other hand, surface stress $\tau^{(s)}$ is determined by the reversible work per area to stretch elastically a pre-existing surface.

2.1.1   Surface stress

To obtain a proper definition of surface stress in a crystalline solid, the tensorial elastic properties should be considered. In a highly symmetric surface, the surface stress is isotropic and can be expressed as [49]

$$\tau_{ij} = \frac{\partial f_i}{\partial a_j}, \tag{2.1}$$

where ∂f_i is the differential force along i direction and ∂a_j is the area element normal in j direction.

The relation between surface stress and surface free energy is given as [49]

$$\tau_{ij}^{(s)} = \gamma \delta_{ij} + \frac{\partial \gamma}{\partial \epsilon_{ij}}, \tag{2.2}$$

where ϵ_{ij} is the strain tensor with i and j as the in-plane components and δ_{ij} is the Kronecker symbol.

In contrast to the surface free energy, which is positive, the surface stress can assume positive and negative values. A positive stress is referred as "tensile" stress, and the negative surface stress is called "compressive" stress. The sign of the stress depends on whether the surface tends to contract (tensile), where the surface atoms prefer a shorter bond length than in bulk, or expand (compressive), surface atoms repel each other under its own stress. The calculated surface stress of transition metals are often positive (tensile) [49].

The interplay of surface free energy and surface stress rules the characteristics of surface in a solid, from Eq. 2.2, the term $\partial \gamma / \partial \epsilon \;=\; \tau^{(s)} - \gamma$ is the thermodynamic driving force to move atoms from bulk to surface layers. Therefore, if the right term is positive the accumulation of atoms on the surface is favored in comparison to the inner arrangement. On the other hand, when the term is negative the surface prefers less atoms in the top layers. Moreover, a large surface stress may cause instabilities on the surface such as reconstructions [49, 50]. A reconstruction refers to the atomic configuration of the surface that differs from the atomic structure of the bulk.

However, in a solid-solid interface of crystalline materials the film stress is often driven by the lattice misfit of the materials. This concept is important to understand film stress in epitaxial films on a substrate.

2.1.2 Epitaxial film

The epitaxial growth is the notion that a material grown on a substrate follows the crystalline order of the substrate in a specific, well defined relation. Pseudomorphic growth, i.e. the continuation of the substrate crystalline order in the films, yields a lateral strain in the film. The strain is given by the misfit between the atomic lattices of film and substrate. The in-plane misfit (η) is calculated from the in-plane atomic distances (a) of the bulk of the substrate with reference to the film bulk material as

$$\eta = (a_{\mathrm{S}} - a_{\mathrm{F}})/a_{\mathrm{F}}, \tag{2.3}$$

where a_{S} represents substrate atomic distances and a_{F} describes the film atomic distances.

Epitaxial growth, however, is not always possible, and a large lattice mismatch may induce dislocations in the film. Dislocations may minimize the elastic energy of the film lattice. For a low lattice misfit the elastic strain is sustainable to form a lattice of the epitaxial film. This in-plane strain results in an induced stress in the film. When the lattice constant of the material in the film (a_{F}) is smaller than the lattice constant of the substrate (a_{S}), it gives rise to a positive strain, consequently a tensile stress in the film. On the other hand, for the case that the lattice of the material of the film (a_{F}) is bigger than the substrate lattice (a_{S}) the strain is negative, which results in a compressive stress in the film. If the substrate is thin enough, the stress in the film is transferred to the substrate where it induces a measurable curvature. The curvature can be measured as presented in Section 3.1. Figure 2.1a and b are illustrations of the curvature condition for a compressive and a tensile film stress. It is observed that pseudomophic growth is possible in several atomic layers thin films provided the misfit is below a few percent [50].

In an isotropic in-plane strain $\eta = \epsilon_1 = \epsilon_2$ (the indices 1 and 2 correspond to the in-plane directions) the biaxial epitaxial stress can be calculated by the linear elastic theory as [51]:

$$\tau = \frac{Y}{1 - \nu}\eta, \tag{2.4}$$

where Y is the Young's modulus and ν is the Poisson ratio of the film, here the ratio $Y/(1-\nu)$ determines the rigidity of the film material.

However, in a real system the stress during growth involves other effects besides misfit stress. For example, in a submonolayer regime, a contribution from the change in surface stress is expected. The variation on surface stress depends on the surface stress of the substrate τ_{s}, the surface stress of the new
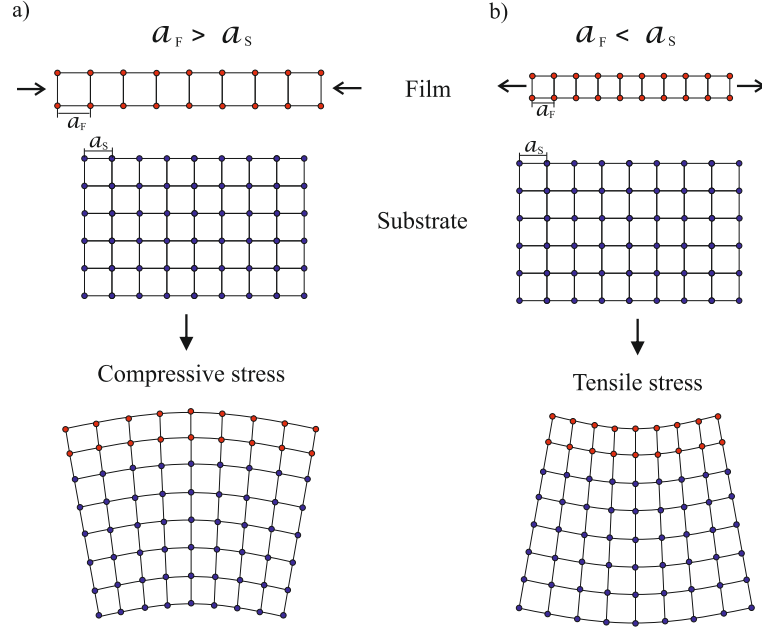
Figure 2.1: Illustration of film stress due to the difference in lattice constants of film (red) and substrate (blue) in a compressive stress and a tensile stress, and the induced bending of a thin substrate. a) compressive stress, $\eta < 0$; b) tensile stress, $\eta > 0$.

film/substrate interface $\tau_{\text{f-s}}$, and the film surface stress τ_{f} as $\tau_{\text{f}}+\tau_{\text{f-s}}-\tau_{\text{s}}$. Stress measurements during film growth reveal dislocation formation [52], change of growth mode [51], and reconstructions [53]. I use stress measurements to investigate the relevant processes during growth.

In this thesis, I used the bending technique of a cantilever substrate to investigate the stress involved during growth. I choose systems that present segregation and/or interdiffusion during the growth process. Corresponding stress measurements have not been reported in the literature before. I studied the deposition of Fe on Ag(001) and Fe on Au(001). These systems were selected as a wealth of previous investigations is available [34–43,54–62]. Besides, I measured the change of surface stress for a submonolayer deposition of Fe on Bi_2Se_3(0001). The Bi_2Se_3(0001) crystal has a specific crystalline structure of quintuple layers of Se-Bi-Se-Bi-Se bonded with other quintuple layers by van-der-Waals interaction. This structural peculiarity make Bi_2Se_3 a very attractive system to measure stress during deposition in view of possible intercalation of Fe [63].

2.2   Magnetoelastic coupling in thin films

The magnetic anisotropy energy of a magnetic crystal in a strained state is described by the magnetoelastic energy. The magnetoelastic energy arises from the interplay of lattice strain and magnetization. In an unstrained lattice this term is zero, which results in an anisotropy energy given by the crystal symmetry [64]. The magnetoelastic energy represents the interaction between the magnetic anisotropy and strain of the crystal. According to Kittel [65], the magnetoelastic energy density for a cubic system is defined as, where higher order terms are omitted [51]:

$$f_{\mathrm{me}} = B_1(\epsilon_1 \alpha_1^2 + \epsilon_2 \alpha_2^2 + \epsilon_3 \alpha_3^2) + B_2(\epsilon_4 \alpha_2 \alpha_3 + \epsilon_5 \alpha_1 \alpha_3 + \epsilon_6 \alpha_1 \alpha_2)...., \quad (2.5)$$

where ϵ_i is the strain along the cubic axes and α_i is the direction cosine of the magnetization direction with respect to the crystallographic direction. Here we use the contracted Voigt notation [51]. B_1 and B_2 are the first order magnetoelastic coupling coefficients. The higher-order terms in α_i have been neglected in this work. Higher order terms in strain ϵ_i are discussed below in the ME models. The magnetoelastic coupling coefficients, B_1 and B_2, represent the strain gradient of the magnetic anisotropy energy density.

This contribution is to minimize the total energy by a lattice deformation. This is known as magnetostriction of bulk materials. The resulting magnetostrictive strain is described by the magnetostriction constant λ as $\Delta l/l$, where l is the length along the direction of the magnetization, and Δl the change of length along a given direction upon a reorientation of magnetization.

Thus, the magnetostriction constant λ in a cubic crystal depends on the cubic axis as λ_{100} and λ_{111}. The indices determine the longitudinal magnetostriction along the directions [100] and [111], respectively. The magnetostrictive constants λ_{100} and λ_{111} are proportional to the magnetoelastic coupling coefficients B_1 and B_2 as follow,

$$\lambda_{100} = -\frac{2}{3}\frac{B_1}{(c_{11} - c_{12})} \quad \text{and} \quad \lambda_{111} = -\frac{1}{3}\frac{B_2}{c_{44}}, \quad (2.6)$$

where c_{ij} are the elastic stiffness constants of the bulk material. Note that λ depends on the elastic properties of the crystal. A small $c_{11} - c_{12}$ may lead to a large λ even for a moderate B_1 [20, 21, 66].

The typical experimental values of λ for the ferromagnetic elements Fe, Co, and Ni, are of the order of 10^{-6} [65], which corresponds to a change of a few μeV/atom on the anisotropy energies. Therefore, due to its small magnitude, calculations on the magnetoelastic properties are demanding [67].

Table 2.1: Elastic stiffness constants c_{ij} (GPa) , magnetostrictive constants λ_{100} and λ_{111} and its respective magnetoelastic coupling coefficient B_i (MJ/m^3) of Fe bulk. Values obtained from Ref. [51].

	c_{11}	c_{12}	c_{44}	λ_{100}	λ_{111}	B_1	B_2
bcc Fe	229	134	115	24.1	-22.7	-3.43	7.83

Using the experimental results of λ and the relation of Eq. 2.6 the magnetoleastic coupling coefficients B_1 and B_2 for bulk sample are calculated from magnetostriction measurements.

For bcc Fe bulk the elastics constants and magnetoelastic coefficients are presented in Table 2.1. The negative sign of B_1 means that an expansion of the Fe lattice upon magnetization along the [100] direction of the cubic axis is energetically favorable.

However, the magnetic properties of thin films deviate from the bulk behavior, and the values obtained above can hardly be applied [68]. The main reason behind the different behavior is that films are often under a considerable lattice strain, due to the contact with the substrate. Generally, films cannot change their in-plane atomic distances freely due to the bond to the substrate. Consequently in a thin film, upon a magnetization process the magnetoelastic coupling (ME) leads to a magnetoelastic stress and not to a magnetostrictive strain. Therefore, the term "magnetostriction" should be avoided when discussing magnetoelastic properties of films. Thus, the magnetoelastic coupling coefficient are the proper reference. The magnetoelastic stress is defined as the strain derivative of the magnetoelastic energy density ($\tau = \partial f_{me}/\partial \epsilon$).

Magnetoelastic stress, the tendency of the film to change its length upon magnetization, is phenomenologically comparable to magnetostriction of bulk materials, as demonstrated in Fig. 2.2a and b.

Experimentally the magnetoelastic stress can be measured by a stress change upon a reorientation of the magnetization direction, as induced by external magnetic fields [67]. In a film, this stress induces a curvature of the substrate, provided the substrate is thin enough. The use of a thin substrate provides a way to obtain experimentally the stress involved in the process and, therefore, the value of B_i is accessible as described below.

As the magnetoelastic coupling energy depends on the directions of the magnetization with respect to the cubic axis, Eq. 2.5, the magnetization is applied in two equivalent directions. For this reason, to access B_1 the magnetization is aligned parallel to the direction [100] and [010], see Fig. 2.3a. This gives $\alpha_1 = 1$, $\alpha_2 = 0$, and $\alpha_3 = 0$ for [100], and $\alpha_1 = 0$, $\alpha_2 = 1$, and
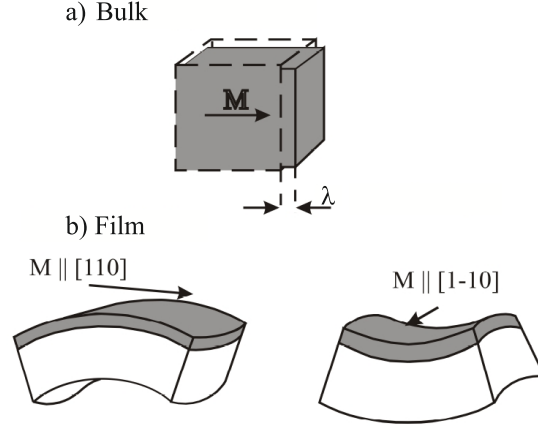
Figure 2.2: Magnetoelastic coupling in a) bulk sample, where $M \neq 0$ induces a magnetostrictive strain λ. b) magnetic thin film on a substrate, due to the bonding on the substrate, $M \neq 0$ induces a magnetoelastic stress, which induces a bending of the crystal (film and substrate).

$\alpha_3 = 0$ for [010]. Eq. 2.5 is reduced to

$$f_{\mathrm{me}} = B_1(\epsilon_1), \tag{2.7}$$

for each direction. As $\tau = \partial f_{\mathrm{me}}/\partial \epsilon$, in this configuration $\tau_1 = B_1$ and B_1 is found with

$$\Delta \tau = \tau_{\mathrm{me}}^{||[100]} - \tau_{\mathrm{me}}^{||[010]} = \frac{\partial f(M||100)}{\partial \epsilon_1} - \frac{\partial f(M||010)}{\partial \epsilon_1} = B_1. \tag{2.8}$$

One can access B_2 in a similar way, provided the magnetization directions are changed accordingly, as sketched Fig. 2.3c. A transformation matrix is necessary to obtain the strain on the new coordinates (ϵ'), which are rotated by 45°. In this case the magnetization is aligned parallel to the plane [110] and [1$\bar{1}$0], which lay along the length and width of the rectangular crystal, Fig. 2.3b. This results in $\alpha_1 = 1/\sqrt{2}$, $\alpha_2 = 1/\sqrt{2}$, and $\alpha_3 = 0$ and $\alpha_1 = -1/\sqrt{2}$, $\alpha_2 = 1/\sqrt{2}$, and $\alpha_3 = 0$ for [110] and [1$\bar{1}$0], respectively. Likewise B_2 is found with

$$\Delta \tau = \tau_{\mathrm{me}}^{||[110]} - \tau_{\mathrm{me}}^{||[1\bar{1}0]} = \frac{\partial f(M||110)}{\partial \epsilon'} - \frac{\partial f(M||1\bar{1}0)}{\partial \epsilon'} = B_2. \tag{2.9}$$

Consequently, the magnetoelastic coupling coefficients B_1 and B_2 are experimentally accessed directly by measuring the change of stress upon changing the magnetization direction in-plane.
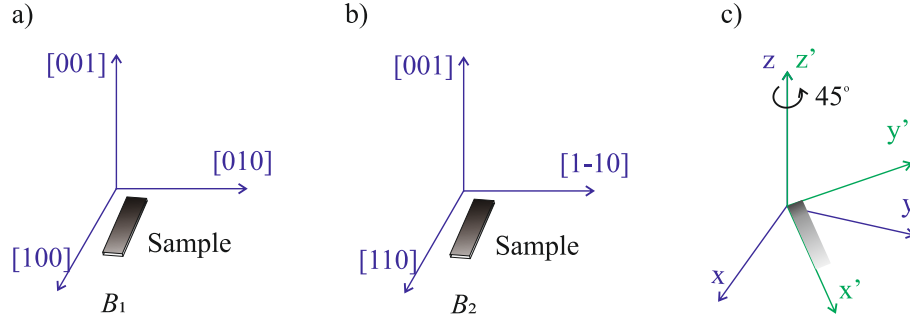
Figure 2.3: Geometry configuration of magnetoelastic coupling coefficients measured in this work. The crystal with its length and width parallel to a) [100] and [010] directions of the crystal axes of the film is used to obtain B_1. b)alignment along [110] and [$1\bar{1}0$] directions of the crystal axes is used to obtain B_2. c) rotation around [001] by 45° transfers (a) to (b).

In the past years several methods and techniques were developed to measure magnetoelastic samples. Direct and indirect methods have been proposed [27,69,70]. The indirect methods are based on the Villari effect [64], which is the inverse of magnetostriction. The basic idea is to apply an external strain in the sample and measured the change in the magnetic anisotropy [71]. Direct methods exploit the magnetostrictive strain in bulk samples as a function of applied magnetic field [27]. These techniques give the magnetostrictive coefficient λ, which includes the elastic response of the material [72]. Common techniques to measure magnetostriction are the strain gauge in bulk samples [12] and the cantilever technique for film-substrate composites [73]. Upon changing the magnetization direction induced by an external magnetic field the change of length or curvature can be detected by the change in the resistance [12], capacitance [74] or by detecting the reflection angle of an optical beam [19].

In this thesis, I exploit the cantilever technique to measured the change in curvature induced by magnetoelastic stress. The change in curvature is measured via a change of deflection of two laser beams. The difference of the curvature measured for two different magnetization orientation gives directly the magnetoelastic coupling coefficient B. Further technical details are given in Section 3.1. The advantages of this method, besides the direct access to the value of the magnetoelastic coupling coefficient B_i, are the sensitivity and the non-intrusive character. The measurements can be made in ultra-high vacuum without any mechanical contact with the sample with an astonishingly high sensitivity for detecting small curvature with a radius of curvature

as larger as several 100 km [51].

On the other hand, the theory of ME in thin films is very demanding. *Ab-initio* calculations are exploited to access the magnetoelastic effects in a perturbative manner [69]. However, a reasonable magnetoelastic coupling coefficients is hard to calculate, due to very high demands on the numerical accuracy [73]. Several simplistic models have been proposed in the past years to tackle magnetoelasticity.

A surface effect based on Néel's model proposes a volume and surface contribution to the effective ME coefficient as $B^{\text{eff}} = B_{\text{bulk}} + B_{\text{s}}/t$. This model reveals a bulk contribution for larger thickness, and an increasing contribution of the surface contribution for thin films [23, 75]. A strain-dependend correction of magnetoelastic coupling of thin film has been proposed to describe the systems where a change of ME sign is observed. This correction is described by $B_{\text{i}}^{\text{eff}} = B_{\text{i}} + D\epsilon$ [72]. This linear relation of ME with film strain, which corresponds to a second order strain contribution in Eq. 2.5 above, can be applied for several systems [22, 24–26, 76–78]. However, these phenomenological models could no be generalized. Experimental observations fail to reveal this linear dependence with film strain or the expected bulk value for thicker film [26, 79–81].

A huge increase of the magnetostrictive response has been observed for alloys of Fe with different rare earths [80, 81]. This results are attributed to a transfer of large spin-orbit coupling (SOC) to Fe in combination with the already large ME coupling of rare earth elements. In fact, rare earth metals like Tb and Dy present magnetostricitve response (λ) several orders of magnitude larger than 3d transition metals [82].

Recently, the discovery of giant magnetostrictive effect boosted a wide discussion on Fe-Ga based alloys [20, 66, 83]. The increased magnetostriction is based on elastic modifications via structural changes. More specifically, this large magnetostriction of Fe-Ga alloys has been attributed to the change of elastic constants of the Fe film with increasing Ga concentration [66, 84]. Thin films of a Co-Fe alloy have shown such increase in magnetostriction by varying the temperature of the sample [85, 86]. The combination of Fe-Ga based alloys with rare earth metals or with multifunctional materials, like ferroelectrics, gains much attention due to its potential for applications [11–16]. The magnetostrictive materials are normally used as actuators and sensors [17–19], and new materials or compounds are explored [14, 15, 78, 87, 88].

The main purpose of this work is to realize a direct modification of the magnetoelastic coupling of thin film by interface and surface changes and by electronic-modulation. I focus on systems with well know magnetic anisotropies, allowing to decouple the analysis from further effects.

In the next Chapters, I present results that reveal several effects, which

greatly impact the ME of a thin film. Substrate-induced effects that go beyond the change of strain are presented. I discuss the role of interfacial intermixing and surface segregation. A novel approach to influence the magnetoelastic coupling through quantum confinement states (QWS) is revealed in this thesis. A well established impact of electronic effects on magnetic properties is observed for the interlayer exchange coupling (IEC) of trilayers and multilayers. An oscillatory IEC is attributed to the modulated electronic states by quantum confinement effects. Next I focus on the basic aspects of oscillatory IEC in trilayer system of ferromagnetic/ nonmagnetic/ ferromagnetic (FM/NM/FM).

2.3 Interlayer exchange coupling of a trilayer system

In this Section, I briefly discuss the basic mechanisms of interlayer exchange coupling (IEC) between two ferromagnetic films separated by a non-magnetic spacer material. The essential effect has been attributed to the electronic confinement in the spacer layer. This confinement effect gives rise to sharp changes in the electronic density of states (DOS), called quantum well states (QWS). Essentially, QWS in the spacer layer couple the adjacent magnetic layers on both sides, despite that no direct contact exists. Since the nature of the effect is related to a quantum size effect, an oscillatory magnetic response is observed by varying the spacer layer thickness [89].

The antiferromagnetic coupling of Fe films separated by Cr spacer layer was first observed by Grünberg in 1986 [2], since then, the phenomenon has been intensely investigated [7, 90–95]. The discovery of the oscillatory ferromagnetic/antiferromagnetic character of the magnetization with increased spacer layer thickness is a key aspect for the development of storage devices used nowadays [1–4].

The interlayer exchange coupling takes place between two ferromagnetic layers separated by a non-magnetic material. Here, the electrons of the spacer layer mediate such a coupling. This type of interaction is referred to on the basis of the interlayer exchange coupling energy. The exchange coupling energy per unit area of two layers is described by [96]:

$$E_{AB} = -J_{AB}\mathbf{M}_\mathrm{A} \cdot \mathbf{M}_\mathrm{B} = -J_{AB}\cos\theta, \qquad (2.10)$$

where J_{AB}, or J_1, is the interlayer exchange coupling constant, $\mathbf{M}_\mathrm{i}$ are the unit vectors of magnetization direction in both layers i, A and B, and θ is the angle between the magnetic moments of layers A and B. This J_{AB} term is

called bilinear as it gives the highest coupling energy for a collinear alignment of $\mathbf{M}_A$ and $\mathbf{M}_B$, where either the parallel or the antiparallel configurations is energetically preferred.

A positive value of J_1 favors the parallel alignment of the magnetic layers and a negative J_1 favors antiparallel configuration. A perpendicular alignment of the magnetic layer has also been observed [97]. This configuration requires an additional term to minimize the energy. A biquadratic term has been introduced as follows [98]:

$$E = -J_2 \cos^2\theta = -J_2(\mathbf{M}_A \cdot \mathbf{M}_B)^2. \qquad (2.11)$$

For a positive J_2, the term favors a minimum for the relative alignment as J_1. A negative J_2, favors a perpendicular magnetization orientation of $\mathbf{M}_A$ and $\mathbf{M}_B$.

Various theoretical models have been proposed to explain the observation of interlayer exchange coupling. IEC is accessible in experiments as oscillations of magnetization orientation between two ferromagnets [34, 92, 95]. Among the most relevant models are the free electron model, the hole confinement, Ruderman-Kitter-Kasuya-Yosida (RKKY) model, the s-d mixing model, and the quantum interference model due to spin dependent reflection at the interfaces, summarized in Ref. [93].

In most models, it is assumed that the IEC-oscillations are mediated by modulations on the electronic states due to quantum well states within the non-ferromagnetic spacer layer. The period of these oscillations are determined by topological characteristics of the Fermi surface of the spacer material.

Quantum well states as a mediator of IEC

The interlayer exchange coupling can be described in terms of quantum interferences. These quantum interferences result from spin-dependent reflections of electron waves at the ferromagnetic(FM)/non-magnetic(NM) interfaces.

In a ferromagnetic material the majority- and minority-spin electrons are no longer equivalent. The difference of spin character gives rise to an energy split in the electronic states of the ferromagnetic material. This split results in a selective spin reflection at the interface FM/NM. For a ferromagnetic/noble metal interface the quantum interferences are spin dependent and are mostly of minority-spin ($\downarrow$) character, as seen in experiments [34]. The quantum effect can be understood from the electronic band structure at the interface.

Figure 2.4 shows a typical example of electronic band structures of a ferromagnetic (Co(001)) and a noble metal (Cu(001)) near the Fermi energy. In
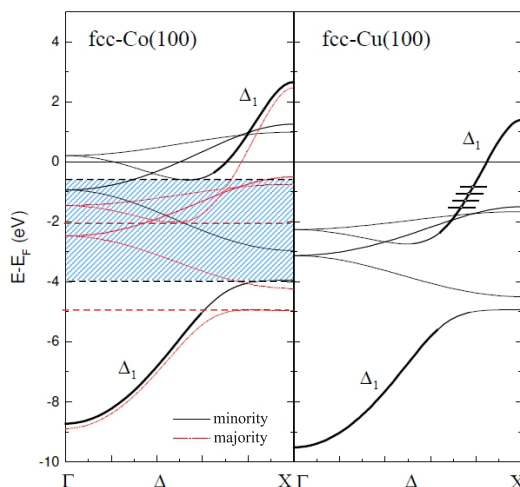
Figure 2.4: Electronic bands of bulk fcc Co(100) and Cu(100). The hybridization of the *sp*-band in the ferromagnetic material leads to a Δ_1 symmetry gap. The minority spin from the noble metal encounter this gap near the E_F and reflect, leading to a polarized QW. This system can be generalized for others ferromagnetic/noble metal interfaces. Figure adapted from [99].

the ferromagnetic material the *sp*-band hybridizes with the *d*-band, opening a Δ_1 symmetry gap. The gap region is highlighted with a light blue color in Fig. 2.4. At the interface, electrons of *sp*-character with Δ_1 symmetry in the noble metal find this gap [34]. This gap affects only the minority spins ($\downarrow$) (black curve) leading to reflections of minority spins at the interface. The QWS in Cu are identified with the horizontal lines near Fermi level in Fig. 2.4. The majority spins ($\uparrow$) Δ_1, on the other hand, couple to the majority Δ_1 band of Co near the Fermi level, and no quantum size effect is experienced by the majority spins.

If we consider an 1D-model to describe IEC, the quantum problem is reduced to a particle-in-a-box model for the minority electrons. The resulting interferences within the spacer layer induce changes in the density of states [93]. The system is composed of a sandwich of $FM_1/NM/FM_2$, where FM is a $3d$ transition metal and NM is a noble metal. An electron characterized by a wave vector $k_\perp$ that travels in the space, in a complete round trip (forth and back) gives rise to a phase shift,

$$\Delta\phi = 2k_\perp D + \phi_1 + \phi_2, \tag{2.12}$$

where D represents the thickness of the spacer, and $\phi_{1,2}$ are the phase shifts after the reflection at each interface. These interferences can be constructive

or destructive. The bound states, where the electron tends to remain localized due to confinement, occur when the interferences are constructive. A constructive interference is satisfied when [89, 100],

$$2k_{\perp}D + \phi_1 + \phi_2 = 2\pi n, \qquad (2.13)$$

where n is an integer.

The strength of the electron confinement is determined by the product of reflection amplitudes at both interfaces. For a total confinement the product is 1 [93]. The change of density of states depends on this confinement strength, as well as on the magnitude of D. The period Λ of the oscillations, on the other hand, depends only on the wave vector $k_{\perp}$ as $\Lambda = \pi/k_{\perp}$. For a three dimensional layered system, the 3-D vector $\mathbf{k} = (k_{\perp}, \mathbf{k}_{\parallel})$. $\mathbf{k}_{\parallel}$ is an arbitrary wave vector, and $k_{\perp}$ obeys the confinement condition. In a constructive interference $k_{\perp}$ is quantized.

As mentioned before, the period of oscillations corresponds to a given wave vector $k_{\perp}$. The prediction of the Λ can be done by an inspection of the Fermi surface of the spacer layer. The Fermi surface of noble metals can be experimentally obtained by highly accurate cyclotron resonance experiments [89] and angular-resolved photoelectron spectroscopy (ARPES) [101].

Figure 2.5 shows a typical cross-section of the Fermi surface of a noble metal. The dashed-line represents the first Brillouin zone (BZ). The arrows represent vectors which give rise to oscillation in DOS. The arrows link opposite parts of the contour plots with the same curvature (parallel line segments). In the plane (110), four different periods are predicted, and in this cross section only one is presented, which is the vertical arrow. The oblique arrow is the period predicted for the (111) plane. For the (100) plane two arrows give the long and short oscillation periods.

Therefore, in the plane (100) two QW oscillation periods are expected. Consequently, two stationary waves with vectors k_1 and k_2 are defined by the Fermi surface of the noble metal.

Considering the oscillations modulated by an envelope function k_{env} the atomic spacing of the material should be taken into account. The k_{env} is defined as $k_{\text{BZ}} - k_{\perp}$, where k_{BZ} is the zone boundary wave vector at high symmetry. For a (100) interface $k_{\text{BZ}} = 2\pi/a$, where a is the lattice constant of the spacer, Eq 2.13 can be rewritten as:

$$2k_{\text{env}}D - \phi_1 - \phi_2 = 2\pi\nu, \qquad (2.14)$$

where ν is a new quantum number, $\nu = N - n$, and N is an integer multiple of the atomic spacing a. From Eq. 2.14 the oscillation period Λ can be extracted
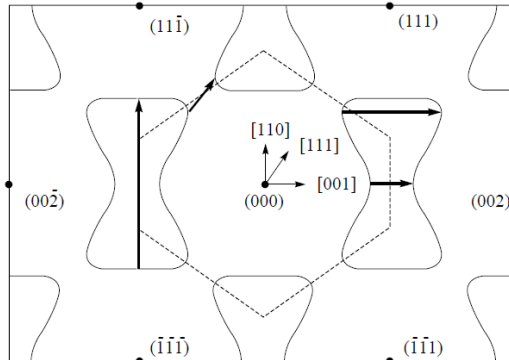
Figure 2.5: Fermi surface contour plot of the (110)-cross section of a bulk noble metal. The bold points belong to the fcc reciprocal lattice. The first BZ boundary is indicated by the dashed line. The solid thick arrows represent the vectors $k_\perp$ giving the oscillation period in the respective plane orientation [92].

as $\Lambda = \pi/(k_{\mathrm{BZ}} - k_\perp)$. In the case of QWS crossing the Fermi level, $k_\perp$ equals the Fermi wave vector k_{F} [102],

$$\Lambda = \pi/(k_{\mathrm{BZ}} - k_{\mathrm{F}}). \tag{2.15}$$

These vectors, k_1 and k_2, connect two parallel areas of the Fermi surface (called calipers) of the interlayer. In a $k_\parallel = 0$, k_1 gives the long oscillation period. The short period is obtained for a larger k_2, and arbitrary $k_\parallel$. k_2 can be located in Fig. 2.5 at the end of the "dog bone" shaped Fermi surface.

The reflections at the interfaces result in a modulation of the electron density of states. The variation of the density of states due to the quantum confinement depends on the thickness of the spacer. The spacer may enhance or suppress the density of states near E_{F}. In a trilayer FM/NM/FM system, the magnetization of the ferromagnetic layers depends on how far the QWS is from E_{F}. When the thickness of a nonmagnetic layer results in QWS far away from E_{F}, the antiparallel orientation of the magnetization is favored. On the other hand, for a quantum well state near the Fermi level, the minority electrons are confined in the spacer layer and the parallel magnetization orientation is favored. Thus, the periodicity of the oscillations in the interlayer exchange coupling with increasing spacer thickness is determined by QWS in the spacer layer. The quantum interferences in thin films due to confinement effects are investigated by photoemission [103]. This technique gives the opportunity to select the wave vector, energy, and spin character. The oscillation periods of the IEC are experimentally accessible by scanning electron microscopy with polarization analysis (SEMPA) and

18

magneto-optical Kerr effect (MOKE) measurements [104–106].

Biquadratic term - non-collinear magnetization

The exchange coupling energy per unit area of two layers is described by Eq. 2.10 and 2.11 as [96]

$$E_{AB} = -J_1 \cos\theta - J_2 \cos^2\theta. \tag{2.16}$$

The second-order term considers a non-collinear alignment of the layer magnetization. This relation was included in view of the observed perpendicular magnetization alignment, i.e. 90° in-plane [106–109]. From Eq 2.16, when the second-order term dominates, the angle between the magnetization $\mathbf{M}_A$ and $\mathbf{M}_B$ is 90°, provided $J_2 < 0$. However, in the case of $J_2 \geq 0$, a minimal influence on the coupling is observed, and the magnetization results in a collinear coupling (P or AP).

In general, whenever J_1 is the dominant term, but a negative J_2 is present, a canted magnetization orientation may be expected. In the case of $J_2 < 0$ and $2|J_2| > |J_1|$, the angle of the minimum energy is $\cos\theta = -J_1/2J_2$. Therefore, the presence of J_2 renders a canted magnetization, which has been experimentally detected [98, 110]. The canted phase denotes the configuration where the magnetization of the layers has an arbitrary angle between each other. Only in the extreme case of $J_2 >> J_1$, the magnetizations have a 90° alignment between them. The presence of J_2 has been reported and predicted in several systems, Fe/Cu/Fe, Fe/Cr/Fe, Fe/Au/Fe, Fe/Al/Fe, Fe/Ag/Fe [110–114].

The origin of a biquadratic term J_2 in a given system can be intrinsic or due to the presence of structural disorder [98]. Some phenomenological models have been proposed to describe the origin of the biquadratic coupling.

The intrinsic origin of J_2 results from non-collinear moments in each magnetic layer, as induced by other interactions. It was, first, calculated for an ideal surface and interface system. The prediction determined that J_2 would oscillate commensurately with J_1. However, this has not been observed experimentally. For the case of extrinsic sources, several effects have been related to the experimental observations. Examples of models to describe experimental canted phases are: "loose spin", thickness fluctuations, "pinhole", and magnetostatic coupling. Each one is described below.

"Loose spin" is a model that describes magnetic moments that are weakly coupled. In this model, it is assumed that a small concentration of magnetic impurities is embedded in the spacer. It represents an additive contribution to the energy coupling of the two magnetic layers. This model describe the

strong dependence of J_2 on temperature. This behavior has been observed in Fe/Ag/Fe [107], in Co/Cu/Co [108], and in Fe/Cu/Fe [115].

Thickness-fluctuations are discussed to explain a slightly rotation of the magnetization. Basically, it is considered for a incomplete last monolayer, where the thickness fluctuates by 1 ML. The terrace's height, therefore, is one atomic layer with a width L. Thus J_2 depends on the terrace width and J_1 as $\pm \Delta J_1$, due to the additional static wave of magnetization in and out of the terrace thickness fluctuation. This thickness-fluctuation has been reported for Fe/Cr/Fe [110, 113].

"Pin-hole" describes a direct exchange coupling. This interaction favors a ferromagnetic configuration, and it is attributed to direct coupling of both FM layers through openings ("pin-holes") in the spacer. It is in general restricted to very thin spacer layers.

Magnetostatic coupling results from a periodic roughness at the interface. The roughness gives rise to magnetic poles that contribute to the magnetization. Thus, the model takes into account the dipole fields created by a periodic rough interfaces. J_2 in this case depends on the period and height of the steps. This dependence of J_2 with interface roughness was observed in Fe/Au/Fe system [109].

In this thesis, the magnetoelastic coupling behavior of a trilayer of Fe/Au/Fe grown on Au(001) is investigated in terms of IEC and QWS. In the next Chapter 3, I describe the experimental techniques and methods involved in this work.

Chapter 3

Experimental setup and methods

This Chapter presents the main experimental setups and methods used in this work. Section 3.1 focuses on the optical bending beam technique used for the measurements of stress of ultrathin films. The films were grown *in-situ* under ultra-high vacuum (UHV) conditions. An overview of the UHV chamber is presented in Section 3.2. Details of the surface science techniques used for sample preparation such as low energy electron diffraction (LEED) and Auger electron spectroscopy (AES) are also included. The magnetic characterization was performed by magneto-optical Kerr effect (MOKE), which is briefly described in the Section 3.3. Finally, Section 3.4 presents details of the sample preparation.

3.1   Optical beam deflection technique

The optical beam deflection technique is based on the bending of a cantilever substrate due to an induced stress at one of its surfaces. The stress causes the cantilever substrate to curve. By measuring the curvature in real time, the involved stress is directly accessed during film growth and magnetization processes. I exploited this technique to quantify epitaxial misfit stress during film growth and to measure magnetoelastic coupling during a magnetization process. Apart from these, this technique can be also used to measure, for example, surface stress changes [49], stress change during surface reconstruction [50], and it can contribute to measure the substrate elasticity [116]. I used this technique to obtain, the previously unknown Young's modulus of $Bi_2Se_3(0001)$.
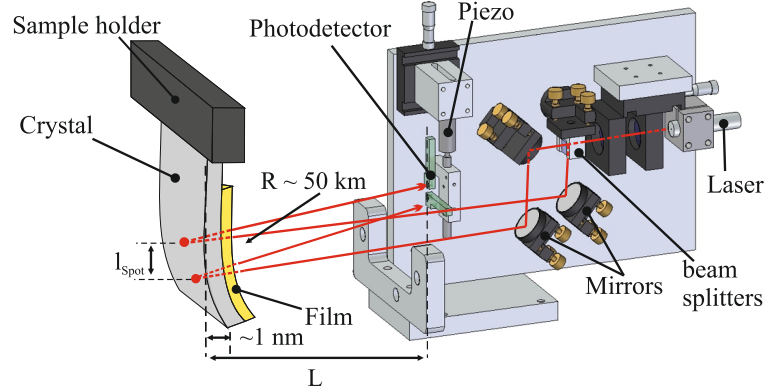
Figure 3.1: A schematic of the optical beam deflection setup. The sample is fixed at the upper end in the sample holder and free in the lower end. A representative value of the deflection of the crystal and its equivalent radius of curvature in km is given. The setup, except for the sample holder, is fixed at a CF100 or CF63 window of the UHV chamber. Adopted from [30].

3.1.1 Stress measurement

The dimensions of the substrate play an important role for the stress sensitivity of the measurement. Thin (≈ 0.1 mm) rectangular substrates are used, with $length = 4 * width$ to minimize the effect of clamping on substrate curvature [30]. The substrate is fixed along its width at one end and its other end is free to bend as a cantilever. Figure 3.1 shows a scheme of the optical beam setup which I used to obtain the stress during film growth and the magnetoelastic stress during magnetization reorientation processes.

Figure 3.1 shows the working principle: a laser beam is split into two, and both beam are directed by mirrors to the sample surface. The two beams hit the sample at two different positions some millimeters apart along the vertical direction near the lower end of the crystal. The beams are reflected onto two independent position sensitive photodetectors(split-photodiodes [30]). The photodiodes are connected to amplifiers, which deliver two signals: the sum and the difference of the two photo currents of each detector. The sum indicates the overall illumination and the difference is used to obtain the relative beam position of each beam at each detector. The induced curvature of the crystal gives rise to a displacement of the reflected beams on the split-photodiodes, and this beams displacement differs for both beams. The result is a change of the difference signal, while the sum signal largely remains unaffected. Due to the geometry of the setup the curvature is linked to the

22

change in the position signal as:

$$\frac{1}{R} = \frac{\Delta m}{2l_{\text{Spot}}L},\tag{3.1}$$

where L is the distance between sample and detectors ($L = 280$ mm), l_{Spot} is the beams separation on the surface ($l_{\text{Spot}} \cong 4$ mm) and Δm is a difference of position signal change of the photodetectors. Δm is calculated from the difference in signal as ($\Delta m = (\Delta_{\text{top}} - \Delta_{\text{bottom}})\cdot$ Calib). The calibration factor Calib is obtained from a measurement of the position signal variation for a known displacement of the detectors by a calibrated piezo drive [30].

Due to the crystal geometry (length to width ratio> 4) the bending can be treated as free two-dimensional bending [50]. Considering a biaxial film under isotropic biaxial stress, the modified Stoney equation [51] describes the relation between change of curvature $\Delta(\frac{1}{R})$ and stress change $\Delta\tau_{\text{F}}$:

$$\Delta\tau_{\text{F}} = \frac{Y_{\text{S}}t_{\text{S}}^2}{6(1-\nu_{\text{S}})t_{\text{F}}}\Delta\frac{1}{R},\tag{3.2}$$

where Y, t and ν are the Young's modulus, thickness and Poisson ratio of the substrate, respectively. The subscript S describes substrate properties, and F film properties. The film thickness is t_{F}.

I performed mainly two types of stress measurements: film stress during growth and magnetoelastic stress during magnetization reorientation. One source of film stress is the lattice mismatch between film and substrate during epitaxial growth (see Section 2.1). Other contributions are expected, e.g. surface stress, lifting of surface reconstruction, change of adsorbate coverage, formation of dislocations [50–52]. The induced stress during film growth is typically of the order of GPa for misfit in the percent range. On the other hand, the stress induced during magnetization process is two order of magnitude smaller, which is equivalent to a curvature of several $(\text{km})^{-1}$. The sensitivity for a direct measurement without averaging correspond to a minimum deflection of the bottom end of the substrate of ≈ 1 nm, and a maximum $R \approx 50$ km.

Magnetoelastic stress is measured by the same setup where external magnetic fields are added. However, the change of curvature of the crystal is now induced by a change of magnetization direction, due to magnetoelastic coupling. The relation of the curvature $(\frac{1}{R})$ and the magnetoelastic stress (τ_{me}) is given by:

$$\Delta\tau = \Delta(\tau_{\text{me}} \cdot t_{\text{F}}) = \frac{Y_{\text{S}}t_{\text{S}}^2}{6(1+\nu_{\text{S}})}\Delta\frac{1}{R}.\tag{3.3}$$

The change in the magnetization orientation from horizontal (along sample width) to vertical (along sample length) in-plane directions is induced by

external magnetic fields produced by electromagnets. The difference of the stress between two magnetization directions gives directly the magnetoelastic coupling coefficient B_i. The magnetoelastic coefficient B_i in terms of the radii curvature is [51]:

$$B_i = \frac{Y_S t_S^2}{6(1 + \nu_S) t_F} \left(\frac{1}{R} \bigg|^{M\|length} - \frac{1}{R} \bigg|^{M\|width} \right).$$ (3.4)

Note that from Eq. 3.4, B_i depends on the relative orientation of the crystal and the magnetization. Here, $M \parallel length$ indicates that the magnetization is kept parallel to the crystal length, and $M \parallel width$ indicates a magnetization parallel to the crystal width. In a cubic system B_1 and B_2 are obtained with

$$B_1 = \tau_{me}^{\|[100]} - \tau_{me}^{\|[010]}$$ (3.5)

and

$$B_2 = \tau_{me}^{\|[110]} - \tau_{me}^{\|[1\bar{1}0]}.$$ (3.6)

In Chapters 5 and 6, I use Eq. 3.5 and Eq. 3.6 to obtain B_1 of an Fe film on Au(001), and B_2 of Fe on Ag(001), respectively. It is important to note that the mechanism behind the epitaxial growth of bcc Fe on fcc Au or Ag includes a 45° rotation in relation to the Au or Ag fcc lattices. Therefore, to obtain B_1 and B_2 it is required that the substrates (Au and Ag) are cut along the length parallel to [110] and [010] directions, respectively. The orientation of the crystal was confirmed by LEED patterns, as discussed in Section 3.4. Next, the importance of the Young's modulus for a quantitative analysis of the optical curvature stress measurement is reviewed.

3.1.2   Determination of Young's modulus (Y) of a Bi_2Se_3 crystal

The cantilever method gives direct access to the curvature of the substrate with high precision. With this technique one can also measure elastic constants. As I could not find any experimental determination of Y of Bi_2Se_3 in the literature, I performed such experiments. I determined Y of Bi_2Se_3 by two methods: a) from the flexural vibration frequencies, and b) from the weight-induced deflection of the Bi_2Se_3 cantilever crystal. Schematics are shown in Figs. 3.2a and b.

The schematic of the resonance frequency of flexural vibrations method is shown in Fig. 3.2a. The flexural vibration of the crystal is excited by a loudspeaker placed on top of the manipulator. The driving ac signal is 1 in Fig. 3.2a. The vibration of the sample is monitored by measuring the ac
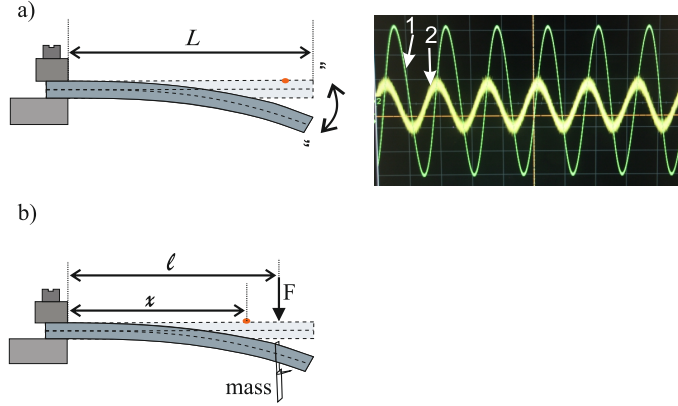
Figure 3.2: A schematic of the methods to obtain the Young's modulus (Y) of the cantilever crystal a) from the flexural vibration frequencies in resonance; 1: driving frequency, 2: crystal vibration b) from weight-induced deflection, where a known mass is placed at a length l of the free length of the crystal.

component of the position signal, which is represented by curve 2 in Fig. 3.2a. Note that the driving oscillator has a phase shift of $\pi/2$ in relation to the driven force. A driven damped oscillator acquires the same frequency as the driven force but it has a different amplitude and phase. The amplitude has a peak on the resonance frequency and the corresponding phase shift at the resonant frequency is $\pi/2$, which is in agreement to phase shift observed in Fig. 3.2a. The resonance frequency of flexural vibrations of a cantilever is given by [117]:

$$f_n = \frac{\beta_{\mathrm{n}}^2}{2\pi}\sqrt{\frac{YI}{mL^4}}, \tag{3.7}$$

where m is the mass, L is the length of the sample, Y is Young's modulus, β_{n} is a mode constant ($\beta_1 = 1.8751$, $\beta_2 = 4.694$, and $\beta_3 = 7.855$) [30], and I is the areal moment of inertia. I is calculated as [118]

$$I = \frac{bt^3}{12}, \tag{3.8}$$

where b and t are the width and thickness of the sample. Thus, the Young's modulus is derived from a measurement of the resonance frequency of the cantilever sample by the optical deflection measurement.

   The second technique exploits the deflection of the cantilever upon application of a known force at a given position of the cantilever. The change of slope $w^{'}$ of the cantilever deflection is measured upon loading the cantilever
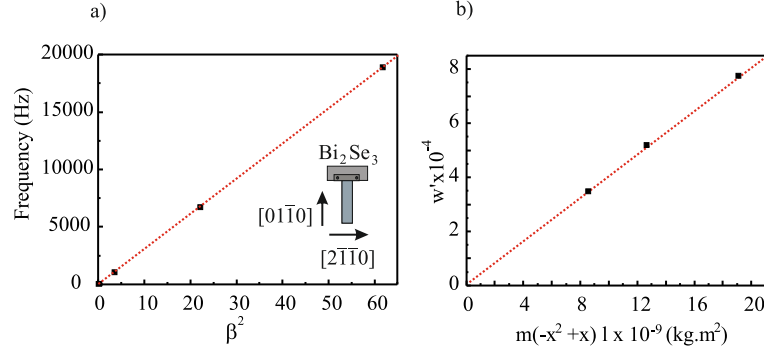
Figure 3.3: Experimental determination of the Young's modulus of a $Bi_2Se_3(0001)$ crystal. a) Plot of the resonance frequencies as a function of the mode constant (β^2). The slope of the dashed linear fit is 306.35 ± 0.02 Hz. The insert shows the crystal orientation. b) Plot of the change of slope of the crystal $(w^{'})$ upon loading with a mass. The linear fit (dashed line) is $4.1 \times 10^4 \pm 7.1 \times 10^2$ kg m^2.

with a known mass. The relation of slope $w^{'}$ with Y is given by [119]:

$$w^{'}(x) = \frac{Fl^2}{2YI}\left(-\frac{x^2}{l^2} + \frac{2x}{l}\right),\qquad(3.9)$$

where F is the force due to the attached weight, I is the areal moment of inertia, l and x are the lever arm length of the mass(force) and the position of the slope measurement, respectively. See sketch in Fig. 3.2b.

Figure 3.3a gives the plot of three resonance frequencies measured on a Bi_2Se_3 crystal as a function of mode constant β^2. Figure 3.3b gives the change of slope due to loading the cantilever with three different masses.

The measurements of the Young's modulus for $Bi_2Se_3(0001)$ give an average $Y = 47\pm9$ GPa, where the results from both measurements are $Y_{vibr.} = 49 \pm 0.1$ GPa and $Y_{load} = 43\pm5$ GPa.

Young's modulus is defined as $Y = \tau/\epsilon$, which represents the stiffness of the material. This relatively small value of Y is not unexpected for its peculiar crystalline structure. Bi_2Te_3 has a similar layered structure, and the experimental Young's modulus is 54.2 GPa, in close agreement with a theoretical result ($Y = 51.4$ GPa) [120]. These layered materials are very soft in comparison with metals such as Ir, where $Y = 634$ GPa [26].

Note that the Poisson's ratio ν cannot be determined this way. Poisson's ratio is defined by the ratio of lateral strain to axial strain when the material is subjected to an uni-axial stress [121]. I could not measure Poisson's ratio of $Bi_2Se_3(0001)$ in this work. From the similarity of the Young's modulus of

Table 3.1: Elastic constants: Young's modulus (Y) and Poisson's ratio (ν); and the crystal substrates thickness (t_S) used in this work.

Crystal	Y [GPa]	ν	$Y/(1-\nu)$ [GPa]	t_S [μm]
Ag(001)[a]	43.67	0.423	75.68	91
Au(001)[b]	78	0.44	139.28	90
Fe(001)[a]	131	0.37	207.93	
Bi_2Se_3(0001)[c,d]	47	0.241	61.92	$100-340$

[a] Ref. [123], [b] Ref. [124], [c] this work, and [d] Ref. [122].

Bi_2Se_3(0001) and Bi_2Te_3(0001), I tentatively take the value ν as $\nu = 0.241$, as given for Bi_2Te_3(0001) [122].

The bulk values of all elastic constants used in this work are given in Table 3.1. All t_S were measured/checked by the flexural vibration method.

3.2   Ultra-high vacuum (UHV) system

In order to achieve best well-defined sample preparations and assure the absence of significant contaminations on the surface, the experiments were performed under ultra-high vacuum (UHV) condition, with a base pressure of order 10^{-11} mbar. The gas pressure and gas composition inside the chamber is monitored by ion gauge and a quadrupole mass spectrometer, respectively. The chamber is divided in two parts by a gate valve, see Fig. 3.4.

The upper part is used for the sample preparation and structural analysis. There are evaporators for metals, an ion gun, low energy electron diffraction (LEED), Auger electron spectroscopy (AES), and the optical beam deflection setup. In the lower part of the chamber (Fig. 3.4), the magnetic measurements are performed with the optical beam deflection and magneto-optical Kerr effect (MOKE) setups. There is one electromagnet to apply a vertical magnetic field, and an external electromagnet, which can be rotated by 90°, is used for horizontal fields and for magnetization perpendicular to the surface. This electromagnet can achieve fields of the order of 0.3 T at 20 V, 20 A. The small magnet produces fields along the vertical direction of up to 0.1 T.

The manipulator drives the sample up and down, with rotation of 360° and ± 2 centimeters of freedom in the x- and y-directions. Besides the sample, several further utilities are fixed on the manipulator: a K-type thermocouple (NiCr-NiAl) to monitor the sample temperature, a quartz microbalance to calibrate the deposition rate, and a fluorescent screen to calibrate the alignment of the ion beam. Additionally, located behind the sample, is an e-beam

2.50 m

LN2

manipulator

LEED
MEED

AES

sample

Ti-sublimation
pump

ion pump

gate valve

magnet
for vertical
field

magnet for
longitudinal
and polar field
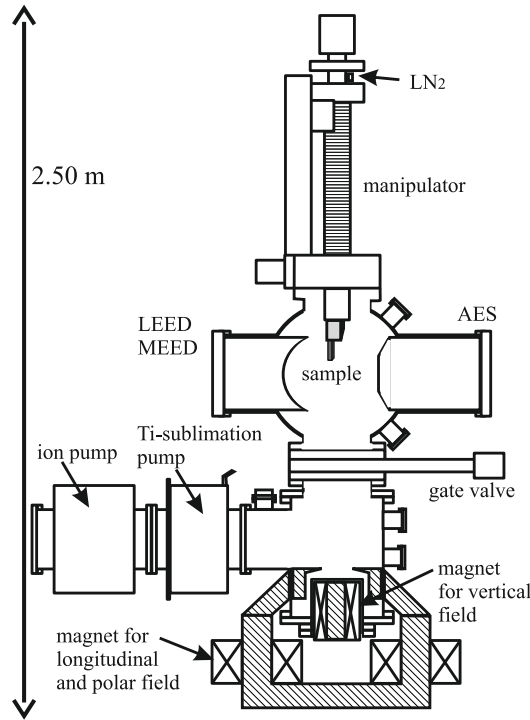
Figure 3.4: Schematic of the UHV chamber.

filament-heater to heat the sample to high temperature. The heating is done
by a W-shield placed between filament and sample to protect the crystal
and to distribute the heat homogeneously. Near the sample a Cu-braid es-
tablishes thermal contact to a capillary that can be filled with liquid-N_2 to
cool the sample (indicated in Fig. 3.4). In summary, the temperature of the
sample can be adjusted in the range from 150 to 1500 K.

Next, I focus on the surface science techniques available to examine the
quality of the sample preparation.

Low Energy Electron Diffraction (LEED)

Low energy electron diffraction (LEED), is a technique used to study
the structure of surfaces. It was first proposed in 1927 by Davisson and
Germer [125] and it is widely used in the present days. As it is named,
this method uses low energy electrons ($20 - 500$ eV) to study the surface
structure from an analysis of a diffraction pattern. The wavelength (λ) of
these electrons are comparable to atomic distances of a solid crystal and the
mean free path in a solid is typically of $5-10$ Å, which results in a pronounced

Figure 3.5: Sketch of a LEED measurement and a simplistic 1D chain of atoms simulating the scattering of electrons from the incidence beam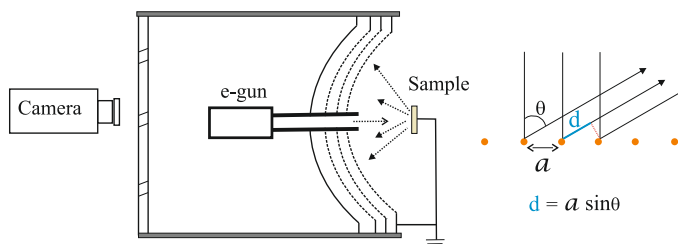, the "path difference" (d) in the distance the radiation has to travel from the scattering center to a distant detector is defined.

surface sensitivity.

Figure 3.5 shows a sketch of the LEED setup and a simplistic 1D surface diffraction. The electrons collide with the sample surface giving rise to diffraction, which depends on the surface crystallography. The back scattered electrons pass through grids and reach a fluorescent screen. The grids act as an energy filter allowing only elastically scattered electrons to pass through, thus lower energy secondary electrons do not contribute to the image. The result of this elastic reflection is a pattern of intensities, which reflects the surface symmetry on the fluorescent screen. The selection rule to diffraction in a 2D surface is written as:

$$a \sin \theta = \sqrt{h^2 + k^2} n \lambda, \tag{3.10}$$

where h, k are the Miller indices, a is the lattice constant of the crystal, n and θ are the order of diffraction (integer) and emission angle, respectively. λ is the electron de Broglie wavelength. It is written as function of energy as:

$$\lambda = \frac{h}{p} = \frac{h}{\sqrt{2mE}}. \tag{3.11}$$

From the position of the diffraction pattern and Eq. 3.10, θ can be extracted and the in-plane atomic distance in Ångtrom is given by:

$$a = \frac{nL12.26}{l} \sqrt{\frac{h^2 + k^2}{E(eV)}} \tag{3.12}$$

where L and l are distances between: sample and screen (72 mm) and between one of the primary spots to the (0,0) spot, respectively.

a)

      i) Ionization   ii) Excitation   iii) Auger electron
                                                  emission

b)
                    CMA

Sample   e-gun   Channeltron
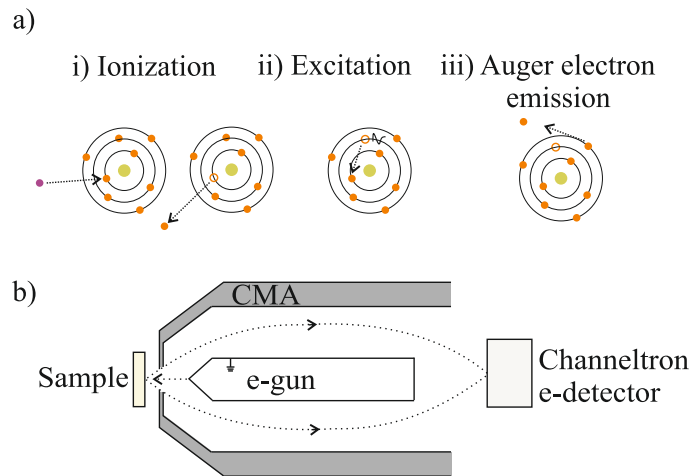   e-detector

Figure 3.6: a) The simplistic sketch of the steps of the Auger process in an atom. b) A schematic of the CMA electron energy analyzer used in the Auger setup with the electron gun and the cylindrical mirror analyzer (CMA).

Auger Electron Spectroscopy (AES)

Auger electron spectroscopy (AES) is an analytical surface technique. Its principle is based on the emission of an Auger electron upon electron incidence. The Auger electron has been first observed by Pierre Auger, which later inspired the development of this technique. Today, AES is commonly used to determine the chemical composition of a surface.

The Auger process consists of three steps: i) ionization; ii) excitation; iii) Auger electron emission, a sketch of the process is shown in Fig. 3.6a.

i) Upon collision of an incident electron, a core electron is removed from the atom. ii) An electron of an higher level fills the hole. iii) The energy left from the excitation is used to emit the Auger electron from the atom as well. From the analysis of its energy, the Auger electron energy identifies a specific element. Another technique associated with Auger transitions is the Auger-photoelectron coincidence spectroscopy (APECS) [126, 127]. This spectroscopy detects Auger and photoelectrons that are correlated in time and hence originate from the same ionization event. APECS is a powerful technique to probe electronic structure with extremely high surface sensitivity [128] and separate overlapping spectral features [127, 129].

The configuration of the apparatus for AES is shown in Fig. 3.6b. A 3 keV incident electron beam is directed normal to the surface. The sample current is of order of μA. The three processes presented above happen inside the atom

and Auger electrons are ejected from the crystal. These Auger electrons are analyzed in energy in a cylindrical mirror analyzer. Their intensity is measured by an electron multiplier. The surface sensitivity of the technique is governed by inelastic mean free path of Auger electrons in solids. Metals have a short inelastic mean free path yielding a depth sensitivity of the order of 10 monolayers ($\approx$ 2 nm) [130]. AES gives a sensitivity for surface concentrations of order of 1 atom% [131].

In this thesis, LEED and AES are used as a complementary techniques to obtain more information on the structure and chemical composition of the epitaxial thin films. The AES ratio ($\frac{AES\ int.\ Fe}{AES\ int.\ Ag}$) for Fe film on Ag(001) and Au(001) reveals the presence of Au and Ag atoms on top of the Fe film. This indicates surface segregation, and it is discussed in Chapters 5 and 6. The LEED measurements represent the atomic arrangement of the surface. Drastic changes of the surface order is observed after deposition of Fe on the Bi_2Se_3 substrate, see Chapter 4.

3.3 Magneto-optical Kerr effect setup (MOKE)

The magneto-optical Kerr effect (MOKE) is used to characterize magnetic properties of ferromagnetic thin films and multilayers. The Kerr effect is based on a change in the polarization of light upon reflection from a magnetized material. The reflected light experiences a Kerr rotation, which is the in-phase component with the incident light, and the out-of-phase component accounts for the Kerr ellipticity. This change in the polarization state of the reflected light is among other dependencies proportional to the magnetization $\mathbf{M}$. The magneto-optical response of the sample is obtained while the magnetic field is swept. The magneto-optical Kerr effect can be described by macroscopic dielectric theory [132, 133] or by a microscopic quantum mechanical theory [134].

Microscopically, the effect results from the coupling of the electrical field of the light and the electron spin within the magnetic medium through spin-orbit (SO) interaction [134]. The SO of the magnetic material brakes the left- right-symmetry of circularity polarized light. This symmetry braking result in two different refractive indices, for left and right circularly polarized light. Therefore, incident linearly polarized light is reflected with elliptical polarization, with a rotation from the original linear axis. The macroscopic description arises from the antisymmetric, off-diagonal terms in the dielectric tensor [132].

The MOKE measurement is performed with an incident laser light of λ=670 nm with a fixed incident angle of 30° with respect to the sample
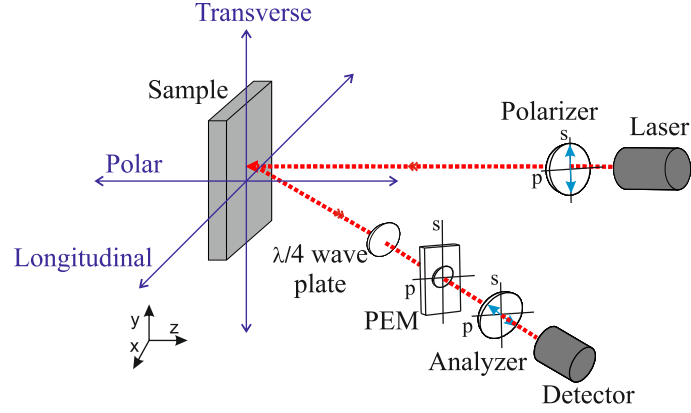
Figure 3.7: MOKE setup where three magnetization directions are indicated by the blue arrows. The s-polarized light is used in longitudinal and polar modes, and the transversal mode the s-polarized light is 45° rotated, as described in the text.

normal. S-polarized light is used, as given by the optical axis of the polarizer, set perpendicularly to the light plane. The s-polarized light is reflected from the sample, passes through a quarter-wave plate, a photoelastic modulator (PEM), and finally the light reaches the analyzer and detector. Note that the quarter-wave plate is necessary to compensate the phase shifts due to the UHV−window birefringence and the ellipticity of the metallic reflection of the sample. The PEM modulates the reference signal Kerr rotation (at twice the fundamental frequency: $2f$) and Kerr ellipticity (at fundamental frequency) [132, 135].

Figure 3.7 shows a schematic representation of the MOKE setup used in this work. There are three conventional MOKE configurations: longitudinal (LMOKE), transversal (TMOKE), and polar (PMOKE). The geometries of the MOKE depends on the magnetization vector **M** orientation with respect to the incident plane. In LMOKE (PMOKE) an external magnetic filed **M** is applied parallel (perpendicular) to the sample plane. In both geometries, s-polarized light is used. However, the PMOKE mode is sensitive to an out-of-plane magnetization. In contrast, LMOKE and TMOKE are sensitive to the in-plane magnetization. In TMOKE, however, **M** lies orthogonal to the plane of incidence but along the sample surface. In this case, the incoming light is set to a 45° rotation from the s-polarized direction.

The transverse MOKE configuration requires a change in the geometry of the setup, because of the vector product of the magnetization and the electric field of the incident light gives zero. The plane of polarization is rotated by 45° from the s-polarization, and to adjust the setup PEM and the analyzer
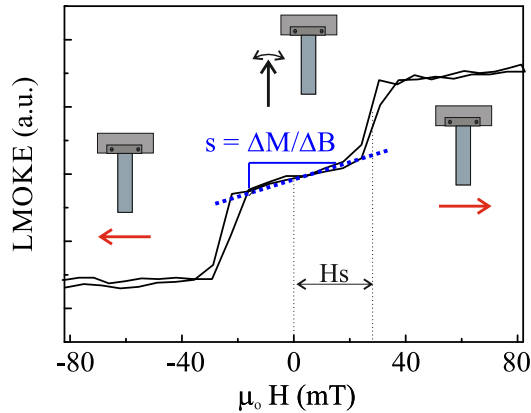
Figure 3.8: Longitudinal MOKE with additional constant bias magnetic field along the transversal direction the of thin film of Fe on Au(001). The hysiteresis loop is split into two due to the induced undirectional anisotropy. The sketches show the in-plane magnetization direction of the sample. The initial slope s and the shift field H_s are identified. The slope is inversely proportional to the biaxial anisotropy, as the H_s is used to find the uniaxial anisotropy constant.

are also rotate by 45°. The quarter-wave plate is no longer necessary. With this modifications of the geometry, the intensity of reflected light contains the information $\mathbf{M}$ [136].

The magnetic anisotropy of thin films can also be extracted by a quantitative analysis of the hysteresis loop obtained by MOKE. A method to obtain the anisotropies in films is to measure the magnetization rotation from the easy axis with field sweeping along the hard axis [137–139]. This technique uses two subsequent measurements of the saturation magnetization.

Weber and co-authors [140], propose a different approach for this technique. By applying a constant magnetic field ($\mathbf{H}_{bias}$) perpendicular to the sweeping field an additional unidirectional anisotropy is induced. With this method the anisotropies can be extracted from one single measurement. Figure 3.8 shows a split hysteresis loop of a thin film under a constant field applied in-plane perpendicular to the sweep field in a longitudinal MOKE geometry.

As the sweeping field decreases the constant field $\mathbf{H}_{bias}$ forces the magnetization to tilt. In a vanishing sweeping field, the magnetization of the sample is kept aligned to $\mathbf{H}_{bias}$. As the sweeping field increases again, the magnetization tilts from the original direction (aligned with $\mathbf{H}_{bias}$) up to a saturation in the sweep field direction. The tilt angle is determined by the magnetization component along the easy axis, the initial slope s of the

hysteresis loop. To align the magnetization along the sweeping field, an an-
isotropy barrier is overcome. At some field the magnetization flips and then
saturates. Both anisotropies, uniaxial (K_{u}) and biaxial (K_1), can be determ-
ined from the hysteresis loop, independent if the loop is taken along the easy
axis or from an intermediate axis [140]. The interplay of field contribution
to the magnetization splits the hysteresis loop of the magnetization reversal.
The reversible linear increase at small field is described by the linear initial
slope s. And the sharp transition to the saturation magnetization gives the
shift field H_{s}. H_{s} is determined by the field difference between the center of
one shifted loop and the zero field. The anisotropies are extracted from the
minimization of the total energy.

The total energy is given by the in-plane anisotropy energy and Zeeman
energy as

$$E(\phi) = K_{\mathrm{u}} sin^2(\phi) + (K_1/4) sin^2(2\phi) - \mu_0(\mathbf{H} + \mathbf{H}_{\mathrm{bias}}) \cdot \mathbf{M}, \qquad (3.13)$$

where ϕ is the angle between magnetization and easy axis, $\mathbf{M}$ is the saturation
magnetization, $\mathbf{H}$ and $\mathbf{H}_{\mathrm{bias}}$ are the sweep and bias field, respectively. From
the minimization of the energy with respect to ϕ, $\frac{\partial E(\phi)}{\partial \phi} = 0$, the anisotropies
are given directly by s and H_s [141, 142]. Considering $K_{\mathrm{u}} \ll K_1$ [140], the
anisotropies are obtained with respect to the bulk saturation magnetization
as

$$K_u = \mu_0(H_{\mathrm{s}} - H_{\mathrm{bias}})M_s \quad \text{and} \quad K_1 = \mu_0 M_{\mathrm{s}}^2/2s. \qquad (3.14)$$

This method was used in thin films on a vicinal substrate to determine
the contruibution of uniaxial and cubic anisotropies [141, 142]. However, it
can be applied for a film grown on a flat substrate, as seen for Co/W(001) in
Ref. [143]. They extract the fourfold cubic anisotropy by apply an additional
constant perpendicular magnetic field during MOKE measurement. Similar
to [140], the hysteresis loop in [143] split and a linear initial slope s could
be identified. From the analysis of the initial slope the cubic anisotropy was
found.

In the present work, I exploit this technique to obtain the cubic anisotropy
for the trilayer Fe/Au/Fe system. In order to obtain a split hysteresis loop
with an extended linear slope between the shifted loops, a constant field
along the [100] direction was applied. The sweeping field is applied along
[110] direction, $\mathbf{M}$ is followed by LMOKE. Figure 3.9 shows the hysteresis
loops of a trilayer of Fe(15 ML)/ Au(9 ML)/ Fe(10 ML), with an additional
vertical field of 10, 25, and 35 mT. The experiments are performed with
the bias field of 35 mT (28 kA/m), in order to obtain reliable slope values
for the entire thickness range investigated. A check of the reliability of this
technique with this strong bias filled has been made by extracting K of a
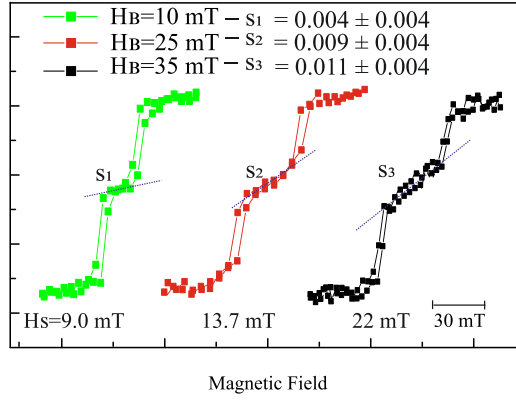
Figure 3.9: Longitudinal MOKE with additional constant bias magnetic field along the transversal direction, measured for the trilayer Fe(15 ML)/ Au(9 ML)/ Fe(10 ML) on Au(001). The hysteresis loop is split into two due to the induced unidirectional anisotropy. The slope s and the shift field H_s of each curve are given.

single Fe film of 25 ML on Au(001). Using the same $\mathbf{H}_{bias}$ of 35 mT, I obtain K_1 of 67 kJ/m^3. This value of K_1 is larger as compared with Fe bulk 48 kJ/m^3 [144]. The enhanced K_1 could be related with the strong bias field applied or due to an interface effects. However, a qualitative analysis can be obtain by this experiment, as seen in Chapter 7.

In this work all three MOKE modes were measured, but only longitudinal and transverse MOKE are presented. In the range of film thickness only the in-plane film magnetization is observed. A qualitative analysis of the MOKE signal under the presence of a constant vertical magnetic fields is also performed for the trilayer system. With these results I obtained the correlation between the oscillatory magnetoelastic coupling coefficient and the change of the crystalline anisotropy, see Section 7.2. The next section describes the sample preparation of each substrate used.

3.4   Sample preparation

In this thesis three different substrates are used, Bi_2Se_3(0001), Ag(001), and Au(001) single crystals. All of them have a rectangular shape with thickness ≈ 0.1 mm, length ≈ 13 mm, and width ≈ 2.5 mm. The Fe films are deposited from a 5 mm thick rod of 99,99% purity. I define 1 ML of Fe as a single layer of Fe bcc (100) bulk as $t_{Fe} = 1.43$ Å, which corresponding to an areal atomic density of 1 ML: 12.17×10^{14} cm^{-2}. The Au films are evaporated from a Mo-crucible, filled with Au wires of 99,99% purity. A single layer of
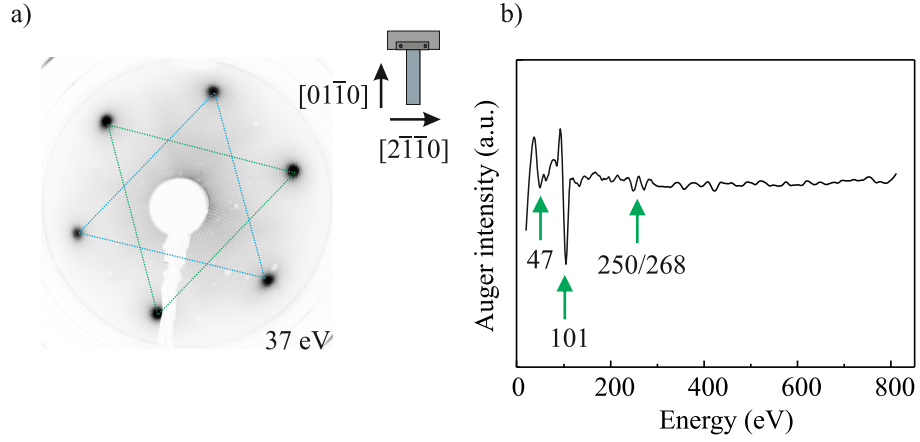
Figure 3.10: a) LEED diffraction of $Bi_2Se_3(0001)$ crystal at 37 eV. The LEED image is inverted for better visualization, dark means high and white means low intensity. The insert is the sketch of the directions on the crystal. b) Auger spectrum of the clean crystal at 3 keV primary energy. AES shows the peaks of Bi-NOO at 101 eV, 250, and 268 eV, and the Se-MNN peak at 47 eV (green arrows).

Au fcc (100) bulk equals 1 ML, with $t_{Au} = 2.04$ Å. This corresponds to an areal atomic density of 1 ML: 12.02×10^{14} cm^{-2}. The partial pressure during depositions is below 4×10^{-10} mbar, at a deposition rate of 1 Å/min.

$Bi_2Se_3(0001)$

In this work an alternative process of cleaning of $Bi_2Se_3(0001)$ crystals is used. The clean crystal surface can be obtained by cleavage, or alternatively, by sputtering, as described as the "alternative" method. The process of cleavage is not performed in this work due to the thickness range of the crystal and the design of the sample holder. The method has been reported, in detail, in our recent publication [63]. The crystal is subject to cycles of Ar-sputtering and annealing. The atomic structure of $Bi_2Se_3(0001)$ after the cleaning treatment is controlled by scanning tunneling microscopy [63]. The sputtering is performed by a differentially pumped sputter gun in an Ar partial pressure of 2×10^{-7} mbar. The Ar beam energy is 0.8 keV, with a 0.5 μA sample current. After sputtering the crystal for 15 minutes, an annealing period at 450 K for 30 minutes follows. I controlled both, surface crystallography and stoichiometry by LEED and AES, respectively.

Figure 3.10 presents a LEED image and an Auger spectrum after the cleaning process. The hexagonal pattern in the LEED with clear spots in-
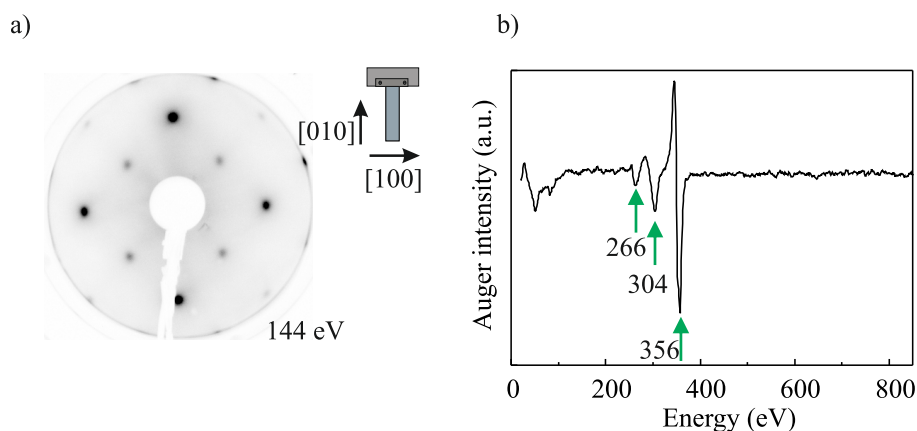
a)   b)

Figure 3.11: a) LEED patterns of Ag(001) crystal at 144 eV. The LEED image is inverted for better visualization, dark means high and white means low intensity. The insert is the sketch of the directions on the crystal. The plane is rotate 45°, thus the plane [010] is along the length of the crystal. b) Auger spectrum of Ag crystal at 3 keV shows Ag-MNN peaks at 266, 304, and 356 eV (green arrows).

dicates a sufficient temperature of annealing. However, due to its stacking along the c-axis the crystal reveals a threefold symmetry identified by the triangle for the different diffraction intensities on the LEED image. The Auger spectrum shows peaks at 101, 250, and 268 eV of Bi-NOO and a small contribution of Se-MNN at 47 eV, which confirms an atomically clean surface.

Ag(001)

For the Ag(001) crystal cleaning process, I followed a well established procedure [145]. The surface is sputtered by a differentially pumped sputter gun in an Ar partial pressure of 2×10^{-7} mbar, at an Ar energy of 1 keV and a sample current of 0.2 μA for 15 minutes. After the removal of the first layers of the surface the crystal is annealed. For this the substrate was held at 450 K for 30 minutes. I checked LEED images and Auger spectra of the clean crystal after each preparation. A typical LEED image and Auger spectrum of a clean Ag(001) crystal are presented in Fig. 3.11.

Figure 3.11 shows a LEED pattern with a clear (1×1) surface pattern. In this 2D image, the pattern indicates that the length of the crystal is cut in the [010] direction. Figure 3.11b shows the Auger spectrum of pure Ag, where no contamination is observed. The relevant Auger peaks of Ag-MNN are presented by the arrows at 266, 304, and 356 eV.

a)   b)
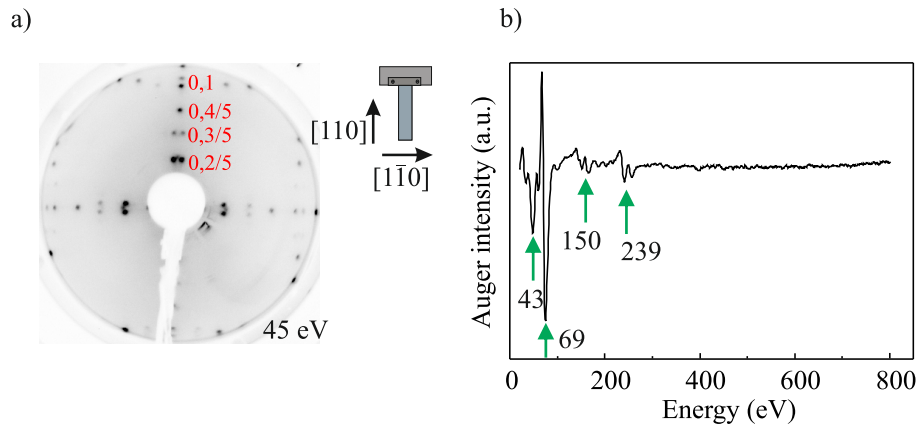
Figure 3.12: a) LEED patterns of Au(001) crystal at 45 eV, the numbers represent the characteristic (1×5) reconstruction of Au prepared with cycles of sputtering and annealing. The LEED image is inverted for better visualization, dark means high and white means low intensity. The insert is the sketch of the directions on the crystal. b) AES of Au(001) at 3 keV, which shows the main Au-NVV peaks at 43, 69, 150, and 239 eV (green arrows).

Au(001)

The process of cleaning the Au(001) crystal is similar to the procedure adopted for the Ag crystal. I reduced the Ar partial pressure to 4×10^{-8} mbar, at an energy of 0.8 keV and sample current of 0.5 μA. The annealing in Au is made at higher temperature than Ag, a temperature of 580 K is applied for 20 minutes.

Figure 3.12 shows a LEED image and an Auger spectrum of the cleaned Au crystal. The LEED pattern shows the typical reconstructed (1×5) surface of clean Au(001) [146]. The reconstruction of Au(001) has been intensely investigated [147–150]. The visible double or triple spots observed in 0.3/5 or 0.2/5 positions result from the existence of two mutually perpendicular domains [151]. The Au(001) reconstruction is also known as (5×20) and c(26×68), but in the present work we refer to (1×5). The LEED pattern confirms the length of the crystal along the [110] direction. The Auger spectrum shows four main peaks of Au-NVV indicated by the arrows at 43, 69, 150, and 239 eV.

Chapter 4

Stress and structure of Fe and FeSe on Bi_2Se_3(0001)

In this Chapter, I present results on stress measurements during deposition of Fe on Bi_2Se_3(0001). The impact of different growth temperatures on the resulting stress is investigated. The procedure for the substrate preparation and Fe evaporation are detailed in Section 3.4. Here, I investigated compositional and structural properties after Fe deposition via LEED and Auger measurements. The deposition temperature induces a change in the stress due to the change in morphology. A well ordered structure is identified for higher temperature. The results indicate that Fe bonds to Se atoms, which are provided by the substrate, forming FeSe. This leads to the formation of FeSe nanocrystals embedded on the Bi_2Se_3 substrate [63].

Figure 4.1a shows the stress during deposition of a submonolayer (0.3 ML) amount of Fe on Bi_2Se_3at different substrate temperatures. The Fe deposition was calibrated by a quartz oscillator as described in Section 3.4. The black solid line represents the stress during deposition at 150 K, red shows the stress at 298 K and the green curve shows the stress measured at 473 K.

I find that the total stress change $\Delta\tau$ increases with increasing growth temperature. At the lower temperature of 150 K a small compressive total stress change is observed. The compressive stress is of the order of -0.5 N/m. As the deposition temperature increases, the total compressive stress increases to -2.3 N/m and -3.5 N/m at 298 K and at 473 K, respectively. Figure 4.1b summarizes the total stress change for different deposition temperatures. An almost linear increase of total stress change $\Delta\tau$ with increasing temperature is observed.

In order to understand the behavior of the stress change with increasing deposition temperature, AES and LEED measurements were performed. The measurements were done at room temperature after Fe deposition at
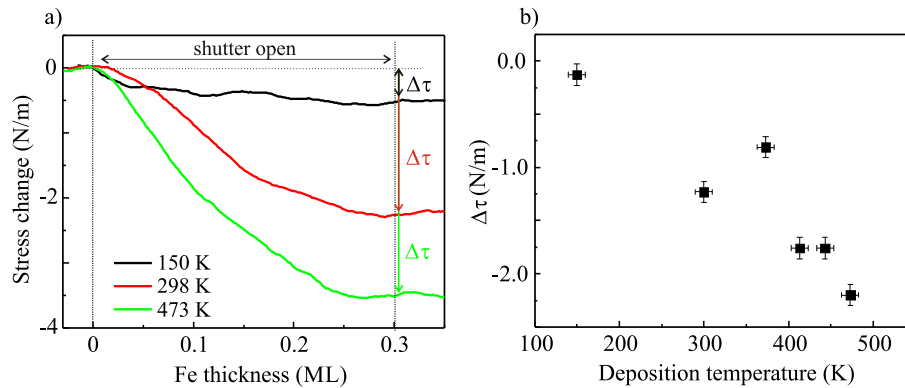
Figure 4.1: a) Stress measurements during deposition of 0.3 ML of Fe on Bi$_2$Se$_3$(0001) at different temperatures. The dashed vertical lines indicates opening and closing of the Fe evaporator. The total stress change between onset and termination of deposition $\Delta\tau$ is indicated. b) Total stress change $\Delta\tau$ after Fe deposition as a function of deposition temperature.

different temperatures. Figure 4.2a shows AES spectra of samples prepared at 150, 298 and 473 K. All spectra show the characteristics peaks of Se-MNN at 47 eV, Bi-NOO at 101 eV and the three peaks of Fe-LMM at 598, 650 and 703 eV. Relative changes of peak intensities of the Se (47 eV), Bi (101 eV), and Fe (650 eV) [152] are observed. The variation of the intensity is apparent for a quantitative analysis of the AES data by calculating the AES-intensity Fe-LMM/Bi-NOO ratio. The Fe-LMM/Bi-NOO ratio values are given in Fig. 4.2a. The Bi/Fe ratios decrease with increasing deposition temperature. This indicates that changes in the deposition temperature modify the distribution of the elements at the surface.

As outlined in the discussion Section 8.1, these results suggest a replacement of Bi by Fe at higher temperature to form FeSe. This assessment is further corroborated by LEED measurements. The structure at the surface also shows characteristic and specific variations with increasing deposition temperature.

The LEED images at 51 eV for each deposition temperature are presented in Fig. 4.2b, as indicated by arrows from the respective Auger spectrum. For the deposition at 150 K the LEED image does not show any distinct diffraction pattern. It is remarkable that the diffraction spots related with Bi$_2$Se$_3$ crystal are not present either, cf. Section 3.4. In contrast, the diffraction pattern appears for depositions at elevated temperatures. The LEED image reveals diffraction spots for samples prepared at 298 K. However the intensity is low, and the spots are blurred. LEED after higher deposition
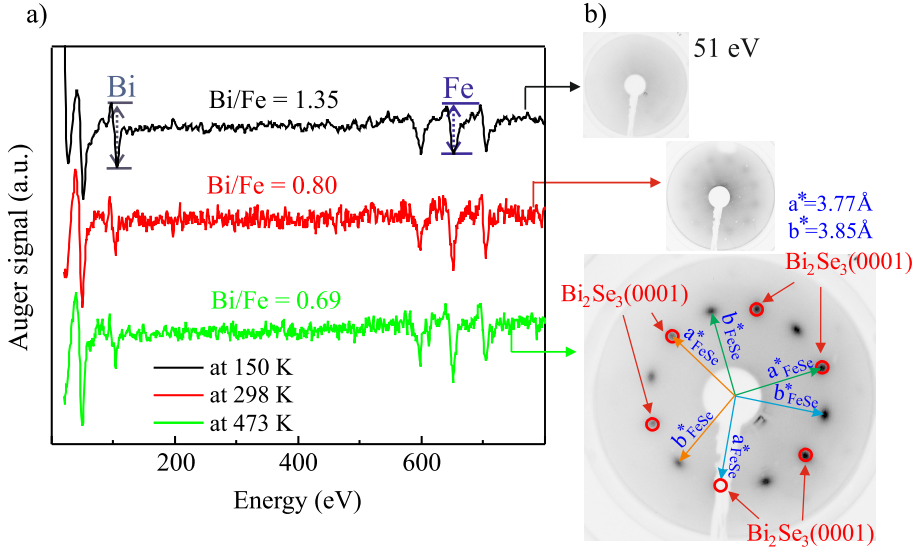
Figure 4.2: a) Auger spectra and the respective Bi/Fe ratio and b) LEED images at 51 eV after Fe deposition on Bi$_2$Se$_3$(0001) at different temperatures. Auger spectra are vertically shifted for sake of visualization. In (b) a distinct diffraction pattern is observed only for deposition at high temperature. An interpretation of the diffraction pattern is indicated in the image. Three rotational domains of the FeSe lattice are identified. The LEED image is inverted for better visualization, dark means high and white means low intensity.

temperature shows a clear and distinct diffraction pattern. This suggests that the variation of deposition temperature, indeed, modifies the sample surface and its geometric structure. LEED measurements suggest a lack of crystalline order at the surface for deposition at 150 K. This changes to a well ordered surface for samples prepared at higher temperatures of 473 K. The latter sample presents a modified diffraction pattern as compared with the clean Bi$_2$Se$_3$ crystal. This indicates a distinct structure at the surface. This LEED pattern and the correponding surface structure of the formed FeSe are discussed in Section 8.1.

In summary, to understand the deposition temperature dependence of the stress measurements three considerations should be taken into account, (i) the decrease of Bi concentration near the surface as shown in AES; (ii) the suppression of crystalline order at the surface after deposition of Fe atoms at low and room temperature, as revealed by LEED measurements; (iii) the tendency towards the formation of FeSe nanocrystal as derived from LEED and STM in Ref. [63]. The formation of FeSe nanocrystals in a well ordered fashion with three rotational domains embedded in the Bi$_2$Se$_3$ surface

will be considered in the discussion of anisotropic strain distribution in the Discussion chapter of this thesis: Section 8.1.

These results are the first stress measurements for the deposition of Fe on $Bi_2Se_3(0001)$. The discussion in Section 8.1 reveals that the increasing total stress change with increasing deposition temperature identifies the formation of an ordered FeSe compound, where Se is supplied by the substrate.

Next, I will focus on the growth of Fe on the metallic substrates, Ag(001) and Au(001). Here, stress measurements provide new insights by revealing that stress can deviate from the calculated misfit stress due to additional stress contributions from segregation and interdiffusion.

Chapter 5

Film stress and magnetoelastic stress of Fe on Ag (001)

In this Chapter, I present results on film stress and magnetoelastic stress of epitaxial Fe films on Ag(001). Section 5.1 focuses on the film stress during growth of Fe monolayers. Details of the sample preparation are given in Section 3.4. The stress results are presented as a function of Fe thickness and growth temperature. I investigate the structural properties of Fe films in view of Fe interdiffusion. Section 5.2 presents the magnetic properties of the Fe films with emphasis on the magnetoelasticity of the samples. The magnetoelastic stress results indicate a peculiar dependence of the magnetoelastic coupling of Fe on Ag(001) on Fe thickness. Furthermore, we found that magnetoelasticity is strong influenced by the Fe deposition temperature.

5.1   Stress and structure

Growth and morphology of Fe films on Ag(001) were intensively investigated. Fe/Ag(001) is a complex system, and the decisive influence of temperature and deposition rate on the film properties has been identified before [33, 35, 55–59, 153–160]. Critical aspects are not only the growth mechanism, but also the role of interface interdiffusion. The growth temperature triggers interdiffusion, which results in interface intermixing and Ag floating on top of the Fe film. I refer to this process as Ag segregation. In this thesis, I revisit this system. We provide new insights from stress measurement during growth. These novel results contribute to the understanding of the growth processes. Our results shed new light on interdiffusion, and its impact on growth mode, interfacial intermixing and Ag segregation for Fe on Ag(001).

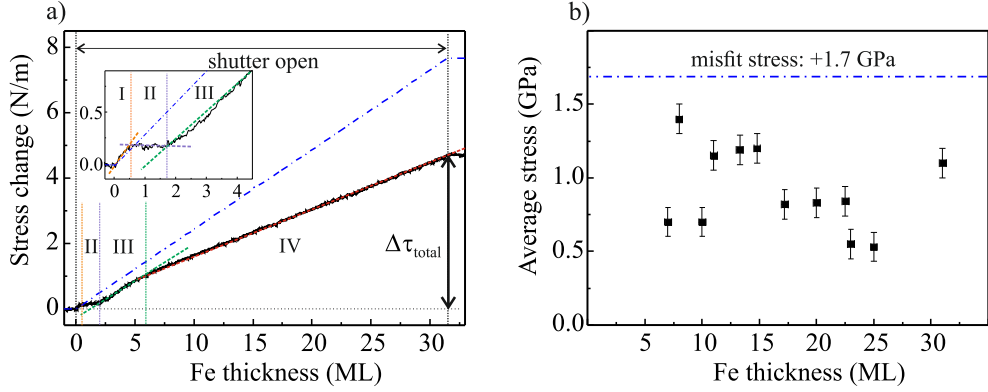Here, film stress was measured for growth at low (200 K) and at room

Figure 5.1: a) Stress measurement during deposition of an 32 ML Fe film on Ag(001) at 298 K. The black dashed vertical lines show the interval of Fe deposition and the colored dashed vertical lines highlight regions with the slope of the stress curve changes. The blue dashed-dotted line represents the calculated stress expected from epitaxial misfit of $+0.8$ % as $+1.7$ GPa. The inset is a zoom-in of up to 5 ML of Fe. b) Average stress calculated from the total stress change $\Delta\tau$ during deposition divided by the total thickness of Fe ($\tau_{\mathrm{avy}} = \Delta\tau_{\mathrm{total}}/t_{\mathrm{Fe}}$). The blue dashed-point line represent the calculated misfit stress of $+1.7$ GPa. 1 ML: 12.22×10^{14} cm^{-2}; $t_{\mathrm{Fe}} = 1.43$ Å.

(298 K) temperature with a fixed Fe deposition rate of 1 Å/min. I compare the stress results of these two temperatures to elucidate the processes involved in the growth of Fe on Ag. The Fe films were investigated in a thickness range of $7 - 32$ ML. Moreover, a concise argument of the influence of growth temperature on the magnetoelasticity is presented in Section 5.2.

The stress change during growth of a 32 ML Fe film on Ag is presented in Fig. 5.1a. The expected stress due to its misfit is represented by the dashed-dotted blue curve. The black curve depicts the measured stress change during Fe deposition. The zoom-in shows the stress during the initial deposition of up to 5 ML Fe for clarity.

The film stress during epitaxial growth can be calculated from the mismatch of the unit cells. From Eq. 2.3, the misfit between bcc Fe and fcc Ag(001) is calculated as $\eta = (a_{\mathrm{Ag}/\sqrt{2}} - a_{\mathrm{Fe}})/a_{\mathrm{Fe}}$, due to the 45° rotation of the Fe unit cell on Ag(001). The lattice constant is given as $a_{\mathrm{Ag}} = 4.085$ Å, and $a_{\mathrm{Fe}} = 2.866$ Å, and the misfit results in $\eta = +0.8$ % [123]. The misfit gives rise to an expected stress calculated from Eq. 2.4 of $+1.7$ GPa.

The film stress curve, in Fig. 5.1a, clearly deviates from the calculated misfit stress. Close inspection of the first stage of deposition reveals a non-monotonic stress behavior. The curve shows changes in slope at 0.5, 2, and

44

5 ML as identified by the separated regions I, II, III, and IV. Next, each region is presented in detail.

Region I represents the beginning of the deposition. The stress curve shows a positive slope, which represents a tensile stress of the order of +1.9 GPa. The stress from the slope of the curve reveals a slightly larger stress as compared with the calculated misfit stress of +1.7 GPa. This tensile stress is almost constant, and lasts up to a Fe coverage of 0.5 ML. In region II the stress a small compressive stress is observed. The negative slope of the curve is equivalent to a compressive stress of −0.05 GPa. The change of the stress sign during deposition demonstrates a clear deviation from the epitaxial misfit stress. The inversion of slope is measured up to 1.8 ML Fe deposition. In region III, from 1.8 to 5 ML, the curve returns to a positive slope, indicating tensile stress. The dashed green line on the curve shows a similar slope as the calculated misfit stress. The green line represents a tensile stress of +1.8 GPa. This value is very close to the calculated misfit stress of +1.7 GPa. However, for films thicker than 5 ML the slope changes again. In this region IV the slope is reduced, and a tensile stressof +0.9 GPa is observed up to the end of the deposition. Due to this reduced slope, the total stress change $\Delta\tau_{\text{total}}$ results in a smaller value as compared with the calculated misfit stress. Consequently, the average stress is also smaller than expected from misfit arguments.

The average stress is the total stress change $\Delta\tau_{\text{total}}$ divided by the thickness of the film t_{Fe}. Therefore, the unit of the average stress is GPa. The average stress of this 32 ML Fe film, presented in Fig. 5.1a, is +1.0 GPa. This is less than expected from the calculated misfit stress of +1.7 GPa. The average stress of each film deposition is calculated in order to investigate the dependence of magnetoelastic coupling on average film stress, which is related to the average film strain.

Figure 5.1b shows the calculated average stress for different thicknesses of Fe. All values are below the calculated misfit stress, represented by the dashed-dotted blue line. The values show no clear trend with Fe thickness, rather a random distribution is observed. To shed light on the understanding of stress results, an analysis of the film structure and composition is required.

LEED images and Auger spectra obtained after deposition of the Fe films on Ag(001) are presented in Fig. 5.2. Figure 5.2a shows Auger spectra of Fe on Ag for selected Fe thickness. The spectra show the Ag-MNN peaks at 266, 304, and 356 eV and the Fe-LMM peaks at 598, 650, and 703 eV [152]. This means that both Ag and Fe are present near the surface. For a quantitative analysis of the AES measurements the Ag-MNN/Fe-LMM ratio of Auger peaks intensity is extracted. The peaks used to obtain the ratio are at 356 eV (Ag-MNN) and at 651 eV (Fe-LMM) on Fig. 5.2a. The values are given with

the color code of the spectra. Surprisingly, the ratios Ag/Fe remain almost constant. Naively, a reduction of this ratio was expected with increasing Fe film thickness. This reduction is not observed, but rather a constant value is obtained for films as thick as 30 ML. A 30 ML Fe film is more than 4 nm thick, and this should reduce considerably the likelihood of electrons from the Ag substrate to penetrate to the surface. This is, indeed, a surprise in view of the short mean free path of ≈ 2 nm of electrons with energy of 300 eV in a solid [161].

In order to confirm the nature of the Ag signal, I selected an even thicker Fe film of 80 ML, with a thickness of 11 nm and performed AES measurements.

Figure 5.2b shows Auger spectra of a 80 ML thick Fe film grown at 298 K. The black curve represents data for the as-grown film, and the red solid line shows the spectrum of the film after 1 minute Ar-sputtering. This short time of bombardment exposure assures the removal of ≈ 1 atomic layer of the surface. The highlighted region on Fig. 5.2b identifies the energy region of the Ag-MNN AES line (at 356 eV). A clear Ag peak in the as-grown film is visible, although the Ag/Fe ratio is considerately reduced as compared with the 30 ML film. The observation of the Ag peak itself confirms the presence of Ag atoms near the surface. Further evidence is obtained after a short sputtering on the surface, which is expected to remove the topmost layer of the film. The spectrum after this short sputtering shows the absence of the Ag peak. This indicates that the Ag atom are removed from the top most layer surface. This experiment reveals clear Ag surface segregation. The amount of Ag segregation decreases with increasing Fe thickness, for this thicker film of 80 ML very short sputtering time is needed to remove the Ag atoms. This experiment was performed for films as thicker as 30 ML, which required a exposure time of 1 min. in order to remove the Ag atoms. From the sputtering time of 1min. we estimate that in 30 ML Fe film thickness approximately one atomic layer of Ag floates on top of the Fe film.

Additional insights into the development of the film is provided by LEED measurements. Figure 5.2c shows LEED diffraction patterns at 144 eV of Fe films of 8, 13, 30, and 80 ML thickness on Ag(001). The images show (1×1) diffraction patterns for all film thicknesses. This sequence of LEED images demonstrates the quality of the films. Films up to 30 ML of Fe do not show variations in intensity or sharpness of the spots, the diffraction pattern looks very similar. For the thickest film of 80 ML, the intensity of the spots is visibly decreased, where as background intensity is increased (the spot contrast is reduced). This indicates a partial loss of the long range crystalline order as the film thickness increases. The similarity of the LEED diffraction up to 30 ML suggests a good quality epitaxial growth of the films.
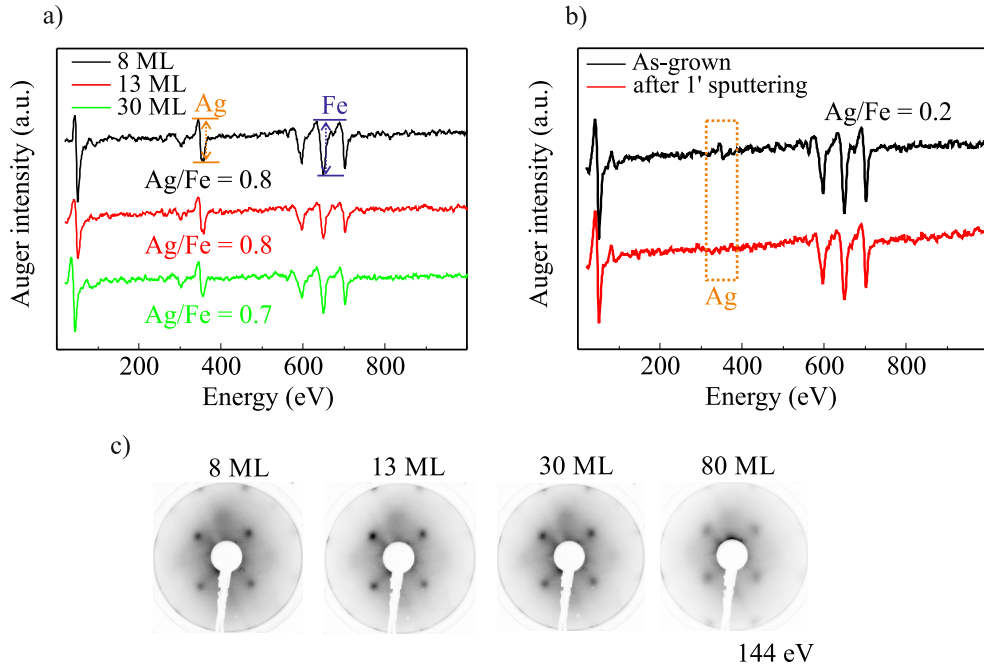
Figure 5.2: a) Auger spectra measured on Fe films on Ag(001) for selected thicknesses. Ag/Fe ratio from intensity peaks are indicated at each spectrum (Ag-MNN 356 eV and Fe-LMM 651 eV [152]). b) Auger spectra 80 ML Fe/Ag(001) as-grown, and after 1 minute of Ar-sputtering. The presence and absence of the Ag peak is highlighted. c) LEED images at 144 eV of Fe films as a function of thickness. The LEED image is inverted, dark means high and white means low intensity, and Auger spectra are vertically shifted for the sake of visualization.

As mentioned before, the Fe/Ag system is extremely affected by the temperature. The interdiffusion and segregation processes are known to be thermally activated [153, 154, 156, 159, 162, 163]. To further study the impact of temperature, I carried out preparations of Fe films on Ag at a low temperature of 200 K. Figure 5.3a shows the comparison of the stress change during growth of 13 ML of Fe at 298 K and at 200 K. The blue dashed-dotted line is the calculated misfit stress, the black curve represents the stress for growth at 298 K (room temperature), and the red curve is the stress for growth at 200 K.

Growth at 200 K, in contrast to 298 K growth, shows a rather monotonic stress behavior. The stress behavior is highlighted in three regimes where the curve changes its slope. Region I represents the region of constant slope of the stress just after the evaporator shutter is opened. This region shows an immediate tensile stress for submonolayer thickness (0.5 ML). This positive
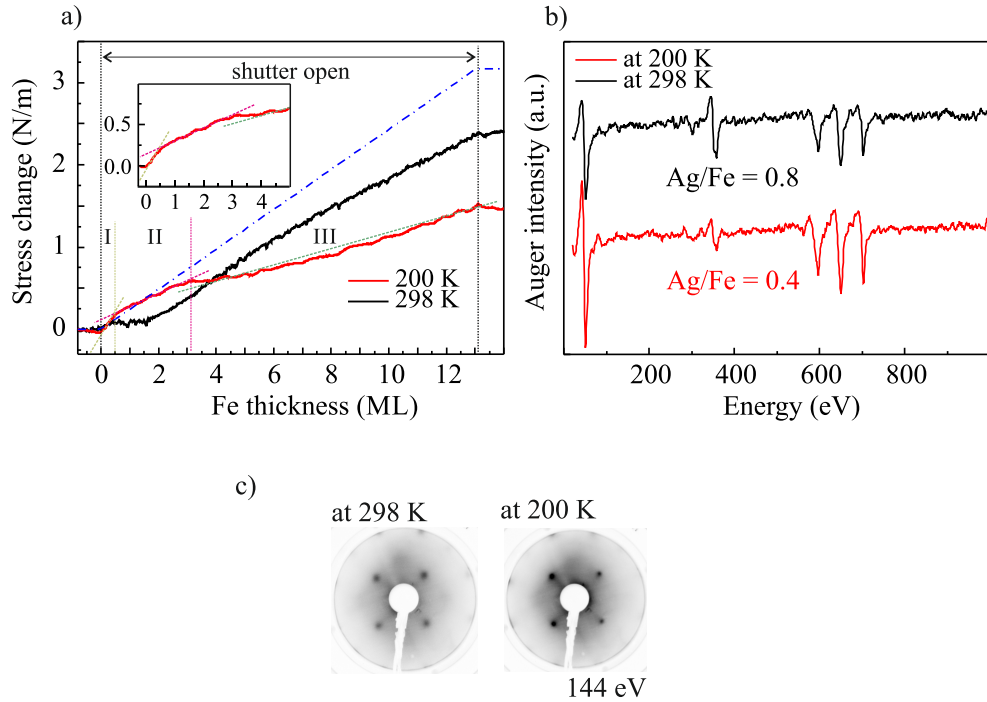
Figure 5.3: a) Stress measurement during deposition of 13 Fe ML on Ag(001) at different temperature. The dashed vertical lines show the interval of Fe deposition in black and the colored lines identify the regions of changing slope. The blue dashed-dotted line represents the stress calculated from epitaxial misfit. The inset is a zoom-in of up to 5 ML of Fe growth at 200 K. b) Auger spectra of 13 ML Fe on Ag(001) at different deposition temperature, and c) LEED images at 144 eV of the given Fe films. The LEED image is inverted, dark means high and white means low intensity and Auger spectra are vertically shifted for the sake of visualization.

slope results in a tensile stress of +2.7 GPa. The next region, II, shows a positive slope up to 3 ML of Fe. The stress measured in this regime is tensile +1.0 GPa. The slope changes again at 3 ML to a tensile stress of +0.7 GPa. The region III lasts to the end of the deposition. Thus, the film stress at 200 K presents only three regions of stress behavior, furthermore, no inversion of slope to negative sign is observed in contrast to growth at 298 K.

Elemental composition and surface structure are also impacted by the growth temperature. Therefore, AES and LEED measurements are presented in Fig. 5.3b for Fe films grown at 298 and 200 K. The Auger spectra of the 13 ML Fe films deposited at different temperatures, indeed, shows different AES peak intensities. The values of the Ag-MNN/Fe-LMM ratio are shown in

Fig. 5.3b with the color code of their respective spectrum. The change of the Ag/Fe ratio indicates a distinctly different distribution of Fe and Ag atoms near the surface. The Fe film with 13 ML is not thick enough to cover the Ag signal of the substrate completely, but the Ag/Fe ratio is twice as high for growth at 298 K. This suggests less Ag near the top surface at lower growth temperature as compared to higher growth temperature for films of the same thickness. The LEED images of each sample are presented on Fig.5.3c. The diffractions show (1×1) patterns for both growth temperatures. Although the LEED images look similar, the film grown at 200 K shows a sharper and more intense diffraction pattern than for growth at 298 K. The findings are discussed in Section 8.2.1, in view of the growth mode and interdiffusion of the Fe/Ag system.

In conclusion, the stress measurements are an useful tool to characterize the growth of Fe films on Ag(001). The film stress during deposition at 298 K, showed a very peculiar behavior. The measured stress deviates from the calculated misfit stress. An intriguing compressive stress was observed for thin films up to 2 ML. This negative slope was not observed for low growth temperature (200 K).

Our stress results in combination with *in-situ* AES and LEED provide new insights into the structure and morphology of Fe films on Ag(100). For room temperature growth (298 K), evidence for Ag segregation is observed by AES measurements. In contrast, at 200 K growth, the Ag/Fe ratio and the LEED diffraction show small deviations, which is a reflection of the different growth processes observed by film stress change.

The discussion of the stress results are presented in Section 8.2.1. The discussion addresses the growth mode in both temperature with emphases on the interdiffusion reported in this system [33,153]. Furthermore, the influence of temperature on the magnetoelasticity of this films due to the change in morphology is addressed in Section 8.3. The magnetoelastic stress results of Fe films grown at 298 K and 200 K are presented next.

5.2   Magnetic properties

In this Section, I present the magnetic measurements of Fe monolayers on Ag(001). This includes MOKE results, and the main focus is on the magnetoelasticity of Fe on Ag(001) at different Fe thickness. We found a non-monotonic behavior of the magnetoelastic coupling coefficient B_2 as a function of Fe thickness. Our results suggest an almost oscillatory behavior of B_2 with respect to the Fe film thickness. This novel finding may suggest a quantum confinement effect in magnetoelasticity.
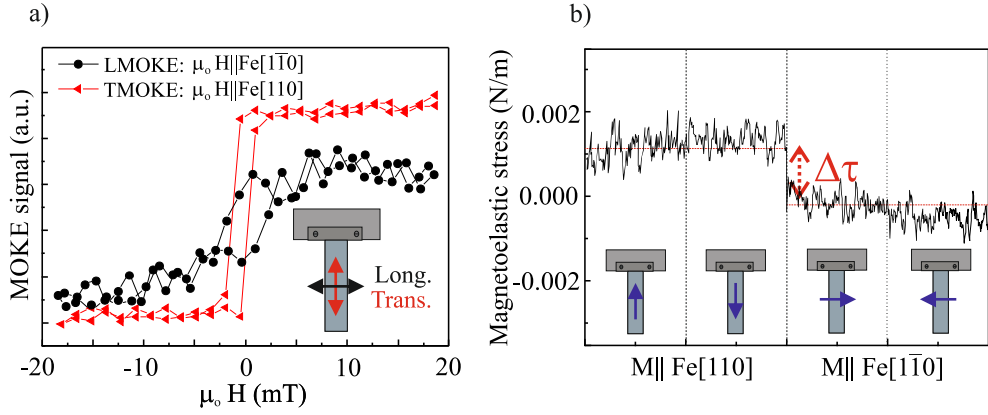
Figure 5.4: a) Longitudinal and transversal MOKE of 8 ML Fe on Ag at 298 K. b) Magnetoelastic stress of (8 ML) Fe/Ag. The change of curvature is induced by switching the magnetization in the sample plane from along the length (M||Fe-[110]), up and down, to along the width of the crystal (M||Fe-[1$\bar{1}$0]), left and right. The sketches indicate the magnetization direction in relation to the crystal layout. Up and down and left and right are magnetoelastically equivalent.

Figure 5.4a shows hysteresis curves of the magnetization of an Fe film of 8 ML on Ag(001) as a function of the external magnetic field in two MOKE geometries, longitudinal (black) and transversal (red). The MOKE results indicate that the magnetization is in-plane. MOKE indicates that the sample magnetization is saturated at an external magnetic fields of ± 10 mT. Consequently, during experiments of magnetoelastic stress, magnetic fields of 30 mT applied along the longitudinal and transversal directions assure a saturated magnetization, aligned with the external field.

The spin reorientation transition (SRT) of Fe on Ag, where the magnetization orientation rotates from out-of-plane to in-plane orientation, is reported to occur at 4-6 ML of Fe [163–167]. A proper orientation of the magnetization of the sample and the external magnetic field is necessary in order to measure the magnetoelastic stress. The cantilever technique exploited in this work to measure the magnetoelastic stress can also be used as a magnetometer, as an external deflecting field $\mathbf{B}$ acting on the total magnetic moment of the film $\mathbf{m}_{\mathrm{total}}$ resulting in a torque ($\mathbf{T} = \mathbf{B} \times \mathbf{m}_{\mathrm{total}}$) [51]. To avoid conflicting results, I performed all measurements for films thicker than 6 ML of Fe, in which the magnetization lies in the film plane [159, 165–167], as verified by MOKE.

Figure 5.4b shows a typical measurement of the magnetoelastic stress of an Fe film of 25 ML grown on Ag(001) at room temperature. The technical
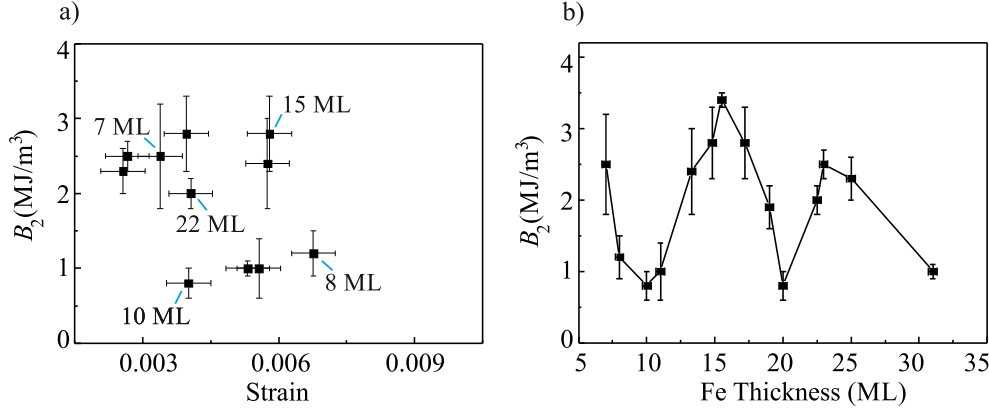
Figure 5.5: Collection of the magnetoelastic stress coefficients (B_2) of Fe films of different thickness grown on Ag(001) at room temperature. In (a) the magnetoelastic stress is plotted as a function of the strain in the Fe film, as calculated from stress curves, e.g., Fig. 5.1. In (b) B_2 is plotted as a function of the Fe film thickness.

aspects of the measurement of magnetoelasticity of thin films are described in Section 3.1. Here, the the change curvature is monitored while the magnetization is switched along the length and width of the crystal. This reorientation of the magnetization is induced by an external magnetic field. The stress change ($\Delta\tau$) is analyzed by Eq. 3.6, and this provides the magnetoelastic coupling coefficient B_2.

I perform magnetoelastic stress measurement of several Fe films grown on Ag(001) at room temperature as a function of Fe thickness. Figure 5.5 shows two compilations of the measured values of B_2 as a function of the average in-plane strain in the film (Fig. 5.5a), and as a function of the film thickness (Fig. 5.5b). The average in-plane strain is obtained from the average stress during growth of Fe films, from the results presented in Fig. 5.1b, Section 5.1.

In Fig. 5.5a, the data points appear to be randomly distributed in the graph, no clear trend or dependence of B_2 on film strain is observed. In contrast, in Fig. 5.5b a clear trend of B_2 with film thickness is noticeable. The values of B_2 present a non-monotonic behavior with increasing Fe thickness. Our results show a rather oscillatory tendency of B_2. B_2 changes from 1 to 3 MJ/m^3 over a thickness scale of about 5 ML, repeatedly. In Section 8.3, I discuss the results of B_2 in view of quantum well states in the Fe layer.

To investigate the influence of Ag segregation on magnetoelastic coupling, I performed magnetoelastic stress measurement of Fe film prepared at the lower temperature(200 K). In the previous Section 5.1, I showed the in-
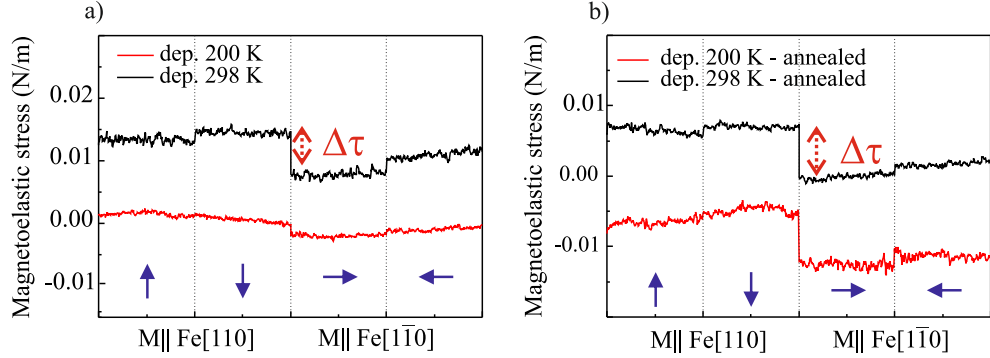
Figure 5.6: a) Magnetoelastic stress curves measured at room temperature of 13 ML Fe grown on Ag(001) at different temperatures. b) after annealing at 343 K for 30 minutes. Arrows represent variation of stress (red) and the in-plane magnetization of the sample (blue). The curves are vertically translated to show clear distinction of the effect.

fluence of temperature on the interdiffusion and segregation of Ag upon Fe deposition. Segregation is understood to be hampered at low temperatures and less Ag is expected on top of the Fe film [153]. A direct comparison of magnetoelastic stress of samples grown at different temperature is presented next.

Figure 5.6a shows measurements of magnetoelastic stress of Fe films of 13 ML deposited at 298 (black curve) and at 200 K (red curve) on Ag(001). The arrows indicate magnetization directions and change of stress ($\Delta\tau$) of the curves. The impact of the deposition temperature on $\Delta\tau$ is clear in measurements of as-grown films (Fig. 5.6a). The value of B_2 for low temperature (200 K) deposition is 1.3±0.3 MJ/m^3 in contrast to 2.4±0.8 MJ/m^3 for sample grown at room temperature (298 K). This result indicates a reduction of magnetoelastic coupling stress on samples grown at 200 K. Our analysis in Section 5.1 reveals that the film differs for both preparations. My suggestion is that the slight change in growth mode, the segregation, and the higher interfacial intermixing impacts the magnetoelastic response of the film.

Annealing the films up to 343 K for 30 min changes the magnetoelastic stress for both cases, growth at 298 and 200 K. The magnetoelastic curves of the films after annealing are presented in Fig.5.6b. The resulting values of B_2 are 3.2±0.5 MJ/m^3 and 3.3±0.5 MJ/m^3 for 298 and 200 K growth, respectively. The similarity of B_2 after thermal treatment for both growth conditions suggests the impact of film morphology on ME. The interdifussion is increased with increasing of temperature. However, the annealing temperature of 343 K limits the amount of interfacial intermixing and Ag se-

52

gregation in the films, independent of the original sample preparation. The influence of intermixing at the interface of Fe films on Ag(001) will be further discussed in Section 8.3.

In summary, MOKE and magnetoelastic coupling measurements of Fe film on Ag(001) were presented in this section. The magnetoelastic coupling coefficients B_2 of Fe films grown at 298 K show a peculiar dependence with Fe thickness. The trend of B_2 with film thickness is a surprising result. This finding sheds first light on novel contributions to the magnetoelastic coupling of thin films. The oscillatory-like behavior of B_2 with increasing Fe thickness may indicate that magnetoelasticity is influenced by electronic quantum confinement in the Fe film. The discussion on thickness-dependent magnetoelastic coupling is presented in Section 8.5. We found that B_2 of Fe films grown at low temperature, 200 K, is smaller as compared to films grown at room temperature (298 K). This hints at a dependence of magnetoelasticity on film morphology. Compelling evidence is given by the observed change of B_2 after a thermal treatment. After the annealing the magnetoelastic response increased considerably. The discussion of the influence of interface structural changes of the film induced by temperature on the magnetoelastic coupling is presented in Section 8.3.

The variation of ME as a function of Fe thickness in the Fe/Ag system rises some questions concerning the impact of electronics effects such as quantum well state (QWS). The quantum confinement in ferromagnetic layers, like Co on Cu, Co on Pd, and Fe on Ag have been reported [10, 103, 168–171], and its impact in the magnetic-crystalline anisotropy has been discussed [168, 172]. However, the observation of an impact of QWS on magnetoelasticity is novel, and to the best of my knowledge, it has never been reported before. Its very nature is an open question, which we address in Chapter 8.

Chapter 6

Film stress and magnetoelastic stress of Fe on Au (001)

In this Chapter, I present experimental results on film stress and magnetoelastic stress of epitaxial Fe films on Au(001). Section 6.1 describes the film stress during growth of these Fe films, following the sample preparation as detailed in Section 3.4. The effect of growth temperature on film stress is also presented. In Section 6.2, I report on the magnetic properties, with focus on the magnetoelastic coupling of these samples. Our observations suggest that the change of growth temperature impacts magnetoelastic coupling of Fe on Au(001) only little. I find that ion bombardment changes the ME coupling significantly, and the effect depends on the ion mass.

6.1   Stress and structure

Many structural properties that I discussed in the previous Chapter 5 are not only specific for Fe films on Ag(001), but they are characteristic also for the Au substrate. The growth of Fe on Au is affected by interdiffusion, which can result in interfacial intermixing and segregation. The presence of Au segregation impacts the growth mode of the Fe film [33, 38–42, 60–62, 173]. Here, I employed stress measurements, Auger spectroscopy, and LEED to investigate the growth of Fe films on Au(001) at room temperature and at different growth temperatures. Our results give an estimate of the surface segregation from an analysis of the surface composition. The peculiar development of the surface structure as probed by LEED complements the stress measurements.

The stress change during growth of a 30 ML Fe film on Au is presented in Fig. 6.1a. The stress curves show the same features at specific thicknesses
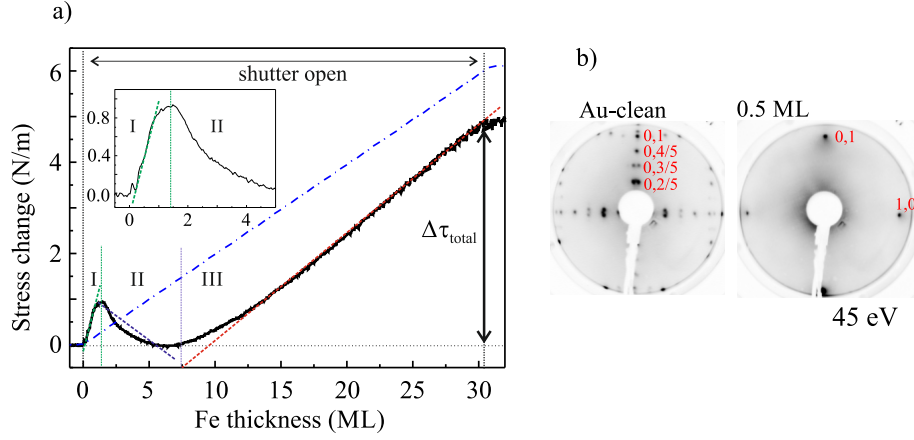
Figure 6.1: a) Stress measurement during deposition of 30 ML Fe on Au(001) at 298 K. The black dashed vertical lines show the interval of Fe deposition and the colored dashed vertical lines highlight the change of slope. $\Delta\tau_{\text{total}}$ represents the total stress change. The blue dashed-dotted line represents the calculated stress expected from epitaxial misfit of +0.6 %.The inset is a zoom-in of up to 5 ML of Fe. 1 ML: 12.22×10^{14} cm^{-2}; t_{Fe} = 1.43 Å. b) LEED diffraction pattern at 45 eV of the clean Au(001) crystal and after 0.5 ML of Fe deposited. The LEED image is inverted, dark means high and white means low intensity for the sake of visualization.

for all total film thicknesses in the range 6−30 ML. The stress change with increasing Fe thickness is given by the black curve, in Fig. 6.1a, and the blue dashed-dotted line indicates the calculated misfit-induced stress. The inset shows a zoom-in of the film stress up to 5 ML of Fe deposition.

The misfit of bcc Fe on fcc Au(001) is calculated from Eq. 2.3 as $\eta = (a_{\text{Au}/\sqrt{2}} - a_{\text{Fe}})/a_{\text{Fe}}$. The lattice constants are a_{Au} = 4.078 Å and a_{Fe} = 2.866 Å, which gives η = +0.6 % [173]. The stress induced by this misfit is calculated with Eq. 2.4 and results in a tensile stress of +1.4 GPa.

The film stress, in Fig. 6.1a, clearly deviates from the calculated misfit stress. The stress curve during Fe deposition reveals a non-monotonic change with increasing thickness. The curve shows changes in slope at 1.5 and 7.5 ML as identified by the separated regions I, II, and III. Next, each region is presented in detail.

Region I represents the stress just after the evaporator shutter was opened up to 1.5 ML of Fe. The curve shows a positive slope depicted by the green dashed line. The positive slope indicates that a tensile stress is measured. This first slope gives a tensile stress of +5.5 GPa. The tensile stress is four times larger than the calculated misfit stress of +1.4 GPa. This indicates an

additional contribution to the stress. The stress in this low coverage regime could be related to surface stress changes. Region II shows the change in slope a negative value. The negative slope of the curve is equivalent to a compressive stress of -1.3 GPa. This compressive stress lasts up to 7.5 ML. A change of sign of the stress during deposition demonstrates a clear deviation from the epitaxial misfit stress. The last region marked as III reestablishes a positive slope. Region III, shows a tensile stress of $+1.5$ GPa up to the end of deposition. This slope, indicated by the red dashed line, is comparable to the misfit stress. The deviation of the film stress from the calculated misfit stress in the first 8 ML is evident. Due to the region II, the total stress change $\Delta\tau_{\mathrm{total}}$ lies below the misfit stress curve at 30 ML of Fe. Consequently, the average stress is also smaller than expected from misfit arguments. On average, the film stress is $\Delta\tau_{\mathrm{total}}/t_{Fe} = +1.1$ GPa.

However, the situation in region I is more complex. The clean Au(001) crystal exhibits the characteristic surface reconstruction identified by the (1×5) diffraction pattern. We observe that this reconstruction is lifted with Fe deposition. Figure 6.1b shows LEED images of the clean Au crystal and after 0.5 ML of Fe deposition. The red numbers identify the diffraction position in reciprocal space. In the clean Au crystal a (1×5) diffraction pattern is visible. After 0.5 ML of Fe deposition, LEED shows a (1×1) pattern. This indicates that the deposition of 0.5 ML of Fe is sufficient to lift the surface reconstruction of the Au surface. The lifting of the Au surface reconstruction is discussed further in Section 8.2.2.

To gather more information on the surface structure and its chemical composition, LEED and AES experiments are performed. The results are presented next.

Figure 6.2a presents LEED images of Fe films on Au(001) at 58 eV. The 3 ML Fe film shows a (1×1) LEED pattern, where the diffraction spot intensity is weak. With increasing Fe thickness the diffraction spots get sharper and more intense. This indicates a structural improvement of the surface. This quality of the LEED pattern is kept up to 30 ML of Fe deposition.

Figure 6.2b presents Auger spectra taken after Fe deposition on Au at 298 K for different thickness. The presence of peaks of Au-NVV at 69 eV and Fe-LMM at 598, 650, and 703 eV even for films as thick as 30 ML Fe indicates that both materials, Au and Fe, are found near the surface [152, 174]. I analyzed our AES data in view of the relative amount of both elements given by the ratio of Auger intensities Au-NVV/Fe-LMM. The ratios are given in Fig. 6.2b. The Au/Fe ratio decreases as a function of Fe thickness up to 25 ML and remains constant for thicker films. This finding suggests a constant amount of Au floating on top of the thicker Fe film. An estimate of the relative amount of Au floating on top is obtained in this Section. But
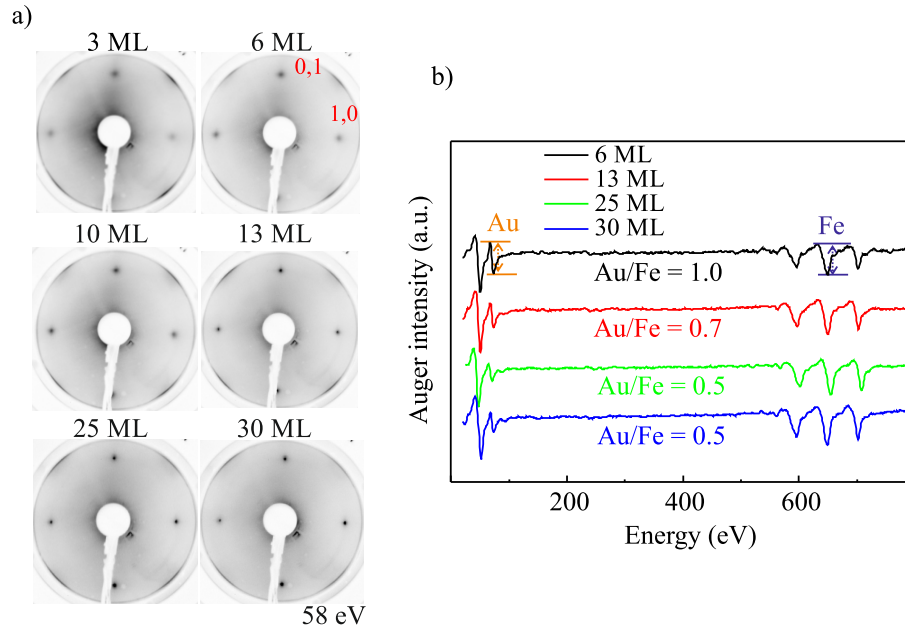
Figure 6.2: a) LEED diffraction pattern at 58 eV of Fe films on Au(001) with different thicknesses. The diffraction reveals a (1×1) pattern. b) Auger spectra of Fe films of different thickness grown on Au(001) at 298 K. Au/Fe ratios of the intensity peaks are given. The LEED image is inverted, dark means high and white means low intensity and Auger spectra are vertically shifted for sake of visualization.

first, I show the results for different growth temperature.

Since the Au/Fe ration remains constant at 25 ML Fe, I choose this Fe thickness to investigate the temperature dependence of film stress, LEED, and Auger measurements. Figure 6.3 shows a direct comparison of the stress during deposition at different temperatures. The black, red and green solid lines correspond to stress measurements at 298, 375 (HT) and 200 K (LT), respectively. The blue dashed-dotted line represents the calculated misfit stress, and the inset shows a zoom-in up to 5 ML deposition. The regions I, II, and III separate regions of different slope of the 298 K growth for sake of comparison. The overall stress behavior is similar for all curves. A strong initial tensile stress is followed by a compressive stress, and then tensile stress for higher thickness is observed, as described before.

A close inspection of the low temperature, 200 K, growth stress curve reveals a negative slope of −2.3 GPa compressive stress up to 8 ML. Then, a tensile stress of +2.0 GPa persists up to the end of deposition. However, for stress measurements at 375 K, the compressive stress of −3.4 GPa starts at

58
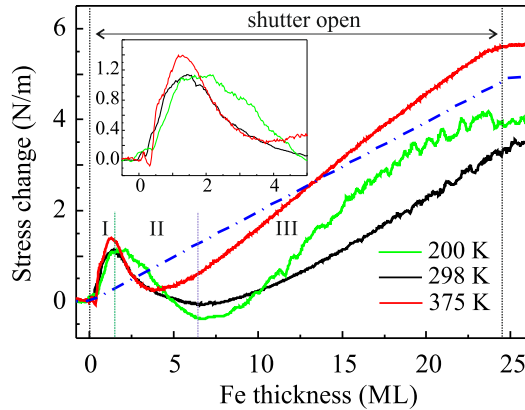
Figure 6.3: Stress measurement during deposition of Fe on Au(001) at different temperatures. The inset is a zoom-in up to 5 ML of Fe deposition.

1.5 ML and persists only up to 4 ML of Fe. The region II for the black curve shifts toward thin films for HT depositions. And a tensile stress of +1.9 GPa is observed for films thicker than 5 ML. The average stress for growth at 200 K and 375 K are +1.2 GPa and +2.3 GPa, respectively. Note that in both cases the average stress is larger than for 298 K depositions (+1.1 GPa). These differences of the stress behavior indicate a non-monotonic dependence of average stress with growth temperature. The impact of the growth temperature on the morphology of these films are reflected in the LEED and Auger measurements as well. The results are presented next.

Figure 6.4a shows Auger spectra of the 25 ML Fe film on Au(001) deposited at different temperatures. The Auger peaks at 69 eV (Au-NVV) and at 651 eV (Fe-LMM) are indicated in the graphic. The Fe film grown at 200 K (green curve) shows only a very small peak in its Auger spectrum. On the other hand, films grown at 375 and 298 K show distinct Au peaks. We observe a clear trend of the Au/Fe ratio with increasing growth temperature. With increasing growth temperature the Au/Fe ratio increases.

Figure 6.4b shows LEED images of Fe films prepared at different temperatures measured at two different energies, 58 and 92 eV. The growth temperature are shown on the left side of the images. LEED images were obtained at the growth temperature to avoid further thermal effects. The column of LEED images at 58 eV displays faint spots becoming more intense as a function of temperature, indicative of well ordered films. The pattern at 92 eV shows sharper spots and a new collection of spots becomes visible with increasing growth temperature. The pattern of the film prepared at 200 K shows few distinct diffraction spots of similar intensity. For deposition at
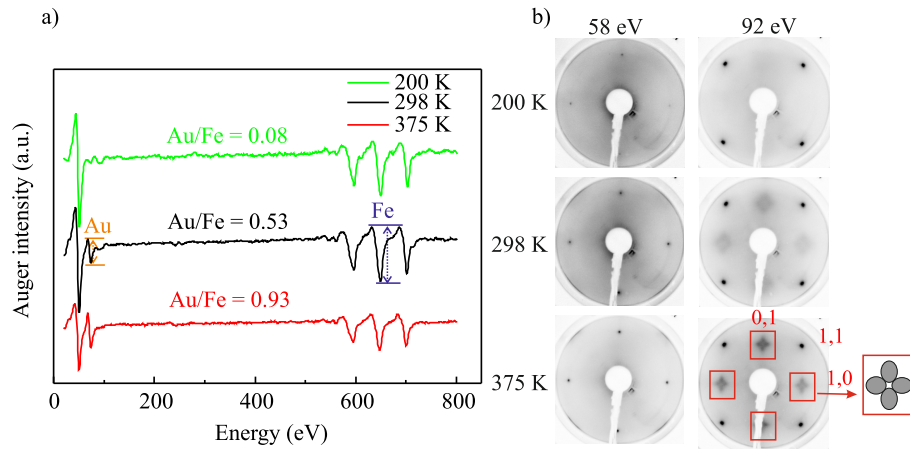
Figure 6.4: a) Auger spectra of 25 ML Fe/Au(001), deposited at different temperatures. The Au peak at 69 eV and the Fe peak at 651 eV are considered in the intensity Au/Fe ratio. Auger spectra are vertically shifted for sake of visualization. b) Corresponding LEED images at 58 and 92 eV. A new set of grouped diffraction spots round (1.0) and (0.1) is identified by the red rectangle and the sketch. The LEED image is inverted, dark means high and white means low intensity.

298 and 375 K additional diffraction spots appear around the (1,0) and (0,1) positions.

This difference in Au/Fe ratio and LEED diffraction could be assigned to Au segregation with increasing temperature. These grouped diffraction spots are attributed to the Au superlattice [175]. A more detailed discussion about the change in morphology of Fe/Au(001) by varying growth temperature is addressed in Section 8.2.2.

A question that rises here is: How much Au is floating on top of Fe films prepared at room temperature? The experiment of removing the top most layers of the film by sputtering is performed. These experiments are presented for different sputtering ions in Section 6.2. In short, the sputtering was successfully applied to remove Au from the samples surfaces prepared at 298 K, as is shown in Fig. 6.9a. This suggests an estimated Au coverage of order of one atomic layer. Another simple experiment that enables a more precise estimate of the amount of Au on top is performed. I benefit from a 25 ML Fe film deposited at 200 K that shows a very small AES Au/Fe ratio, an order of magnitude smaller as it is shown in Fig. 6.5 top. I deposit a known amount of Au on top. The Au evaporation has been performed at 298 K. The calibration was performed before the evaporation by a quartz balance. With 1 ML of Au and $t_{Au} = 2.04$ Å, which corresponds to a density

60
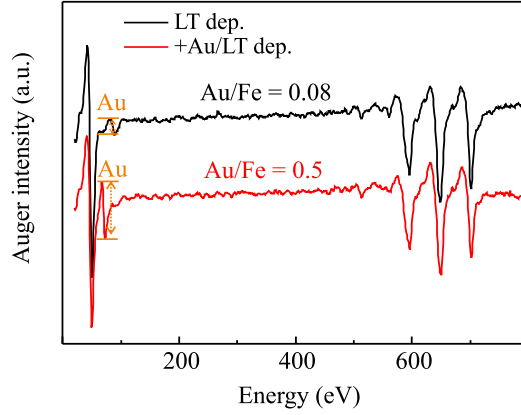
Figure 6.5: Auger spectra of Fe 25 ML grown on Au(001) at 200 K before and after deposition of 0.5 ML of Au. The Au/Fe ratio of 0.5 is obtained after Au deposition. Auger spectra are vertically shifted for sake of visualization.

of 1 ML: 12.02×10^{14} cm^{-2}, I conclude that after 0.5 ML of Au deposited the nominal Au/Fe ratio of 0.5 is reached. This ratio of 0.5 is also found for 25 ML Fe film prepared at 298 K. The calibration of Au before the deposition indicates that an amount of 0.5±0.05 ML of Au is floating on top of Fe film, when prepared at 298 K. This value is in agreement with previous works on Au segregation in Fe/Au system [33, 40].

In conclusion, the stress measurements were performed to characterize the growth of Fe films on Au(001). All growth temperature lead to similar non-monotonic stress behaviors. In contrast with Fe/Ag films, the variation of growth temperature did not impact the formation of the compressive stress region. The changes on the film structure and elemental composition are shown in the Auger and LEED results after film deposition. The AES measurements display larger Au/Fe ratios with increasing growth temperature. I estimate that 0.5 ML Au float on top of 25 ML Fe film deposited at 298 K. From LEED measurements we assessed the Fe thickness necessary to lift the Au-(1×5) reconstruction. The reconstruction is totally lifted just after 0.5 ML of Fe coverage. My results on the dependence of stress on growth temperature indicate a considerable change in surface structure. In LEED, such changes are accompanied by a new set of diffraction spots. These additional spots are ascribed to a specific ordered Au layer on top of Fe. These unexpected LEED results and the film stress of these Fe films are discussed in Section 8.2.2 in view of the Fe growth mode and interdiffusion.

6.2   Magnetic properties

In this Section, I present the results of MOKE and magnetoelastic stress measurements for Fe/Au(001). We found, in contrast to the Fe/Ag(001) system, a linear dependence of magnetoelastic coupling coefficient B_1 with film strain for films deposited at 298 K. The results of growth temperature-dependend ME shows also deviation as compared with the Fe/Ag system. B_1 reveals no change with increasing growth temperature. A novel aspect, the effect of post-grown sputtering on magnetoelasticity of thin films is addressed at the end of this Section.

The magnetic anisotropy of Fe on Au(001) is well know. Fe films thinner than 5 ML show an out-of-plane, whereas thicker films show an in-plane easy magnetization [42, 176–179]. Therefore, I focus on Fe films thicker than 6 ML to study the magnetic properties. MOKE in longitudinal and transverse geometry is performed to verify the in-plane magnetization of the films.

Figure 6.6a shows hysteresis curves of the magnetization of 16 ML Fe on Au(001) as a function of the external magnetic field along two in-plane directions, longitudinal (black) and transversal (red). The hysteresis curves show a square-like hysteresis loop with full remanence. Our MOKE results confirm the previous reports [42, 176–179]. The saturation field in both configurations is lower than 10 mT.

Figure 6.6b shows a magnetoelastic stress curve of 28 ML Fe/Au(001). The arrows depict directions of the changes of magnetization of the film. The stress change upon magnetization reversal is monitored as the external magnetic field switches from along the sample length to along the sample width. The magnetoelastic coupling coefficient B_1 is obtained from the magnetization stress change $\Delta\tau_{\mathrm{me}}$ as described by Eq. 3.5, taking into account the Fe film thickness.

Figure 6.7 shows my compilation of B_1 values of Fe film with various thicknesses plotted versus the in-plane strain. The in-plane strain is calculated from the average stress during film growth, obtained from the stress curve like in Fig. 6.1. The values are negative, so the data in the lower part of the graphic are larger in magnitude. Overall, B_1 varies from -5.4 MJ/m^3 to -1.3 MJ/m^3. The values of B_1 are distributed in two regions, I and II represented in the graphic. Region I corresponds to small film strain, less than 0.3% of strain. Dispersed data points with a linear trend are observed. Note that for thinner films, where the stress is compressive, a negative in-plane strain is obtained.

The region II represents the films with strain larger than 0.3%. B_1 values become independent of the strain, showing a constant values of -1.3 MJ/m^3.
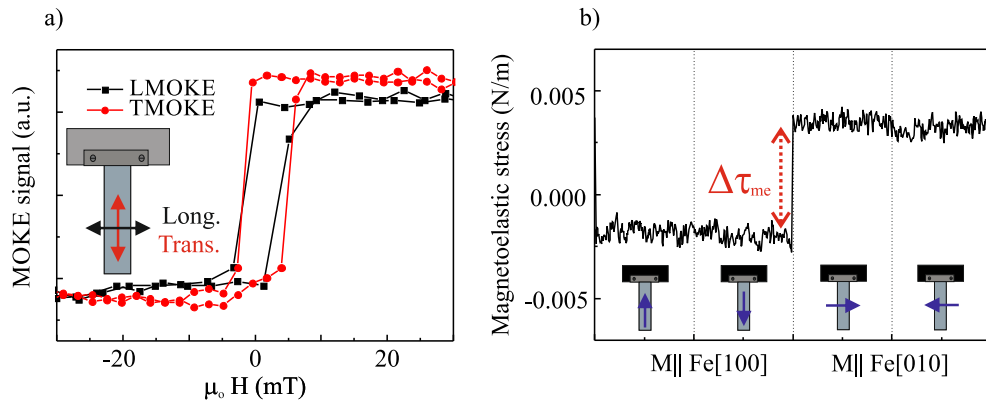
Figure 6.6: a) Longitudinal and transversal MOKE of 16 ML Fe on Au. b) Typical curve of magnetoelastic stress of 28 ML Fe on Au. The change in curvature is induced by switching the magnetization in the sample plane from along the length (M||Fe-[100]), up and down to along the width of the crystal (M||Fe-[010]), left and right, as represented by the blue arrows in the sketch.

For reference, bulk Fe has a value of $B_1 = -3.4$ MJ/m^3. The results of B_1 as a function of strain indicate a strain-dependend magnetoelasticity of the Fe films only for small strains. For larger strain, a constant B_1 is observed. This constant B_1 is observed for thicker films and still deviates from the bulk value, which suggests a persisting influence of strain on the magnetoelasticity of thin films.

We have seen above in Section 6.1 that the growth temperature has a distinct influence on the Au top coverage of the Fe film. To check the impact on magnetoelasticity, I performed magnetoelastic stress measurements on Fe films of 25 ML prepared at different temperatures. The results are shown in Fig. 6.8. Strikingly, all curves show a similar magnetoelastic stress change. Consequently, a similar value of B_1 of -1.3 ± 0.2 MJ/m^3 is obtained. This result indicates that the presence of a Au layer floating on top, which is affected by the growth temperature, does not impact the magnetoelasticity of the system directly. This puzzling result led me to perform an alternative method to study the influence of an Au top layer on the magnetoelasticity of Fe films, as discussed next.

I measured the magnetoelastic stress after removing the Au atoms from the surface of the Fe film by mild sputtering. An estimated amount of 0.5 ML of Au floating on top of films grown at 298 K was presented in Section 6.1. An effective way to remove the top most layer is by a short sputtering [62]. From Fe films prepared under identical conditions and thickness (25 ML Fe

63
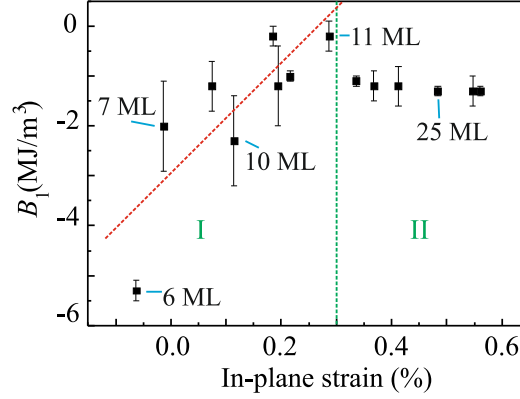
Figure 6.7: Magnetoelastic coefficients B_1, calculated from the magnetoelastic stress (Fig. 6.6b), as a function of in-plane strain. The in-plane strain is calculated from the stress during deposition.

- at 298 K), short sputtering with five noble gases: Helium, Neon, Argon, Krypton, and Xenon, was carried out.

The criterion for complete removal of Au is the absence of the Au peak in the Auger spectrum. As mentioned before, in view of the short mean free path of ≈ 2 nm of Auger electrons with typical energy of 300 eV in a solid [130], the 25 ML Fe film should screen the substrate and prevent electrons from Au to pass through to the surface. The sputtering time varied from 0.5 to 4 minutes with a typical sample current of $I_{sample} = 0.3$ μA.

Figure 6.9a shows Auger spectra of Fe films, as-grown and after short Ar-sputtering. The dashed green lines highlight the energy of Au peak position. The presence and absence of the peak (Au-NVV 69 eV) are visible in the spectra. The magnetic state of the Fe films after each sputter treatment was checked by MOKE, and I found no change in the magnetization of the film. Coercivity and the MOKE intensity remain unaffected.

Figure 6.9b shows magnetoelastic stress measurements plotted for different sputter gases used in the sputtering process. The as-grown film is also presented in the plot for sake of comparison. Every curve shows a different magnetoelastic stress. B_1 shows a variation with the sputtering element. The trend is visible in Fig. 6.9c. Note that the change in stress may be larger or smaller as compared with the as-grown sample. This indicates that sputtering affects the Fe film not only by removing the Au layer from the top. The dependence observed for B_1 on the sputtering element brings the questions concerning of the atomic radius of the elements and its impact to the sputtering process. In Section 8.4 a discussion of the implications
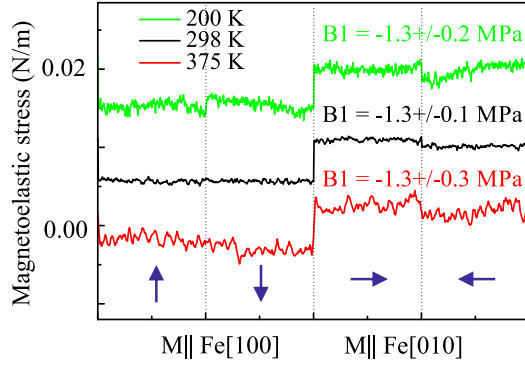
Figure 6.8: Magnetoelastic stress measurements of 25 ML Fe grown on Au(001) at different deposition temperature. ME measurements are performed at 298 K.

of sputtering induced lattice modification on the magnetoelastic coupling is addressed [180–183].

In summary, MOKE and magnetoelastic coupling measurements of Fe film on Au(001) were presented in this section. I obtained the magnetoelastic coupling coefficient B_1 of Fe films grown at 298 K. The values are separated in two distinct regions. In region I, B_1 shows a dependence on film strain. This region is represented by Fe films with small strain below 0.3%. However, in region II, for films with larger strain, B_1 remains almost constant with B_1 -1.3 MJ/m^3. In the investigations of the effect of the growth temperature, B_1 remain unaltered with value of -1.3 MJ/m^3 for 25 ML Fe grown at 200, 298, and 375 K, indicating that the presence of an Au layer floating on top does not affect the magnetoelasticity of Fe/Au(001) system, a further discussion is presented in Section 8.3. An unexpected influence of sputter gas on magnetoelastic coupling was found. This novel finding is discussed in Section 8.4.
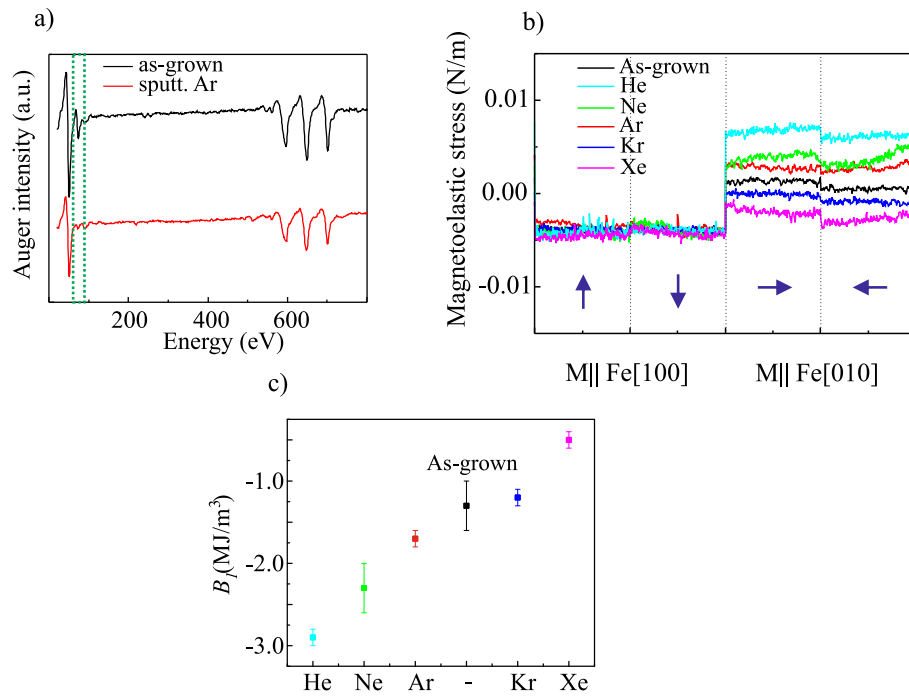
Figure 6.9: a) AES measurements of 25 ML Fe on Au before and after Ar-sputtering of 60 seconds to remove the Au layer floating on top. Auger spectra are vertically shifted for sake of visualization. b) Magnetoelastic stress measurement of 25 ML Fe on Au after removing the Au top layer with different noble gas ions. Curves are vertically translated for comparison. c) Magnetoelastic coefficient B_1 after the sputtering process with different gases.

Chapter 7

Film stress and magnetoelastic stress on Fe/Au/Fe trilayers on Au(001)

In this Chapter, I present results of film stress and magnetoelastic stress of epitaxial trilayer system of Fe/Au/Fe on Au(001). Section 7.1 describes the involved film stress on each preparation step of Fe/Au/Fe trilayers on Au(001). In Section 7.2, I present magnetic measurements, MOKE and magnetoelastic stress of these trilayers. This prototypical system offers an interesting playground, where quantum well states in Au modulate the relative magnetization direction of the two adjacent Fe layers, resulting in an oscillatory interlayer exchange coupling [7, 34, 46, 89, 97, 100, 104, 141, 184]. I find a variation of the magnetoelastic coupling coefficient B_1 with Au interlayer thickness, at constant total Fe film thickness. This result is seen as an experimental evidence that magnetoelasticity may be tuned by QWS, an effect that has not been discussed before.

7.1 Stress and structure

Each individual step of the Fe/Au/Fe trilayer preparation follows the description given in Section 3.4. Trilayers are prepared by subsequent depositions of Fe and Au atomic layers on Au(001). I focus on 10 ML Fe on Au(001), which are covered by X ML Au, where X= $1, 2, ..., 12$ ML, and topped by 15 ML of Fe. All depositions are done at 298 K.

Figure 7.1a shows stress measurements during Fe deposition in the trilayer Fe/Au/Fe on Au(001). The red curve shows the stress change during deposition of 10 ML Fe on Au(001). The green solid line represents the
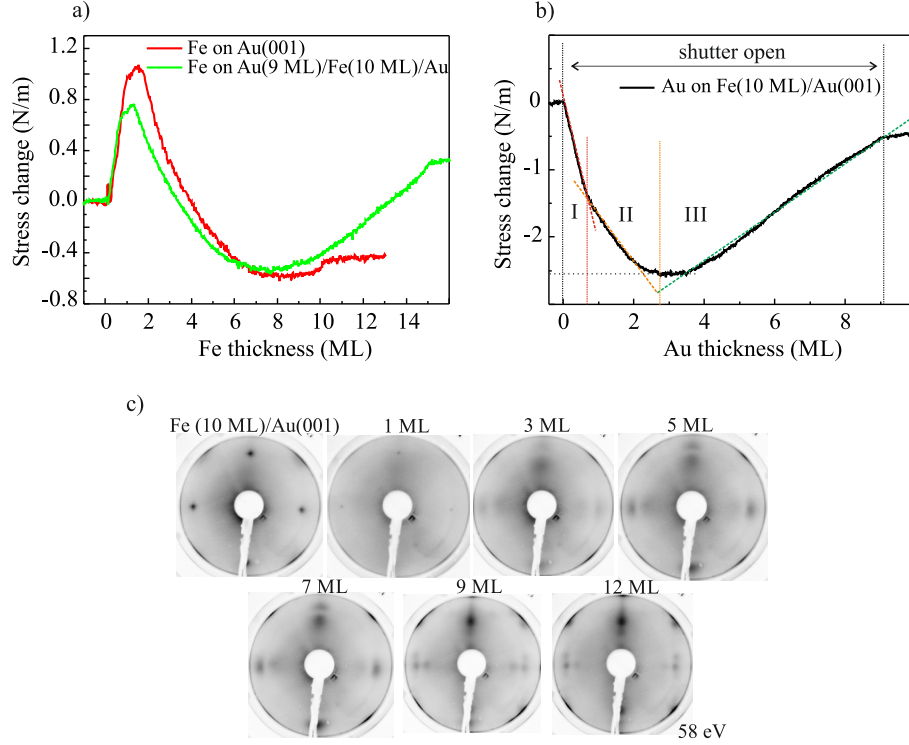
Figure 7.1: a) Stress measurement during deposition of 10 ML Fe on Au(001) in red, and 15 ML Fe on Au(9 ML)/ Fe(10 ML)/ Au(001) in green. b) Stress measurement during deposition of Au on Fe(10 ML)/Au(001). 1 ML: 12.02×10^{14} cm^{-2}; $t_{Ag} = 2.04$ Å. The vertical dashed lines indicate the beginning and end of Au deposition. The colored dashed lines represent the change of slope in regions I, II, and III. c) LEED diffraction pattern at 58 eV after Au deposition, for different Au thickness. The LEED image is inverted, dark means high and white means low intensity.

stress change due to 15 ML Fe deposited on top of Au(9 ML) /Fe(10 ML) /Au(001). The Fe-induced stress in both depositions resembles the behavior presented in Section 6.1, which are described therein. A relevant observation is the similarity between the stress curves indicating an analogous interface Fe/Au(001) and Fe/Au/Fe/Au(001). A small deviation in magnitude of the stress maximum at 1-2 ML of 0.3 N/m is observed. We attributed this to the subtle difference of the surface of Au film and of the clean Au(001). Next, the stress behavior during the deposition of Au on Fe/Au(001) is presented and the Au surface is characterized.

It is important to note that Au is grown on an Fe film which is epitaxially strained on Au(001). Thus, we expect no misfit strain and consequently no

misfit stress in the Au film.

Figure 7.1b shows a typical stress measurement as a function of Au film thickness (1 ML Au: 2.04 Å). The stress curve is divided in three parts showing a compressive stress in regions I and II and an inversion of sign to a tensile stress in region III. The stress change reaches a maximum magnitude of −2.5 N/m for the minimum of the curve, between region II and III. This value is large for the expectation that the Au film should show no misfit stress. The dashed colored lines indicates the change of curve slope. A compressive stress −10.8 GPa is observed immediately after the opening of the evaporator shutter, indicated in region I. This considerable stress persists up to 0.5 ML. The slope is reduced to a stress of −4.0 GPa for larger thickness in region II. This stress reaches a minimum of −2.5 N/m after 3 ML Au deposition. With increasing Au deposition the slope of stress inverts its sign. A positive slope corresponding to a tensile stress of +1.8 GPa is measured in region III. This stress is observed until the end of the deposition.

Figure 7.1c displays LEED diffraction pattern at different Au thickness. The first image depicts the diffraction pattern before Au deposition. The image shows a (1×1) pattern from the epitaxially strained Fe film. After 1 ML Au deposited the LEED shows a similar (1×1) pattern, with reduced intensity. As the Au thickness is increased the pattern changes. At 3 ML Au the LEED shows faint features of the Au(001) (1×5) reconstruction. Thus, the surface reconstruction is reestablished. For thicker Au film the spots become intense and sharp, however, with reduced quality as compared with Au(001). A difference between the Au film and the Au(001) substrate is the preparation temperature. The crystal has been annealed at 580 K for 20 min. to improve the surface order. This contrasts with the Au film, which is kept at 298 K to avoid undue intermixing of Fe-Au.

We discuss the stress results in view of the formation of the surface reconstruction and homo-epitaxial growth in Section 8.2.

Figure 7.2a shows Auger spectra after each preparation step of the Fe (15 ML) / Au (9 ML) / Fe (10 ML) trilayer on Au(001). In each Auger curve the Au/Fe ratio is indicated, when applicable. The first deposition of 10 ML Fe film shows a ratio consistent with that presented in Section 6.1, Au/Fe=0.8. After the deposition of 9 ML of Au (green curve) the ratio increases to 10.8. With the top Fe film of 15 ML thickness the Au/Fe ratio decrease to 0.5. We observe that this ratio remains constant as a function of Au thickness ($t_{Au} = 1...12$ ML).

Figure 7.2b shows LEED images after each preparation step of Fe(15 ML) / Au(9 ML) / Fe(10 ML) on Au(001). A characteristic (1×5) pattern of Au reconstruction surface is visible for clean Au(001). After deposition of each Fe film a (1×1) pattern is observed. The diffraction pattern of 9 ML of Au
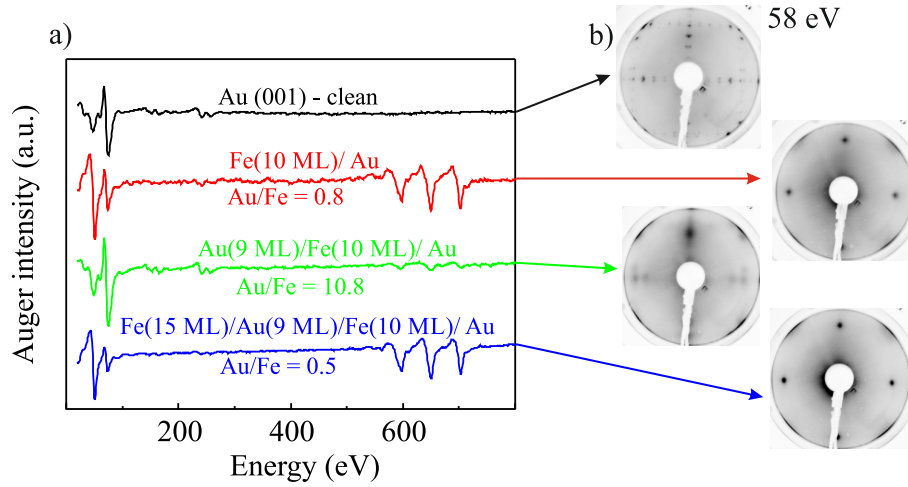
Figure 7.2: a) Auger spectra after each stage of the sample preparation of the trilayer Fe/Au/Fe on Au(001). The respective Au/Fe ratio of the AES peaks (Au-69 eV and Fe-651 eV) is shown. b) LEED patterns at 58 eV of each stage of the sample preparation as indicated by arrows.The LEED image is inverted, dark means high and white means low intensity and Auger spectra are vertically shifted for sake of visualization.

film reveals indications of a blurred (1×5) surface reconstruction. Although the diffraction spots are very broad, characteristic features of the surface reconstruction are present, as mentioned in Fig. 7.1c.

In summary, I presented stress measurements during the formation of a trilayer film of Fe/Au/Fe on Au(001). Our results offer a new level of understanding of the interfaces of the system. Our results reveal the formation of a reconstructed surface, which is observed in LEED images in a 3 ML Au film grown on Fe/Au(100). Measurements of stress due to surface reconstruction are very demanding [185] and hard to be predicted [50]. Further discussions concerning stress changes during surface reconstruction and its implication are presented in Section 8.2.3.

7.2   Magnetic properties

In this Section, I present the results of MOKE and magnetoelastic stress measurements of the Fe(15 ML)/ Au(X ML)/ (10 ML) Fe trilayer on Au(001) for different thickness of Au. The MOKE results present the expected alternation of parallel and antiparallel magnetization alignment of Fe layers with increasing Au thickness [186]. This behavior is characteristic of an os-
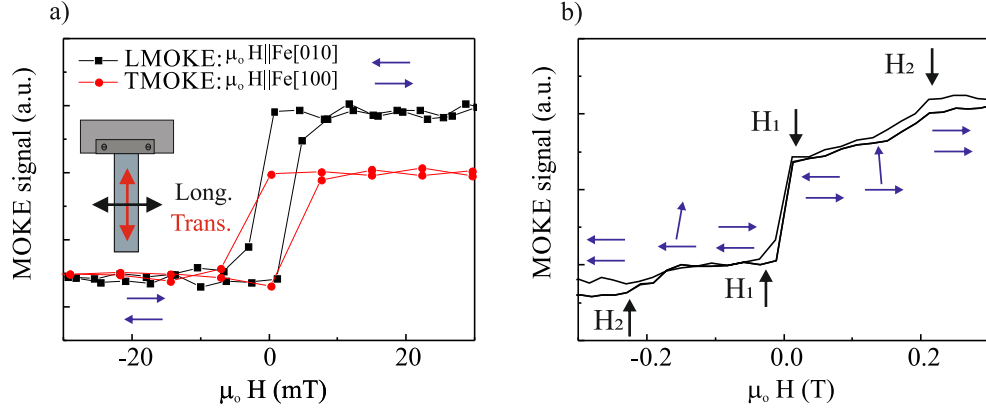
Figure 7.3: a) Longitudinal and transversal MOKE of Fe(15 ML) / Au(9 ML) / Fe(10 ML) on Au(001). b) Longitudinal MOKE with high magnetic field with two switching fields indicated. The sketches indicate the magnetization state of the Fe layers.

cillatory interlayer exchange coupling observed for this system [97, 104–106]. The magnetoelastic coupling of these trilayers show a clear oscillatory-like behavior with increasing Au thickness. An investigation of the magnetic anisotropy of the system is performed.

Figure 7.3a shows MOKE results of the Fe(15 ML)/ Au(9 ML)/ Fe(10 ML) trilayer on Au(001) in the longitudinal and transversal MOKE geometry. The longitudinal (black) and transversal (red) MOKE reveals a square-like hysteresis loop. The magnetic saturation fields in both directions are below 10 mT. The easy magnetization of the samples lies in-plane along Fe[100] [186]. The MOKE measurements are taken before the magnetoelastic stress measurements to establish the necessary saturation field to obtain a collinear magnetization alignment of the Fe layers.

This system, Fe/Au/Fe, is well know to have an oscillatory interlayer exchange coupling (IEC), where the magnetization alignment of the Fe layers changes from parallel (P) to antiparallel (AP) with increasing Au thickness [97, 104–106]. The oscillations of the IEC is mediated via spin-polarized confinement effect in the Au spacer layer [89]. The distinct alignments of the Fe magnetization results in different MOKE responses [186]. In order to check this characteristic in my samples I performed MOKE measurements with the highest possible magnetic field. In the longitudinal magnetization direction it is possible to achieve fields up to 0.3 T, along the transversal direction 0.1 T are possible.

Figure 7.3b shows a LMOKE measurement of a Fe(15 ML)/ Au(9 ML)/
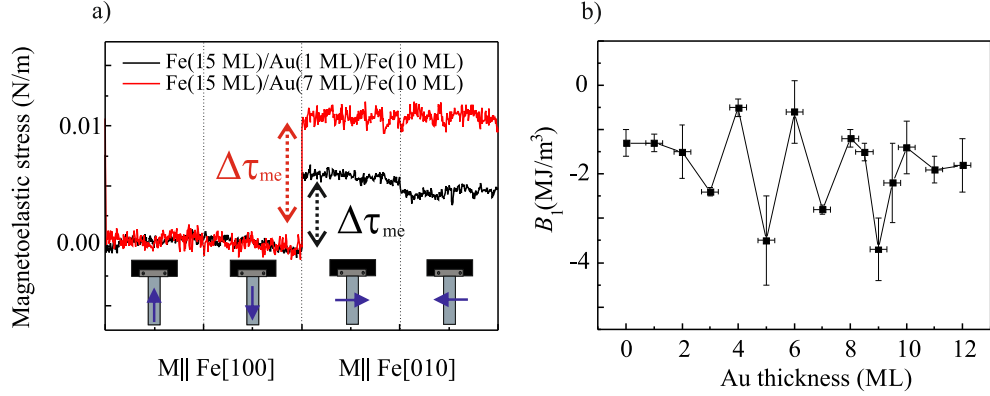
Figure 7.4: a) Magnetoelastic stress curves of Fe(15 ML) / Au(1 ML) / Fe(10 ML) and Fe(15 ML) / Au(7 ML) /Fe(10 ML) on Au(001). The arrows indicate the direction of the applied field of magnitude 20 mT. b) Compilation of B_1 obtained for different Au spacer layer thickness.

Fe(10 ML) trilayer. The trilayer with 9 ML thick Au is expected to have the magnetizations of the Fe layers above and below the Au spacer aligned in an antiparallel configuration [97, 104–106]. The hysteresis loop observed in Fig. 7.3b, reveals indeed a distinct curve as compared with the single square-like hysteresis loop of a parallel magnetization alignment. We identify two switching events. The field H_1 shows the switching field for a collinear alignment of the Fe layers, which remain in an antiparallel magnetization (AP state). The field H_2 field is near 200 mT, and characterizes the switching of the magnetization to a parallel alignment of both Fe layers and the external field, resulting in a P state. The intermediate field is the region between the H_1 and H_2, where the transition from antiparallel to parallel magnetization occurs. These results are in agreement with previous reports on similar Fe layer thickness [186].

The results indicate that in a magnetoelastic stress measurement, where both directions (longitudinal and transversal) of the magnetic field are applied, the field suffices to surpass the H_1 saturation field. This means, for a AP magnetic configurations the Fe films may saturate to a collinear AP magnetization state when the fields are close to 10 mT. This collinear alignment is indicated in Fig. 7.3a by the blue arrows. Therefore, all ME measurements are performed at 20 mT applied field. From the symmetry of the ME effect the same ME stress is expected for AP and P states.

Figure 7.4a presents magnetoelastic stress measurements of a Fe(15 ML)/ Au(X ML)/ Fe(10 ML) trilayer on Au(001) with two different Au thickness

X. The black and red curves are measurements with X= 1 and 7 ML, respectively. The blue arrows show the directions of the applied magnetic field. The red and black arrows identify the difference in magnetoelastic stress $\Delta\tau_{me}$ of 0.010 and 0.005 N/m, respectively. Although the total Fe thickness is constant in both samples, $t_{\text{Fe}} = 25$ ML, the curves clearly give distinct B_1 values. Thus, a substantial change in the magnetoelastic coupling caused by the variation of the thickness of the Au layer is observed. Next, I present a collection of results of magnetoelastic coupling by varying only the Au thickness in a single ML fashion.

Figure 7.4b shows the magnetoelastic coupling B_1 of the Fe/Au/Fe trilayer on Au(001) as a function of Au thickness. A non-monotonic change of B_1 with increasing Au thickness is observed. Above 2 ML of Au, B_1 changes its magnitude for each monolayer added, and an oscillatory curve results. Strikingly, the variation of B_1 amounts to 3 MJ/m^3. Thus, a significant variation of the magnetoelastic coupling of the Fe/Au/Fe system is observed upon variation of the Au thickness. Since the origin of magnetoelasitcity is the strain dependence of the magnetic anisotropy, I investigate whether the latter is also influenced by changing the Au interlayer thickness.

A quantitative analysis of the in-plane magnetic anisotropy of a film is obtained by applying a constant magnetic field perpendicular to the direction of the sweeping field in MOKE [140–142], as described in Section 3.3. The in-plane magnetic anisotropy energy density of the Fe film in a flat Au(001) is described by $K/4\sin^2(2\phi)$, where K is the cubic anisotropy constant and ϕ is the angle between magnetization and the crystalline axis <100> [143]. K is a positive value for an easy magnetization axis along <100> [176, 187]. The extra field $\mathbf{H}_{\text{bias}}$ along the vertical in-plane direction provides an uniaxial magnetic anisotropy with magnetization along the constant applied field in zero sweeping field $\mathbf{H}$ along the horizontal direction. The field energy term is the contribution of both applied fields as $-\mu_o(\mathbf{H} + \mathbf{H}_{\text{bias}}) \cdot \mathbf{M}$, where $\mathbf{M}$ is the saturation magnetization of bulk Fe. The bias field is the additional constant field applied in the vertical direction, along [100]. The loop is taken with the sweep field applied along the [010] direction. Minimizing the energy with respect to ϕ and considering $K_{\text{u}} \ll K_1$ one finds the cubic anisotropy given by the initial slope s of the loop as [141, 143]:

$$K = \frac{1}{2}\frac{\mu_o M_{\text{s}}^2}{s}.$$ (7.1)

The bias field forces the magnetization into the easy direction [100] as soon as the sweeping field is reduced to zero. With increasing sweeping field the magnetization rotates towards the horizontal direction [010], and the longitudinal Kerr signal changes. In this rotational region of magnetization

73

the slope (s) of the longitudinal Kerr signal vs. field is proportional to the magnetic anisotropy K, see Fig. 7.5a. This technique was applied for Fe(15 ML)/ Au(X ML)/ Fe(10 ML) trilayers with X varied from 0 to 12 ML Au.

Figure 7.5a shows a LMOKE measurement of the trilayer Fe(15 ML) / Au(3 ML) / Fe(10 ML) grown on Au(001). For this measurements a strong vertical field of 35 mT was applied in order to obtain reliable values of the slope in the entire thickness range investigated. The hysteresis loop is split and the central region gives the slope s, as described in Section 3.3. The inset shows the magnetization directions of the sample under different fields. From Eq. 7.1 and the value of $\frac{1}{2}\mu_0 M_s^2$ of 1.85 MJ/m^3 from bulk Fe [139], the magnetic anisotropy K of these trilayers is obtained. Figure 7.5b shows the magnetic anisotropy K as a function of Au thickness in blue. K is the fourfold magnetic anisotropy constant, and no sign of an uniaxial anisotropy is found for these samples in the absence of the transversal field $\mathbf{H}_{\text{bias}}$.

In Section 3.3 the procedure of the experiment by applying strong bias field was discussed. The values of K obtained here could be influenced by interface effects or additional contributions from the bias field itself. The increase of the fourfold anisotropy of Fe thin films was observed in Ref. [188]. These authors investigated Fe films on GaAs(001) with and without a MgO underlayer. The authors found a cubic anisotropy of 67 kJ/m^3 in a film of 50 ML of Fe with MgO underlayer [188]. This value is larger than the Fe bulk value of 48 kJ/m^3 [144], and it is similar to the value observed for 25 ML Fe on Au(001), presented in Section 3.3. Even for a film thickness of the order of 50 ML Fe the interface affects the cubic anisotropy. In [176] the authors investigated the in-plane anisotropy of Fe films on Au and Ag. They found an increase of the interface term K_1^S of the cubic anisotropy for Fe films on Au as compared with Fe on Ag. They attributed this increase to the enhancement of the orbital moments at the interface Fe/Au. This indicates that interface modification can affect the cubic anisotropy of the Fe films. In the trilayer system, investigated in this work, K is $\approx 2\times$ larger than for a single Fe(25 ML) film with 67 kJ/m^3, see in Section 3.3. Further investigations may be needed to guarantee the definitive reason for this huge increase in the anisotropy. However, a qualitative analysis of the K results could be done as the bias field is kept fixed.

K shows an oscillatory variation with increasing Au thickness. This oscillations can be compared with the variation of B_1. For this Fig. 7.5b also shows the magnitude of magnetoelastic coefficient B_1, extracted from Fig. 7.4. The variation of K is in in-phase with the variation of the magnitude of B_1. The data are plotted along side the magnetic anisotropy in order to stretch the relation between both constants. We find that B_1 has
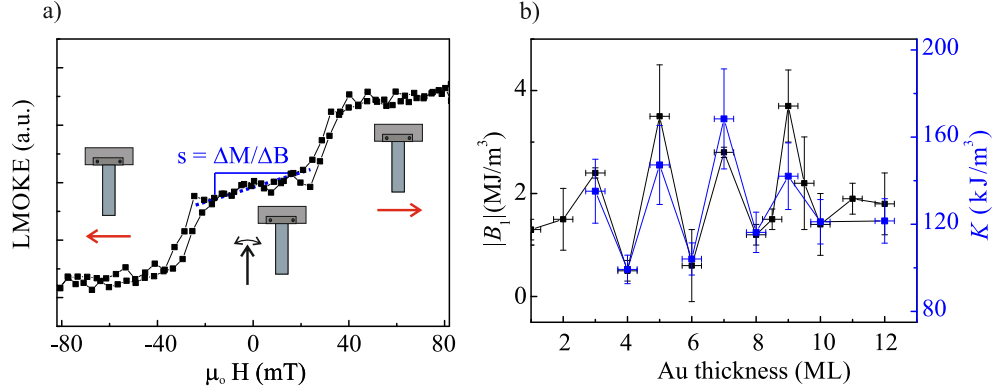
Figure 7.5: a) Longitudinal MOKE with additional bias magnetic field of $\mu_0\mathbf{H}_{\text{bias}} = 35$ mT along the transversal direction of Fe(15 ML)/ Au(3 ML)/ Fe(10 ML) on Au(001). The sketches show the in-plane magnetization direction of the sample. The slope is inversely proportional to the magnetic anisotropy. b) The magnetic anisotropy K as a function of Au spacer layer thickness is shown in blue, and the module of B_1 is plotted for sake comparison.

the lowest magnitude where K is also low. This is evident for $t_{\text{Au}} = 4$, 6, 8 ML. This finding indicates the intimate correlation between magnetic anisotropy and magnetoelasticity.

In summary, I showed that the magnetoelastic coupling B_1 of Fe/Au/Fe trilayers exhibits an oscillatory variation with increasing Au thickness. This hints towards a strong impact of QWS on the magnetoelaticity of this system. Despite the large number of publications discussing oscillatory interlayer exchange coupling, to the best of our knowledge, the corresponding effect on B_1 has not been described before. This novel finding is further discussed in view of the physics underlying this phenomenon in Section 8.3.

Chapter 8

Discussion

This Chapter presents discussions of the results shown in this thesis. The discussions are organized in three main topics. In the first Section 8.1, I focus on the structural change due to different deposition temperature of Fe on $Bi_2Se_3(0001)$. Section 8.2 details the relation between film stress, strain and structure of metallic films. The discussion is presented in view of segregation, interdiffusion and reconstruction of Fe and Au films on Ag(001) and Au(001). The magnetic properties are discussed in Sections 8.3, 8.4, and 8.5 focusing on the results of magnetoelaticity (ME). The interface-driven modifications of ME is discussed in Section 8.3, and the influence of ion implantation on ME is discussed in Section 8.4. The impact of electronic confinement on magnetoelasticity is discussed in the last Section 8.5.

8.1 Fe on Bi_2Se_3: Film stress and structural domains

Here, I discuss the stress results of Fe deposited on $Bi_2Se_3(0001)$ at different temperature, presented in Section 4. The compressive stress change, see in Fig. 4.1, after deposition of 0.3 ML Fe increases with increasing deposition temperature from 150 K (-0.5 N/m) to 473 K (-3.5 N/m). The increase of total stress $\Delta\tau$ with increasing deposition temperature is described to a change film structure and morphology. This is corroborated by LEED and AES measurements after Fe deposition. As pointed out in Fig. 4.2, at elevated deposition temperature a reduction of the Bi/Fe ratio in AES is found and a distinct diffraction pattern is observed in LEED.

Recently, the authors of Ref. [189] investigated the structure of submonolayer Fe (0.3 ML) on $Bi_2Se_3(0001)$, deposited at 160 K by X-ray absorption fine structure. They explored the X-ray absorption spectra to exploit the

possible localization of Fe atoms by calculating the polarization dependence of the interference function. They found that the only adsorption site which fits all observations is the bismuth substitutional site. They conclude that for deposition at 160 K Fe atoms substitute Bi atoms, predominantly in the top QL. The Fe-Se distance as-deposited varies between 2.39 and 2.57 Å. This huge variation of the Fe-Se atomic distances was attributed to the inequivalence of the nearest neighbor Se around Bi in a QL. After several minutes of annealing up to 520 K, the FeSe interaction forms an local ordered FeSe phase at a distance close to 6 Å.

An ordered FeSe phase on Bi$_2$Se$_3$(0001) induced by increasing the Fe deposition or the annealing temperature was also observed by our work [63]. The combined SXRD, LEED and STM measurements provide insight into the peculiar structure of the formed FeSe after annealing at 623 K for 10 min. The analysis of the results of our work [63] shows details of the formation of strained FeSe nanocrystals embedded in the surface. Remarkably, FeSe forms for deposition of Fe only. The formation process is, therefore, different from the progressive build-up of FeSe triple layer by co-depositing Fe and Se [190, 191].

The structure of the thermally induced FeSe nanocrystals on Bi$_2$Se$_3$(0001) shows a similar tetragonal structure as compared to bulk α-FeSe.

α-FeSe consists of triple layers (TL) bonded by van-der-Waals forces. Figure 8.1 shows a hard sphere model of the α-FeSe structure. Figure 8.1a presents the in-plane structure of the bulk in a top view and Fig. 8.1b shows the stacked TL in the z-direction. Each TL is formed by a stack Se-Fe-Se, arranged as a rectangular prism. The lattice constant of bulk FeSe in the z-direction is defined from Se to the next Se, and it amounts to 5.52 Å [192], as indicated in Fig. 8.1b. The structure at 300 K is tetragonal with in-plane lattice dimensions of $a = b = 3.77$ Å [193].

The α-FeSe-like phase observed on Bi$_2$Se$_3$(0001) shows a strained structure. The in-plane atomic distances were obtained by STM and LEED analyses, and the z-direction spacing was investigated by SXRD measurements [63]. The results show a lattice expansion along the vertical direction of 0.2 Å, with an average FeSe thickness of three TL ($t_{\text{FeSe}} \approx 15$ Å). The in-plane lattice constants also showed a strained state, where a and b differ by 2%.

An estimate of the maximum thickness of FeSe nanocrystals prepared by this procedure (Fe deposition on Bi$_2$Se$_3$ plus annealing) is given by the maximum depth from which Se atoms can be extracted from the bulk of Bi$_2$Se$_3$ to form FeSe. The fate of the Bi atoms remains unclear at this point. A specific investigation of this issue is needed, however, but we may speculate about three possibilities. 1) The Bi atoms could desorb from the surface dur-
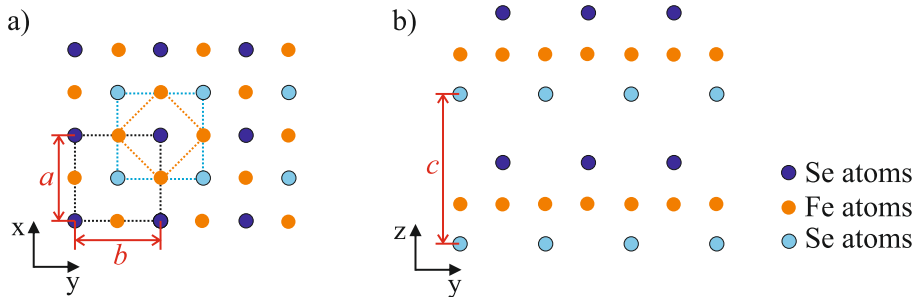
Figure 8.1: Hard sphere model of an α-FeSe triple layer (TL). Individual Se-Fe-Se layers are stacked along the z-direction and are bonded by van-der-Waals forces between Se layers. The FeSe bulk crystal has a tetragonal structure with a = b = 3.77 Å, and c = 5.52 Å. [192, 193]

ing annealing. 2) Bi atoms could remain on the surface as a contamination. The high surface mobility of the usual contamination on the Bi$_2$Se$_3$ surface speaks in favor of this. Or 3) Bi atoms migrate into the bulk of the crystal and form bulk defects.

The stress results during Fe deposited at 150 K on Bi$_2$Se$_3$(0001) shown in Fig. 4.1, reveal a small change of stress of -0.5 N/m. This small compressive stress could be related to the replacement of Bi by Fe. This replacement gives rise to a relaxation of the structure as indicated by Ref. [189]. Thus, the absence of a LEED diffraction pattern, Fig. 4.2b, could be related to the substantial atomic dispersion, with randomly varying atomic distances of Bi-Se to Fe-Se in a QL.

With increasing of deposition temperature a sizable compressive stress is measured, and a change of the LEED diffraction pattern is observed. Deposition at 298 K shows compressive stress of -2.3 N/m and a weak LEED diffraction. A pronounced compressive stress of -3.5 N/m and a clear LEED pattern, indicative of pronounced long range structural order, is observed for depositions at 473 K.

The LEED diffraction pattern observed in a sample prepared at 473 K shows diffraction due to different domains, see Fig. 4.2b. This is discussed in our analysis in Ref. [63]. The diffraction pattern is described to a combination of coexisting structures of Bi$_2$Se$_3$(0001) and FeSe. At elevated temperature the formation of FeSe nanocrystal is promoted. FeSe grows in a three rotational domains, as indicated in Fig. 4.2b by three sets of arrows with different color code. In my measurements the coexistence of three rotational domains on Bi$_2$Se$_3$ is also observed. Intense diffraction spots appear due to a overlap of two diffraction points, from the Bi$_2$Se$_3$ surface and the FeSe nanocrys-

tals. These intense spots are marked by red circles in Fig. 4.2b. We ascribe the low intensity of these diffraction spots to the lower Fe coverage used here, 0.3 ML Fe, as compared to 0.7 ML in Ref. [63], and the difference of annealing/growth temperature may contribute further.

We attribute the increase of compressive stress, observed in Fig. 4.1, to the formation of α-FeSe-like nanocrystals. For a quantitative analysis of the stress at 473 K we recall the structural analysis by LEED and STM from Ref. [63].

The lattice constants and the symmetry of bulk FeSe and Bi$_2$Se$_3$ are distinctly different. Bi$_2$Se$_3$ has an hexagonal surface unit cell with base vectors of $a = 4.14$ Å. FeSe has a square unit cell with $a = 3.77$ Å [193]. The different atomic spacing of Bi$_2$Se$_3$ and FeSe result in a Moiré pattern by superimposing the respective unit cells with specific orientations. The presence of a Moiré pattern infers non-pseudomorphic growth. The formation of FeSe on Bi$_2$Se$_3$ gives rise to strained FeSe, where the in-plane lattice constants a and b differ by 2%. The LEED analysis [63] gives a rectangular surface unit cell with $a = 3.77$ Å and $b = 3.85$ Å. The expected stress for the formation of orthorhombic FeSe nanocrystals can be estimated from the resulting strain state of the FeSe nanocrystals.

The in-plane strain $(\varepsilon_1 \neq \varepsilon_2)$ of FeSe on Bi$_2$Se$_3$(0001) is calculated with respect to the lattice constant of bulk FeSe as

$$\varepsilon_1 = \frac{(a_{\text{FeSe}}^{\text{film}} - a_{\text{FeSe}}^{\text{bulk}})}{a_{\text{FeSe}}^{\text{bulk}}} = 0 \tag{8.1}$$

and

$$\varepsilon_2 = \frac{(b_{\text{FeSe}}^{\text{film}} - a_{\text{FeSe}}^{\text{bulk}})}{a_{\text{FeSe}}^{\text{bulk}}} = +0.021. \tag{8.2}$$

Thus, the misfit is anisotropic. FeSe formed on Bi$_2$Se$_3$(0001) shows a three rotational domains. They are rotated by 120° from each other. Figure 8.2 shows a sketch of the directions of the domains with respect to the crystallographic orientation of the Bi$_2$Se$_3$ crystal.

Because the three directions are crystallographic equivalent, the strain for distinct domains can be calculated with Eq. 8.1 and Eq. 8.2. We assign domain 1 with the directions 1 and 2 of the strain aligned parallel to the in-plane $[01\bar{1}0]$ and $[2\bar{1}\bar{1}0]$ directions of Bi$_2$Se$_3$(0001), respectively. The stress for each direction is calculated as [51]:

$$\tau_1 = \left. \frac{Y}{1 - \nu^2} \right|_{\text{FeSe}} (\varepsilon_1 + \nu\varepsilon_2) \tag{8.3}$$

and

$$\tau_2 = \left. \frac{Y}{1 - \nu^2} \right|_{\text{FeSe}} (\varepsilon_2 + \nu\varepsilon_1), \tag{8.4}$$
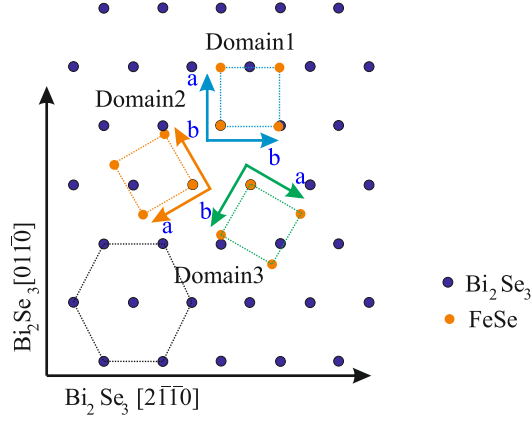
Figure 8.2: Sketch of the Bi$_2$Se$_3$(0001) substrate and the respective orientation of FeSe domains rotated by 120°. The dashed structure represent Bi$_2$Se$_3$ surface. The solid rectangles indicate a unit cell of FeSe. The Moiré pattern appears along the b directions, and along direction a negligible strain results.

where Y and ν are the Young's modulus and the Poisson ratio of FeSe(001), respectively. For FeSe bulk we have $Y = 73.0$ GPa and $\nu = 0.179$ [194]. Inserting the values for the domain 1, the calculated stress in each direction is tensile with $\tau_1 = +0.286$ GPa and $\tau_2 = +1.6$ GPa.

The presence of three rotated domains requires averaging of their respective stress contributions for the three domains. The transformation matrix a_{ij} is used in order to obtain the stress along the length and the width of the crystal. The stress tensor τ_{ij} is written as:

$$\tau_{ij} = \begin{pmatrix} \tau_1 & 0 & 0 \\ 0 & \tau_2 & 0 \\ 0 & 0 & 0 \end{pmatrix}.$$

To obtain the stress contribution from the rotated domains, a tensor transformation needs to be applied, following Ref. [51]:

$$\tau'_{ij} = a^T_{ij} \tau_{ij} a_{ij}, \tag{8.5}$$

where τ'_{ij} is the stress tensor of the rotated domain, a_{ij} and a^T_{ij} are the transformation matrix and its transposed, respectively. The transformation matrix is written:

$$a_{ij} = \begin{pmatrix} \cos\theta & -\sin\theta & 0 \\ \sin\theta & \cos\theta & 0 \\ 0 & 0 & 1 \end{pmatrix},$$

where θ is the angle between the domains (d1, d2, d3): $\theta = 120°$ for domain 2, and $\theta = 240°$ for domain 3. We obtain:

$$\tau^{d1} = \begin{pmatrix} +0.286 & 0 & 0 \\ 0 & +1.6 & 0 \\ 0 & 0 & 0 \end{pmatrix} \text{ GPa,}$$

$$\tau^{d2} = \begin{pmatrix} +1.272 & -0.5688 & 0 \\ -0.5688 & +0.6149 & 0 \\ 0 & 0 & 0 \end{pmatrix} \text{ GPa,}$$

$$\tau^{d3} = \begin{pmatrix} +1.272 & +0.5688 & 0 \\ +0.5688 & +0.6149 & 0 \\ 0 & 0 & 0 \end{pmatrix} \text{ GPa.}$$

The total averaged stress of all three domains (τ_{ij}^{total}) is given by:

$$\tau_{ij}^{\text{total}} = \frac{\tau_{ij}^{d1} + \tau_{ij}^{d2} + \tau_{ij}^{d3}}{3}, \tag{8.6}$$

where the superscripts d1, d2, and d3 identify the first, second, and third domain, respectively. The resulting stress is isotropic in-plane

$$\tau_{12}^{total} = \begin{pmatrix} +0.943 & 0 & 0 \\ 0 & +0.943 & 0 \\ 0 & 0 & 0 \end{pmatrix} \text{ GPa.}$$

We conclude that the strained FeSe on Bi$_2$Se$_3$ gives rise to three stress domains which lead to an average calculated isotropic in-plane tensile stress of $+0.943$ GPa.

The result of compressive stress, shown in Fig. 4.1, is in contrast to the calculated tensile stress. In order to make a proper comparison the stress observed during deposition of Fe on Bi$_2$Se$_3$ we take into account the limitations of the process to form FeSe. The amount of iron deposited and the arrangement in three TL of nanocrystals on the substrate is considered. Based on the areal atomic density of Fe calibrated by the quartz crystal monitor we have 1 ML: 12.17×10^{14} cm^{-2}. However, the nanocrystals are distributed in three TL described in Ref. [63], with an average thickness of 15 Å. Therefore, the deposited amount of Fe of 0.3 ML resulting in $(0.3/3) \cdot 15$ Å FeSe. We can consider the quantity of FeSe formed with Fe deposition as effective thickness t_{eff}, and the stress is calculated with

$$\tau_{\text{FeSe}} = \frac{\sigma}{t_{\text{eff}}}, \tag{8.7}$$

where σ is the measured stress change, and $t_{\text{eff}} = 0.1 \cdot 15$ Å. The film stress measured during Fe deposition at 473 K is -3.5 N/m, extracted from Fig. 4.1. This gives rise to an experimental compressive film stress of -23 GPa.

The experimental film stress has an opposite sign and it is roughly a factor of twenty larger than the calculated stress for strained $FeSe/Bi_2Se_3$. Obviously, the stress calculation, which consider epitaxial misfit only, misses important contributions to the experimental film stress.

The huge compressive stress can be the result of atomic-scale intermixing and atomic dislocations during Fe deposition and FeSe formation. Deposition at 298 K also shows a significant compressive stress of -14 GPa, where the same surface order is deduced from LEED measurements. As described in Ref. [189], for 0.3 ML of Fe deposited at 160 K on Bi_2Se_3 the Fe atoms already replace Bi atoms in a substantial relaxed structure. Only after annealing at higher temperature an ordered α-FeSe-like structure is formed.

In summary, the experimental results on film stress of Fe on Bi_2Se_3 indicate compressive stress in contrast to the epitaxial stress calculated for epitaxial strained orthorhombic FeSe. This indicates that epitaxial strain is not the dominant source of film stress. The replacement of Bi with Fe induces a substantial structural disorder. This displacement has been reported in Ref. [189] for a low temperature of Fe deposition. The annealing procedure induces nanoislands of α-FeSe-like as pointed out in our work [63]. These nanoislands are distributed in three rotational domains in accordance with the symmetry of the hexagonal structure of the $Bi_2Se_3(0001)$ substrate. The complexity of the FeSe formation process is apparent in view of stress analyses as a function of temperature. Further investigations are needed to clarify the origin of the compressive stress, and identified where the Bi atoms go. Next, I discuss growth, stress, and magnetic properties of Fe films on noble metal substrates.

8.2 Relation of stress, strain and structure of Fe films

The strain of a film grown epitaxially on a metallic surface has a prevailing contribution to the epitaxial misfit stress. The epitaxial stress originates from the misfit of the lattices constant of the involved materials. The misfit is calculated as described in Eq. 2.3 for an isotropic in-plane strain. The growth of bcc Fe on Ag(001) or Au(001) is described by an Fe unit cell which is rotated by 45° with respect to the substrate surface unit cell [55].

This rotation results in a minimal mismatch of less than 1% of the unit
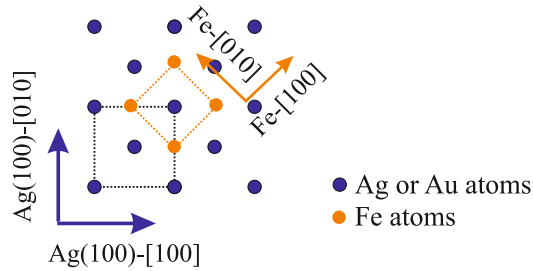
Figure 8.3: Hard spheres model of the in-plane arrangement of the Fe bcc unit cell on the Au fcc unit cell in epitaxial growth.

cells. This small strain does not impede epitaxial growth, and film growth with epitaxial misfit strain is expected. Figure 8.3 shows a sketch of the epitaxial relation.

This 45° rotation of the Fe unit cell gives rise to a small misfit of +0.8 % and +0.6 % on Ag(100) and Au(100), respectively. This misfit between film and substrate induces tensile film stress. The misfit stress is calculated with Eq. 2.4 from Fe bulk elasticity. The biaxial modulus $Y/(1-\nu)$ values used in this thesis are presented in Table 3.1, Chapter 3. The misfit of +0.8 % of Fe on Ag(001) gives rise to a calculated tensile stress of +1.7 GPa. Likewise, +0.6 % misfit of Fe on Au(001) yields a tensile stress of +1.4 GPa. Thus, epitaxial growth in a layer-by-layer mode should lead to a constant tensile film stress of the calculated magnitude.

Surprisingly, the experimental film stress shows a distinctly different behavior, shown in Sections 5.1 and 6.1. For both substrates I identify a stress region labeled II in Fig. 5.1 and 6.1 where a non-monotonic stress is measured. The negative slope indicates compressive stress, in contrast to the calculated tensile stress. The compressive region lasts up to a critical thickness. The critical thickness is different for Au and Ag(001). Thus, the analysis of Fe growth on each substrate, Ag(001) and Au(001), is discussed separately. In the first Subsection 8.2.1, I focus on the relation of films stress and the growth mode of Fe on Ag(001). In the next Subsection 8.2.2 I perform the analysis of Fe on Au(001). We shall see that surface reconstruction and interdiffusion are important aspect to understand the stress behavior. Thus, Subsection 8.2.3 discusses the relation of stress due to surface reconstruction and self-diffusion during deposition of Au films on a strained Fe film on Au(001).

84

Table 8.1: Calculated surface stress τ, surface free energy γ of Fe and Ag, the methods of calculation are indicated: FP-LAPW full potential linear combination of augmented waves, FS: empirical n-body Finnis-Sinclair potencial, EAM: embedded atom method, EMTO: exact muffin-tin orbitals, FPLO: full-potential local-orbital , PAW: projector-augmented-wave, KKR-ASA: Korringa–Kohn–Rostoker-atomic sphere approximation. Compilation from [49].

Material	Surface stress $\tau_{[001]}$ (N/m)	Surface free energy γ (J/m^2)	Method	Reference
Ag(001)		1.59	KKR-ASA	[199]
	0.82	0.70	EAM	[195]
	1.6, 1.1*	0.76, 0.75*	FS	[196]
		1.2		[200]
		1.09		[201]
		1.3		[202]
Fe(001)	0.5	2.45	EMTO	[203]
	1.39*	2.55, 2.50*	PAW	[198]
		3.50	KKR-ASA	[199]
	0.57	2.62	EMTO	[197]
	1.15	3.09, 3.07*	FPLO	[197]
		2.6	FP-LAPW	[198]
		2.48, 2.47*	PAW	[204]
		2.32, 2.29*	PAW	[205]
		2.22		[200]

*Surface layer relaxation included.

8.2.1   Growth and stress of Fe on Ag(001)

Here, I discuss the stress results of Fe on Ag(001) presented in Chapter 5.1, in view of growth mode of the Fe films. I start with the stress of Fe deposited at 298 K, shown in Fig. 5.1. The film stress is separated into regions where the stress curve changes its slope. The first region already reveals a deviation from the misfit stress. In region I, two aspects need to be considered, surface stress and misfit stress. For the first 0.5 ML of Fe deposition, the stress is 0.2 GPa larger than the calculated misfit stress (+1.7 GPa). This implies a small tensile stress contribution from the surface stress change. It is not obvious which surface stress value to choose for Ag(001) and Fe(001) due to the wide spread surface stress values found in the literature [195–198].

Table 8.1 shows the calculated surface stress and surface free energy of Fe and Ag. The Table 8.1 reveals variations on surface stress and surface free

energy, for different calculations method. The surface free energy obtained for Fe is always larger than for Ag. In contrast, for the surface stress there is no clear tendency. The range of surface stress values of Fe(100) and Ag(100) are 0.5-1.3 N/m and 0.8-1.6 N/m, respectively. Based on the surface stress from Table 8.1, predicting the change of surface stress is prone to errors, as the difference of the surface stress $(\tau_{\text{Fe}} + \tau_{\text{Fe-Ag}} - \tau_{\text{Ag}})$ can result in either positive or negative stress. And in view of interfacial intermixing the interface stress $(\tau_{\text{Fe-Ag}})$ cannot be simply neglected. Thus, we can only conclude from the stress measurements that the resulting stress is tensile, which we assign to a change from a low surface stress, Ag(001), to a higher tensile surface stress for Fe/Ag(001). Thus, the stress data suggests a larger surface stress for Fe(001) as compared to Ag(001).

The stress curve reveals an unexpected compressive stress in region II in Fig. 5.1. To elucidate the nature of this inversion of stress, we consider the role of the growth mode. The deposited material can form islands on the substrate, or it can alloy into the first or deeper layers. The resulting surface alloy formation is linked to surface segregation [199, 206, 207].

Interface formation Fe/Ag(001)

The segregation energy is the energy cost of transferring a solute atom (in this case the deposited material - Fe) from the interior to the surface of a host crystal (substrate - Ag). Thus, the segregation energy is the difference in the total energies of the system with the impurity in a surface layer and within the bulk ($E_{\text{segr.}} = E_{\text{impur. on surf}} - E_{\text{impur. in bulk}}$). A positive segregation energy means the solute favors to be inside the substrate bulk. A negative segregation energy indicates that the impurity tends to stay on the substrate surface.

Another important indicator for segregation are structural relaxations. In conjunction with the segregation effects one can determine whether the solute will form a solid solution (mixed phase) or separated phase (the solute atoms stick together). For a negative value of the mixing energy the tendency is a repulsive interaction between the solute atoms, resulting in a solid solution. For a positive mixing energy the deposited elements attract each other, and a phase separation is expected.

Table 8.2 shows the calculated segregation energy for the Fe/Ag system from different references.

For the Fe/Ag(001) system, the segregation energy is calculated as +0.41 eV/ atom and the mixing energy of −0.15 eV/ atom [207]. This means Fe has a tendency to go into the bulk of Ag where it forms a Fe-Ag solution. Diffusion processes will lead to a mixed interface.

Table 8.2: Calculated surface segregation energy and mixing energy of Fe - bcc on Ag - fcc, from the surface free energy.

Material	Segregation energy (eV/atom)	Mixing energy (eV/atom)	Method	Reference
Fe/Ag	+0.54		KKR-ASA	[199]
	+0.41		KKR-ASA	[206]
	+0.41	−0.15	LMTO-ASA	[207]

The intermixing phase at the interface Fe/Ag has been observed experimentally [56–59, 153, 155, 157, 158, 163]. In a systematic work, Canepa and co-authors [56, 58, 153], observed evidence for interdiffusion of Fe and Ag. They proposed two consequences of this atomic interdiffusion: interface intermixing and substrate segregation. Substrate segregation means that substrate atoms migrate to the surface of the deposited film [56, 58, 153, 154], i.e. Ag diffuses to the top of the Fe film.

The interface formation between Fe and Ag depends strongly on the growth temperature. At low temperature, up to 250 K, Fe-Ag interdiffusion is restricted [56, 58, 153, 208] to the interface region. The diffusion occurs by atomic exchange. The region of coexistence of Fe and Ag, is limited to the interface. Hahlin and co-authors [163] conclude that the intermixing of Fe and Ag for deposition at 120 K affects the structure of the film up to 3 ML Fe deposition. They notice a pseudo phase transition from a bcc to a fcc-like structure in the Fe film. This structural modification induces a tetragonal distortion of the Fe film. The authors attribute this structural change to the presence of intermixing [163].

At higher growth or annealing temperature ($250 < T_s \leq 300$ K) an additional process occurs. The higher temperature results in a segregation of Ag to the top of the Fe film (Ag surface segregation), plus interfacial intermixing [33, 56, 156, 209]. At even higher temperature ($T_s \geq 450$ K) diffusion into the bulk increases, which can result in a dissolution of Fe in the bulk of the Ag crystal [153–156].

These temperature-induced diffusion phenomena need to be considered to appreciate the non-trivial stress behavior of Fe on Ag(001). The inversion of film stress, Fig. 5.1, to a compressive stress could be attributed to the atomic exchange and thermally activated diffusion between Fe and Ag. This results in an interfacial intermixing and Ag segregation on top of the Fe film. The direct evidence of Ag segregation was obtained from the AES analysis of the surface composition of thick Fe films. The AES results of as-grown 80 ML Fe, indicates the presence of Ag floating on top, see Fig.5.2b. Ag is successfully removed after short sputtering. From the sputtering rate and

exposure time, we estimate that 1 ML of Ag is floating on top of the Fe film grown at 298 K, in agreement with Ref. [33, 153].

We picture the interface Fe/Ag(001) as an Fe matrix with embedded Ag atoms, forming a coexisting region of Fe-Ag atoms. A way to look at the resulting stress is to imagine the growth of an Fe-Ag alloy on Ag. Several attempts to grow Fe-Ag alloy are described in the literature. Fe-Ag alloys have been prepared with different growth methods [210–215]. A metastable cubic phase of Fe-Ag alloy is obtained using sputtering, sol-gel method, laser deposition, and evaporation as growth techniques.

Krebs and co-authors [216], fabricate an Fe-Ag alloy film by pulsed laser deposition. They measured the in-plane lattice constant by grazing incidence diffraction experiments. They found that a film of $Fe_{83}Ag_{17}$ has an in-plane lattice constant 0.076 Å larger than the pure Fe film. This implies that the in-plane lattice constant of Fe-Ag alloy is 2.936 Å, in a cubic structure. Reference [211] investigated the structure of the Fe-Ag alloy with changing atomic concentration. They observe that Fe-Ag has a tendency to rearrange in a bcc lattice with increasing Fe concentration. Therefore, the misfit of Fe-Ag bcc ($a = 2.936$ Å) on Ag fcc ($a = 4.08$ Å) is calculated using Eq. 2.3 as

$$\eta = (a_{\mathrm{Ag}} - a_{\mathrm{Fe\text{-}Ag}})/a_{\mathrm{Fe\text{-}Ag}} = -1.73\%. \tag{8.8}$$

The expected stress calculated from the misfit in Eq. 2.4 takes into account the biaxial modulus of the film (Fe-Ag). In Ref. [211], the Young's modulus of the alloy was measured, They observed that the Y of the alloy approximates to Fe Young's modulus with increasing Fe concentration. The resulting stress is $\tau = -3.6$ GPa. This expected stress for the direct deposition of an Fe-Ag alloy on Ag(001) ($\tau = -3.6$ GPa) is much higher than the observed stress change in region II ($\tau = -0.05$ GPa), in Fig. 5.1.

This reference to the deposition of an Fe-Ag alloy is far from the real experiment, where only Fe is deposited. Consequently, we take this only as a qualitative hint, that a compressive stress change may be linked to an Fe-Ag alloy formation.

Further studies are called for to identify the interface structure of Fe on Ag(001). Hahlin and co-authors [163] explored the experimental results of X-ray absorption fine structure (EXAFS) for a 3 ML Fe film on Ag(001) to simulate the Fe/Ag interface. They mimic intermixing at the interface using model clusters to improve the agreement with experimental data. However, the crystalographic structure at the interface is more complex, and a definitive assignment of the crystal structure remains open [163].

Growth mode of Fe on Ag(001)

Studies of the growth mode of Fe on Ag(001) brought controversial conclusions. Reports of Frank-van der Merve (layer-by-layer) growth to Stranski-Krastanov (2D to 3D islands) growth mode were found [34–37,54–57,59]. The outcome is that the deposition rate and temperature play a crucial role for the growth mode. In this work, we kept the deposition rate fixed at 1 Å per minute as described in Section 3.4. I changed the deposition temperature to study the effect on film stress. In order to avoid solution of Fe in the Ag bulk higher deposition temperature than 298 K are not investigated.

The measurement of stress change is susceptible to changes in the growth process. A change in growth mode could produce remarkable and significant effects [51]. The stress during growth at 298 K, region IV in Fig. 5.1, reveals a small change in the slope. We attribute this change of stress to a change of growth mode. For this deposition conditions (298 K and 1 Å/min) the growth mode of Fe on Ag is Stranski–Krastanov with interdiffusion up to 5 ML. It changes to Frank-van der Merve plus interdiffusion at higher thickness. Ag segregation can be distinguished in thicker films, as discussed in Ref. [57]. Note that in thin films Ag segregation may also be expected, but it is not possible to identify the origin of the Auger signal as due to interfacial Ag or due to Ag segregation. The possibility of a change in growth mode of Fe on Ag promoted by Ag acting as a surfactant [33] can be considered. A flat Fe film under a surfactant is discussed for Fe/Au system [33]. This change in the growth mode was also observed by RHEED and LEED measurements [159, 217].

It is known that a growth temperature of 120-250 K restricts the interdiffusion to the interface according to Ref. [58, 59]. Other authors report, in Ref. [56, 163], that intermixing at this low temperature takes places mainly up to 3 ML. The growth is Stranski-Krastanov, and no evidences of change of growth mode has been reported.

The low temperature (200 K) stress measurement, in Fig. 5.3a, show a different behavior as compared to growth at 298 K. The film stress is described by three regions. The first region is attributed mainly to the change of surface stress. The tensile stress in the region I is +2.7 GPa. This is larger as compared to growth at 298 K. A quantitative analysis suffers from the considerable spread of surface stress data, as showed in Table 8.1. As mentioned in the beginning of this section the huge range of surface stress obtained from literature for each element would allow both possibilities, a negative and a positive surface stress change. We only can conclude that the surface stress contribution appears to be more dominant for low temperature deposition.

In region II of Fig. 5.3a, the slope of the stress curve changes to +1.0 GPa. This change is confined to an Fe thickness range of 0.5 to 3 ML. We deduce that the thermal energy at 200 K is not sufficient to allow Ag atoms to segregate to the top most layer at higher Fe film thickness. This stress change compared to deposition at 298 K is ascribed to the reduced interdiffusion. The interdiffusion at 200 K gives rise to interfacial intermixing up to 3 ML [56, 163], which is the thickness where the slope of the stress curve changes again.

The interfacial intermixing at 200 K is expected to be strongly reduced as compared to deposition at higher temperature. Thus, a reduced interfacial intermixing may result in the absence of the compressive stress in the region II, in agreement with our results in Fig. 5.3a.

Region III in Fig. 5.3a is reached after 3 ML Fe deposition, a tensile stress of +0.7 GPa is observed up to the end of 13 ML deposition. The stress observed in region III is considerably less than for deposition at 298 K.

The Stranski-Krastanov growth mode can impact the stress relaxation in the islands. The smaller stress in the film might be the result of the film morphology, showing small islands. A relaxation at the edges of the islands leads to a reduction of stress [218, 219]. Film dislocations are further mechanism for stress reduction [143]. However, there is no evidence for misfit dislocation formation from the structural analysis, see below. Therefore, this reduction of stress may be related to the growth mode of Fe on Ag at low temperature.

The structural measurements, presented in Chapter 5.1, show differences in the films grown at different temperatures (200 and 298 K). The increase of intensity and sharpness of the LEED diffraction spots at 200 K is ascribed to the absence of Ag segregation. The suppression of segregation and a reduced intermixing also give rise to a smaller Ag/Fe ratio in AES as compared to 298 K deposition, as observed in Fig.5.3b and c.

In conclusion, the stress measurements at different growth temperatures provide new insights into the growth processes of Fe on Ag(001). We shed new light on the interdiffusion process, and its impact on growth mode, interfacial intermixing and Ag surface segregation. Stress measurements identify different modes of interface formation during Fe growth on Ag(001). A compressive stress as an indicator for pronounced interdiffusion during deposition at 298 K was discussed. This compressive stress is mainly observed due to interfacial intermixing during deposition. The stress measurements also indicate the change in growth mode for depositions at 298 K where a tendency of layer-by-layer growth is found in thicker films. In comparison, the film grown at 200 K presents reduced interfacial intermixing with negligible surface segregation and no change in growth mode [56]. Therefore, the stress results during Fe deposition at 200 K reveals no compressive stress and no

a) growth at 298 K   b) growth at 200 K

Ag segregation
Fe film
Mixed interface

Ag substrate

● Ag atoms
● Fe atoms
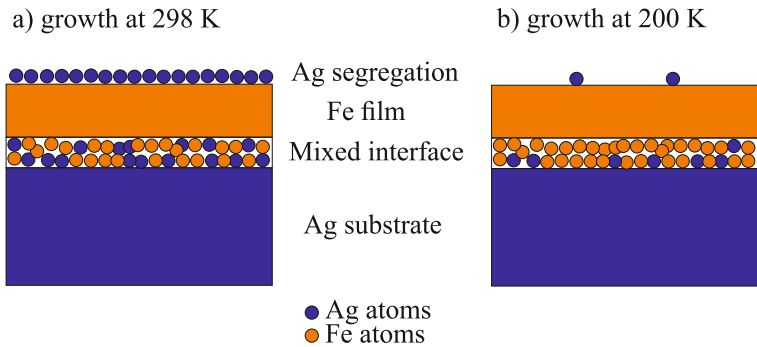
Figure 8.4: Schematic of the Fe film on Ag(001) for growth at a) 298 K and b) 200 K. The interfacial intermixing and Ag segregation are represented.

change of slope for thicker films.

These findings indicate the drastic influence of temperature on the interface formation of the resulting stress change of the Fe/Ag(001) system. This temperature-dependence is also evident in the magnetoelastic coupling measurements as discussed in Section 8.3, when the change of morphology leads to a reduced magnetoelastic stress for low temperature deposition.

In summary, our results corroborate the view that Fe growth at 298 K leads to interfacial mixing of Fe-Ag, where the interface is capped by a complete Fe film, which is covered by 1 ML of Ag floating on top [33, 153]. The growth mode changes for Fe films thicker than 5 ML [159, 217]. For growth at 200 K, we deduce a Stranski-Krastanov growth mode with much less interfacial mixing and absence of Ag segregation on top of the Fe film [56]. Figure 8.4 shows a schematic of the Fe film grown on Ag(001) for different growth temperature, following the conclusions extracted in this work.

Next, a corresponding analysis of the stress signature is performed for Fe growth on Au(001).

8.2.2 Growth and stress of Fe on Au(001)

Here, I discuss the stress results of Fe on Au(001) presented in Section 6.1, Chapter 6. The analysis is done in view of film structure, intermixing, and segregation of Fe on Au(001).

Our result of the stress change during growth of Fe on Au(001) at 298 K reveals a deviation from the calculated misfit stress. The film stress as a function of Fe deposition from Fig. 6.1a was separated in three regions, given by the change of slope of the stress curve. In region I, the observed stress change includes contributions of surface stress and epitaxial misfit stress. In

this region a small stress peak below 0.5 ML Fe deposition is observed. This region is discussed below, and it is proposed that it is linked to the lifting of the (1×5) reconstruction of Au(001) surface [42, 61].

Lifting of the surface reconstruction: Au(001)-(1×5)

Figure 6.1b, in Section 6.1, shows the LEED pattern of clean Au(001) and after 0.5 ML Fe deposited. The LEED images reveal the diffraction pattern indicative of the (1×5) reconstruction for the clean Au surface, and it shows a (1×1) pattern for the epitaxial Fe film. We conclude that 0.5 ML Fe is sufficient to lift the (1×5) surface reconstruction of Au(001).

The lifting of the surface reconstruction of Au has been reported before to occur after 0.4 ML of Fe deposition [42, 61], in good agreement with our results.

The non-reconstructed (1×1) surface of Au(001) can be prepared by a reactive ion bombardment following the procedure from Ref. [151]. The Au(001) surface is submitted to an O-sputtering (ion energy 200 eV) at 1 μA for 60 minute. The bombarding species remain as impurities just after the sputtering. Within minutes the amount of O-ion at the surface is considerably reduced due to desorption. As pointed out by Ref. [151], the surface structure does not change during this desorption, and it remains (1×1).

To observe the difference of stress change, I deposited Fe on Au-(1×1) (001), after the cleaning procedure described above. The stress results of Fe/Au-(1×1) is shown in Fig. 8.5.

Figure 8.5a shows the deposition of 25 ML Fe on Au(001) (1×5) and on the unreconstructed Au(001)-(1×1). The regions I, II, and III show the change of slope as described in Section 6.1. The stress measurement of Fe deposited on Au with the (1×1) surface is presented in Fig. 8.5a, in red. The black curve shows the stress change for deposition on the (1×5) surface, for comparison. The zoom-in of deposition up to 2 ML Fe is presented in Fig. 8.5b. Region A in Fig. 8.5b, shows the Fe deposition up to 0.5 ML. This region highlights the stress where the surface (1×5) is lifted. The curves differ from each other. The region of interest here is the labeled region A, for the stress curve below 0.5 ML Fe. A small depression is observed at 0.25 ML for the black curve, whereas the red curve shows a shoulder-like peak.

This difference of the stress curves could be due to 1) the lifting of the Au reconstruction, or 2) a result of a change of growth mode due to the different surface roughness. A third 3) possibility for the stress difference can be related to contamination of the (1×1) surface by Oxygen. LEED and AES of the Au(001) cleaned with both procedure, Ar-sputtering plus annealing and O-sputtering, are shown in Fig. 8.6a. The spectra are identical with the main
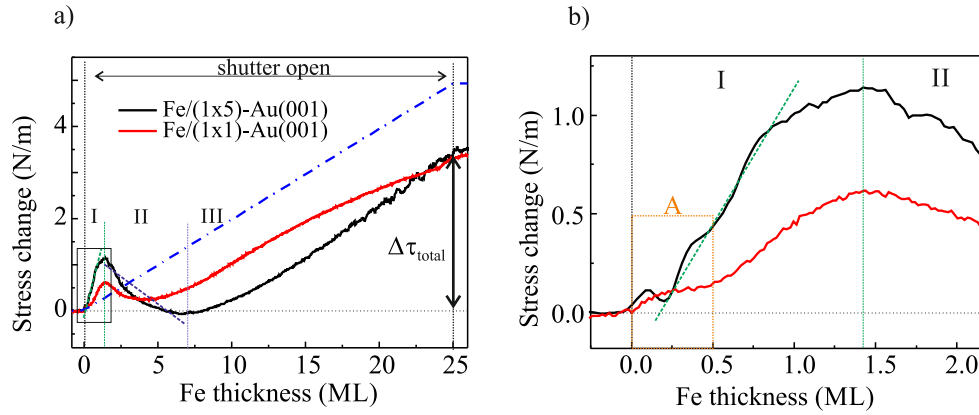
Figure 8.5: a) Film stress change during Fe deposition on Au(001) on different surfaces, reconstructed (1×5) (black curve), and unreconstructed Au(001) (1×1) (red curve). b) The zoom-in shows the stress change up to 2 ML deposition. Region A presents the stress during Fe deposition where the lifting of the surface reconstructuion is observed at 0.5 ML.

peaks at 69, 150, and 239 eV of clean Au, also presented in Section 3.4. The LEED pattern at 58 eV of each surface is inserted. The LEED diffraction reveals a distinct pattern of (1×5) and (1×1). The LEED diffraction of the (1×1) surface shows blurred, broad diffraction spots, in contrast to the (1×5) pattern. The poor long range order of the unreconstructed surface suggests that a rough surface is obtained after the cleaning procedure. The surface roughness can be reduced upon annealing, however, high temperature initiates the surface reconstruction. Therefore, annealing after O-sputtering was not performed.

Figure 8.6b shows the Auger spectra of 25 ML Fe deposited on different Au surfaces. After Fe deposition the main peak of Au at 69 eV, and the three Fe peaks at 598, 650, and 703 eV are visible. The intensity peak of Au of both curves differ and in the blue spectrum a peak at 503 eV is visible. The AES peak at 503 eV is attributed to the presence of oxygen at the surface [220]. Oxygen contamination is a result of the adopted preparation procedure to remove the surface reconstruction. As pointed out in Ref. [151] during the preparation procedure O-ions are implanted in the bulk. Although the AES of the crystal looks free of oxygen, after Fe deposition the oxygen implanted in the bulk comes near the surface and the AES peak at 503 eV becomes visible.

The question of the stress signature of the lifting of the reconstruction is still open. The roughness and the implanted ions make this procedure under
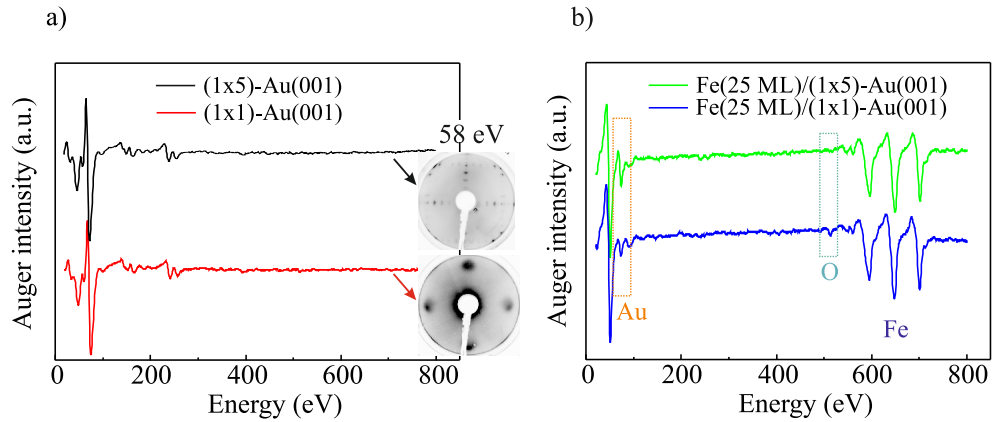
Figure 8.6: a) Auger spectra of the clean Au - (1×5), in black, and the (1×1) surface, in red. The respective LEED diffraction at 58 eV is identified by the color code arrows. b) The AES after deposition of 25 ML Fe on the (1×5) and the (1×1) surface are plotted in green and blue, respectively. The LEED image is inverted, dark means high, and white means low intensity. The Auger spectra are vertically shifted for sake of visualization.

in its analysis with respect to surface reconstruction. Further investigations with different procedures to obtain Au(001)-(1×1) are needed.

Interface formation Fe/Au(001)

I continue to discuss the stress of Fe on Au(001)-(1×5) grown at 298 K, see Fig. 6.1a .

After the small stress peak in region I, the measurement reveals a slope indicative of a tensile stress of +5.5 GPa. This stress is four times larger than +1.4 GPa calculated from misfit. This implies that the change in stress has a strong contribution from surface and interface stress. A huge range of surface stress values for Au and Fe are reported in literature. Table 8.3 compiles the values of surface stress and surface free energy from the literature of Au(001) and Fe(001).

Similar to the Fe/Ag system, Fe and Au are presented with several values of surface stress and surface free energy for different calculations. All values for the surface free energy of Fe(001) are larger than the calculated surface free energy of Au(001). However, the surface stress reveals no clear tendency for Fe and Au.

The range of surface stress values of Fe(100) and Au(100) are 0.5-1.3 N/m and 0.9-2.9 N/m, respectively. Based on Table 8.3, predicting the contribu-

Table 8.3: Calculated surface stress τ, surface free energy γ of Fe and Au. The methods of calculation are indicated: FP-LAPW full potential linear combination of augmented waves, FS: empirical n-body Finnis-Sinclair potencial, EAM: embedded atom method, EMTO: exact muffin-tin orbitals, FPLO: full-potential local-orbital , PAW: projector-augmented-wave. Compilation from [49].

Material	Surface stress $\tau_{[001]}$ (N/m)	Surface free energy γ (J/m^2)	Method	Reference
Au(001)		1.88	KKR-ASA	[199]
	0.92	1.79	AEM	[195]
	2.9, 1.8*	0.79, 0.77*	FS	[196]
		1.6		[200]
		1.3		[201]
		1.6		[202]
Fe(001)	0.5	2.45	EMTO	[203]
	1.39*	2.55, 2.50*	PAW	[198]
	0.57	2.62	EMTO	[197]
	1.15	3.09, 3.07*	FPLO	[197]
		2.6	FP-LAPW	[198]
		2.48, 2.47*	PAW	[204]
		2.22		[200]
		2.32, 2.29*	PAW	[205]

*Surface layer relaxation included.

tion of surface stress on the stress change is prone to errors, as the change of the surface stress $(\tau_{\text{Fe}} + \tau_{\text{Fe-Au}} - \tau_{\text{Au}})$ can result in either positive or negative stress. And in view of interfacial intermixing the interface stress $(\tau_{\text{Fe-Au}})$ cannot be simply neglected. Thus, we can conclude from the stress curve that a change from low surface stress, Au(001), to higher tensile surface stress for Fe/Au(001) is observed. This suggests a larger surface stress for Fe(001) as compared to Au(001).

This region I, where the surface stress has a strong contribution, lasts up to 1.5 ML of Fe deposition. Then a compressive stress is observed, which defines region II. Region II, in Fig. 6.1a, extends from 1.5 to 7.5 ML of Fe deposition. In this case, in contrast with Fe/Ag, the compressive stress is larger and extends to higher Fe thickness. To elucidate the nature of this compressive stress, we recall the investigation on the surface segregation of Ref. [199, 206, 207].

A reminder: segregation energy is the energy cost of transferring a solute atom from the interior to the surface of a host crystal. A positive segregation

Table 8.4: Calculated surface segregation energy and mixing energy of Fe - bcc on Au - fcc.

Material	Segregation energy (eV/atom)	Mixing energy (eV/atom)	Method	Reference
Fe/Au	+0.61		KKR-ASA	[199]
	+0.45		KKR-ASA	[206]
	+0.50	+0.76	LMTO-ASA	[207]

energy means the solute favors to be inside the substrate bulk. A negative segregation energy indicates that the impurity tends to stay on the substrate surface. In a positive segregation energy the mixing energy can also be calculated. For a negative value of the mixing energy the tendency is a repulsive interaction between the solute atoms, resulting in a solid solution. For a positive mixing energy the deposited elements are under an attractive interaction, and a phase separation is expected.

Table 8.4 shows the segregation energy calculated for the Fe/Au system.

Accordingly to Table 8.4, Fe on Au presents a positive segregation energy of +0.50 eV/atom and a mixing energy of +0.76 eV/atom [207]. As discussed above for Fe/Ag, the positive segregation energy suggests that Fe atoms prefer to go into the Au bulk. In contrast, the positive mixing energy indicates a preference for phase separation in the mixing interface. This means Fe tends to cluster together, instead of binding with Au atoms.

Therefore, we attribute the compressive stress to the interdiffusion process, which results in interfacial intermixing of Fe-Au. The atomic exchange between Fe and Au has been observed experimentally [40,41,62]. Similar to Fe/Ag, the interdiffusion is thermally activated [41,62], and results in Au surface segregation in addiction to the interfacial intermixing [40].

The higher compressive stress as compared to Fe/Ag could result form the different mixing energies. The mixing energy in Fe/Au is positive, which suggests Fe clustering in the Au bulk. The interface of Fe/Au has been discussed in Refs. [38,40,62] in view of temperature-induced interterdiffusion. The authors conclude that the interdiffusion during deposition of Fe on Au at room temperature results in Au segregation on top of the Fe film and interfacial intermixing.

An analysis of the expected stress at the interface due to the intermixing was made in the previous Section 8.2.1 for Fe/Ag. We follow a corresponding analysis here for Fe on Au(001).

Fe-Au alloys have been reported before [43,221,222]. At room temperature a tetragonal $L1_0$ structure is expected. However, the structure and distribution of the intermixing at the interface has not been resolved yet [41,43,60].

Table 8.5: Calculation of misfit η and stress τ from the lattices parameters given in Ref. [224].

Alloy	Fe lattice a (Å)	misfit η (%)	stress τ (GPa)
Fe_1/Au_5	2.91	-1.0 %	-2.0
Fe_1/Au_4	2.99	-3.6 %	-7.5
Fe_1/Au_1	$2.81 + 0.32 = 3.13$	-7.9 %	-16
Fe_1/Au_3	$2.81 + 0.17 = 2.98$	-3.3 %	-6.9

To investigate the influence on magnetic properties, several structures of the Fe-Au alloy were considered [221, 223, 224].

Sternik and co-authors [224] calculated the structure and formation energies of Fe_n/Au_m alloys and superlattices. We choose four combinations for Fe-Au alloy structures, which have minimum energies and atomic stability.

From the in-plane lattices and in-plane dislocations given in Ref. [224] we calculate the expected misfit η, with Eq.2.3, and the respective stress τ, with Eq. 2.4, representing the deposition of an Fe-Au alloy on Au(001). The lattice parameters, from ref. [224], and the calculated misfit and stress results are given in Table 8.5.

It is important to notice that all suggested configurations of Fe-Au alloys result in a compressive misfit stress. For Fe on Au(001) this compressive stress, in region II of Fig. 6.1, is observed from 1.5 to 7.5 ML Fe with a magnitude of -1.3 GPa. The results of expected stress shown in Table 8.5 do not reproduce the same magnitude of compressive stress observed experimentally. The simulation of an Fe-Au alloy deposition on Au(001) is far from the real experiment, where only Fe is deposited. This approximation of the deposition of Fe-Au alloy gives only a qualitative result, which is a compressive stress change.

In region III of Fig. 6.1a the stress curve shows a positive slope. The slope represents a tensile stress of $+1.5$ GPa. The slope of the stress change is close to the calculated misfit stress of $+1.4$ GPa. We conclude that in region III misfit is the main origin of film stress. The LEED results, Fig. 6.2a, show sharper and more intense diffraction spots after 10 ML Fe deposition. This is attributed to the improvement of the long range epitaxial order. To understand this improvement of the LEED diffraction pattern we discuss the growth mode of Fe on Au(001) next.

Growth mode of Fe on Au(001)

The impact of Au segregation on the growth mode of Fe on Au(001) has been heavily investigated. Some authors consider that Au atoms act as a surfactant, promoting a Frank-van der Merwe growth mode leading to a flat Fe film [38,39,41–43,60]. In contrast, other authors concluded that Fe grows in the Stranski-Krastanov mode [40,61,62].

According to Ref. [38,42] the interdiffusion of Fe starts after 0.5 ML, facilitated by the lifting of the reconstruction surface, and continues up to 5 ML. This interdiffusion is affected by temperature and results in Au segregation and/or interface intermixing [225,226]. Thus, temperature-dependent stress measurements have the potential to clarify the interfacial process.

Stress measurements at different growth temperature are qualitatively similar, and show only some quantitative differences, see Fig. 6.3. In contrast to Fe/Ag, the compressive stress is also observed at all deposition temperatures (200 K - 375 K). This indicates that interdiffusion of Fe/Au(001) is not strongly affected in this range of growth temperature. Therefore, the intermixing at the interface is not significantly reduced even for deposition at 200 K. The differences of the stress curves in Fig. 6.3 could also be ascribed to a change in film roughness during growth [39], and to the variation of Au surface segregation.

A recent study of the implications of Au segregation on Fe film growth on Au(001) was made in Ref. [227]. The authors observed an increase of roughness as a function of increasing Fe thickness for deposition at room temperature. They attribute the increase of roughness to the reduction of Au surfactant coverage as the Fe thickness increases. Furthermore, they discuss the development of film roughness and Au segregation upon annealing. They observe that the roughness of the film is reduced with increasing annealing temperature, and Au segregation is enhanced [227]. This suggests that the increase of temperature will induces a flatter Fe film with increased Au segregation. This finding speaks in favor of the change of film roughness with variation of growth temperature. Thus, the quantitative changes of the stress curves are ascribed to a change of film roughness.

Distinct and prominent changes are observed, however, in the LEED and Auger results, presented in Fig. 6.4a and b.

The Auger spectra show an increase of the ratio Au/Fe with increasing growth temperature. We assign this result to the increased Au coverage floating on top of the Fe film, as suggested in Ref. [227]. The increased amount of Au segregation affects even the crystalline order of the surface, as seen in LEED measurements. LEED shows sharper, more intense diffraction spots as the deposition temperature is increased. Also, a split of the (1,0)
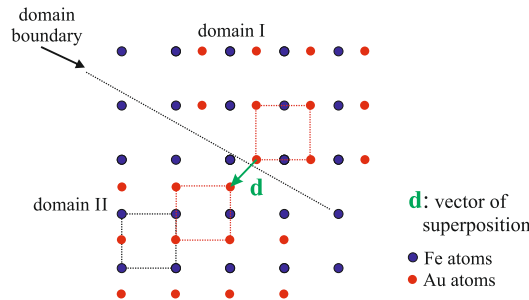
Figure 8.7: Model of the surface structure of two antiphase domains with an antiphase boundary, where the Au atoms form subdomains with (1×1) patterns with two-fold symmetry on Fe(001).

and (0,1) beams is observed, as shown in the sketch of Fig. 6.4b.

The split of the LEED spots are normally associated with changes of structure and with the formation of a superstructure [143, 228, 229]. The diffraction pattern due to the superstructure is improved with increasing temperature [143]. A weak superstructure has been reported for a 2 ML Fe film deposited on Au(001) at 570 K [62], while the (1×1) beams remained very sharp and intense. The authors [62] suggest that the appearance of superstructure is related to the intermixing or alloy formation in the surface region due to the increased temperature. This hypothesis is supported by a gentle 1 min sputtering, which removes the extra spots in LEED and the Au peaks in AES.

The additional spots on LEED, at specific diffraction positions, are predicted to arise due to surface structure, as discussed by Ref. [175]. Similar split spots were a specific observed for chlorine chemisorbed on W(001) [175].

According to Ref. [175], the split is the result of surface domains with (1×1) structure, which are dislocated in relation to similar domains. These domains preserve the long-range order, but due to the existence of subdomains of equal structure out-of-phase, a superposition of the diffraction of both structures is observed. These domains are arranged in a fashion that result in a splitting of specific beams of the diffraction pattern, in this case equivalents (1,0) and (0,1) beams.

Estrup and co-author [175] present a model to explain the split of only specific beams. Figure 8.7 represents in hard spheres a sketch of this model.

Figure 8.7 shows two different Au domains, labeled I and II. In [175] the subdomains have a (1×1) unit cell with two-fold symmetry. The structure model shown in Fig. 8.7 represents a surface structure of the Fe film with the Au atoms on top with two-fold symmetry on Fe(001). The vector d

represented in Fig. 8.7 connects the boundary of these two domains. The vector d satisfies $\mathbf{d} = d_1\mathbf{a_1} + d_2\mathbf{a_2}$, where d_i are integers and $\mathbf{a_i}$ are the reciprocal vectors.

The reciprocal net vector of a reciprocal point to the origin is $\mathbf{u} = h\mathbf{a_1^*} + k\mathbf{a_2^*}$, where h and k are the integers associated lattice rods and $\mathbf{a_{1,2}^*}$ are perpendicular reciprocal vectors.

The condition of a split diffraction beam is determined by a modulating function,

$$hd_1 + kd_2 = \frac{1}{2}(2n+1), \tag{8.9}$$

where n is an integer. The beams that split are determined by the vector d. The prediction of a splitting of the (1,0) and (0,1) beams, but not of the (1,1) beam, results when $\mathbf{d} = \frac{3}{2}\mathbf{a_1} - \frac{1}{2}\mathbf{a_2}$. Therefore, the Eq. 8.9 results in $3h - k = 2n + 1$ and yields a split on (1,0) and (0,1) beams.

This model describes the split of specific diffraction spots in good agreement with our experimental observations. However, the observation of additional spots in LEED is not sufficient to reveal the origin of this structure. Further investigations are needed to determine exactly the domain orientation in our system. Thus, an indication of superstructure induced by higher temperature is observed in the LEED results. The splitting of diffraction spots (1,0) and (0,1), in Fig. 6.5b, suggests an ordered surface structure, which is arranged in domains on top of the Fe film. The formation of the superstructure by surface alloying or diffusion has been observed for other systems, such as Ag-Cu, Ag-Ni, and Ag-Si [230–232]. Therefore, a superstructure resulting from intermixing or alloy formation in the surface region is a reasonable description for the Fe films on Au discussed here.

In summary, the film stress analysis of Fe on Au(001) sheds new light on the interdiffusion process. In all growth temperature investigated here the diffusion impacts the interfacial structure of the Fe films. From our stress results we identify distinct processes during growth. The Au reconstruction is lifted as indicated by a small depression on the stress curve at 0.3 ML Fe deposition. A compressive stress is the signature of the interdiffusion of Fe into Au. The variation of growth temperature results in a different consequence of this interdiffusion. Growth at 200 K gives rise to an almost exclusive interface intermixing. With increasing temperature the intediffusion result in an interfacial intermixing with additional Au segregation. The amount of Au floating on top of the 25 ML Fe film at 298 K is estimated to be 0.5 ML of Au. From the structural point of view, the film maintains its (1×1) epitaxial long range order. However, the temperature dependence of the stress change reveals only minor changes of stress due to increasing Au segregation. A possible intermixing/alloy at the surface for higher growth temperature may
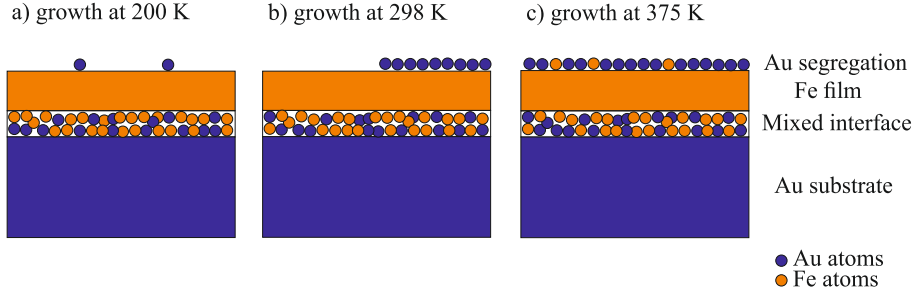
Figure 8.8: Schematic of the Fe film growth on Au(001) at a) 200 K, b)298 K and c) 375 K. The interfacial intermixing and Ag segregation are represented.

induce domain formation, which can be observed by LEED measurements. Figure 8.4 shows a schematic of the Fe film grown on Au(001) at different growth temperature, in view of interface intermixing and Au segregation.

The compressive stress observed on Fe/Au(001) is ascribed to interfacial intermixing. This is an important finding, as the interface on this system brings questions concerning the intermixing of the materials. We conclude that intermixing at the interface is observed in both systems, Fe/Ag and Fe/Au, at 298 K and it is identified a compressive stress in the stress measurements. However, the compressive stress is more pronounced in Fe/Au as compared to Fe/Ag. This difference could be related to the presence of surface reconstruction in Au(001) and not in Ag(001). As pointed out by Ref. [38] the interdiffusion of Fe on Au is facilitated by the lifting of the surface reconstruction after 0.5 ML Fe deposition. Another possibility for this difference in the interdiffusion process is the difference in the calculated mixing energy, or the difference of surface free energy, shown in Tables 8.1, 8.2 and 8.3, 8.4 for Fe/Ag(001) and Fe/Au(001), respectively. The exact origin of the difference of the interdiffusion in Fe/Ag(001) and Fe/Au(001) needs further investigations. Another aspect discussed in this thesis was the surface segregation. The surface segregation shows pronounced dependence on the growth temperature. The deposition temperature varies the amount of surface segregation in both systems, in agreement with previous works [39, 56, 159, 217, 225, 226]. This change of amount of segregation and intermixing may impact the magnetoelastic properties of the films. Thus, this discussion is presented in Section 8.3.

8.2.3   Au surface reconstruction and Fe/Au/Fe structure

In the discussion of the growth of Fe on Au(001) in Section 8.2.2, I pointed out that a critical thickness of Fe deposition lifts the Au-(1×5) surface reconstruction. Now, in the process to prepare trilayers of Fe/Au/Fe on Au(001) presented in Chapter 7, I deposit Au on Fe/Au(001), allowing a discussion of the critical thickness to recover the surface reconstruction in a growing Au film. Before going into details of the reconstruction process, I briefly discuss the film stress of the Fe layers on the Fe(15 ML)/ Au(X ML)/ Fe(10 ML) trilayers on Au(001) from Section 7.1.

I investigated trilayers of Fe/Au/Fe, with a Fe thickness of 10 ML for the inner film and 15 ML for the film on top. The stress behavior during Fe growth, see Fig. 7.1a, is consistent with that found for a single film of Fe on Au(001), presented in Section 6.1 and discussed above. The film stress is fairly independent of the Au spacer layer thickness. However, we found a minor change of the Fe-induced stress for small Au coverage below 2 ML, in Fig. 7.1a. This has been ascribed to the difference in the surface structure of Au(001) and of the Au film, as evidenced by LEED, in Fig. 7.2b. The LEED results show broader spots in a (1×5) pattern for the Au film. This contrasts with the very sharp spots observed for the Au(001) substrate bulk crystal. The reason for this structural difference is the higher temperature that the crystal was submitted before deposition, which reduced roughness and improved the crystalline order of the surface. Therefore, the deviation of the stress results of the Fe films is attributed to the difference of roughness of the Au surface. However, the stress curves of Fe on both, Au film and Au crystal, present no drastic variations. Thus, similar interfaces are expected for Fe on Au(001) and of Fe on Au/Fe/Au(001). In preparations of trilayers the similarity of interfaces plays an important role, as additional interface effects can be ruled out [184, 223, 233].

The new aspect of the Fe/Au/Fe/Au(001) trilayer preparation is the Au film deposition. The Fe film is epitaxially strained on Au(001). Therefore, in principle, no misfit stress is expected for the Au film growth on Fe/Au(001). However, film stress reveals a prominent compressive stress, regions I and II, and after 3 ML of Au a tensile stress is observed in region III, in Fig. 7.1b.

The stress for the first 0.5 ML of Au, region I, is assigned to the change of surface stress. The change in surface stress shows an inverted sign in the stress curve as compared with Fe on Au. Thus, the slope of the curve indicates an expected compressive stress. As the Au thickness increases, the compressive stress becomes smaller, indicated by region II. This second region on the slope stress last up to 3 ML. In this Au thickness range the

reappearance of the (1×5) reconstruction is observed by LEED, see Fig. 7.1c. Therefore, we attribute the slope of −4.0 GPa to the formation of the Au surface reconstruction.

The initial (1×1) surface from epitaxial growth of Au on Fe/Au rearranges in the topmost atomic layer to a quasi-hexagonal closed packed arrangement in a (1×5) structure. The driving force for this surface reconstruction is that the energy gain associated with the increase of surface atom density overcomes the energy cost of bond rearrangement, which accompanies the reconstruction [50].

A crude estimate of the energy cost to form the reconstructed surface is obtained from the surface free energy. Since the Au(111) and Au(100)-(1×5) surfaces have hexagonal structures, the surface energy of reconstructed Au(100) is assumed to be the same as the energy of Au(111).

Therefore, the energy involved in the reconstruction of Au(100) can be described as [50]:

$$\Delta E = (\gamma_{111} - \gamma_{100})A, \tag{8.10}$$

where A is the surface area, and γ_{111} and γ_{100} are the surface free energy of the unreconstructed (111) and (100) Au surface, respectively. The change in surface stress is calculated as

$$\Delta\tau = \frac{\partial \Delta E}{\partial A} = (\gamma_{111} - \gamma_{100}) + A\frac{\partial \gamma_{111}}{\partial A} - A\frac{\partial \gamma_{100}}{\partial A}, \tag{8.11}$$

which is

$$\Delta\tau = \tau_{111} - \tau_{100}. \tag{8.12}$$

With the values of surface stress of τ_{111}=2.77 N/m and τ_{100}=4.56 N/m [50] a compressive stress of −1.79 N/m is expected.

In Ref. [185], the authors performed experiments on a cantilever Au crystal to obtain the change in stress due to surface reconstruction. The experiment explored the bias voltage dependence in an electrochemical cell to form and destroy the surface reconstruction on a Au(001) single crystal immersed in a 0.1 M $HClO_4$ solution. A negative potential induces the surface reconstruction, and a positive potential lifts the reconstruction. The authors [185] noticed that after a few cycles of the electrochemical potential the restoration of the reconstruction was suppressed. The authors followed the idea to compare the stress in the first cycle, where about 50% of the surface area was reconstructed, with the stress after several cycles, when the surface remains (1×1). They found a stress change of 0.24 N/m [185], which corresponds to a reduction on the tensile surface stress of only 5%. They conclude that the driving force for reconstruction surface on Au(001) is not the relaxation of tensile surface stress, in contradiction with calculations [234].

In this thesis, however, the system is different. The atoms needed for the reconstruction are supplied externally (deposited Au). There is no Au deposition in the previous works [185, 234]. The stress change due to surface reconstruction measured in this thesis is ≈ -1.1 N/m. This value is comparable to the calculated -1.79 N/m by [50], but much larger as compared with the compressive stress of -0.24 N/m from Ref. [185]. This variation can be related to the Fe substrate, or the coverage of surface reconstruction. Ref. [185] observed a coverage area of 50% of reconstruction for the first cycle. The larger stress change as compared with the experimental result in [185] can be a result of the larger reconstruction area. Further investigations with a direct analysis of the surface morphology, e.g. by STM, is necessary to obtain the coverage of surface reconstruction in our samples. Furthermore, in a qualitative analysis we ascribe the compressive stress observed in region II to the reconstruction of the Au surface.

The compressive stress due to the reconstruction continues up to 3 ML, where the curve changes to a tensile stress, see region III in Fig. 7.1b. The stress of Au on epitaxial Fe/Au(001) shows unexpectedly a tensile stress of +1.8 GPa after 3 ML of Au. Since the Fe film shows the lattice constant of the Au substrate, and after the surface reconstructed (1×5) is formed, the continuous deposition of Au should, in view of lattice strain, correspond to zero strain, and correspondingly zero stress was expected.

Figure 8.9 shows the stress result of Au deposited directly on Au(001)-(1×5) at 298 K. Remarkably, Au growth induces a tensile stress of +1.2 GPa, even for what is expected to be misfit free growth. Simultaneous *in-situ* MEED shows oscillations in Fig. 8.9. The maxima of the MEED intensity are ascribed to a completed Au layer. These MEED oscillations suggest Frank-van der Merwe growth. This measured stress of +1.2 GPa corresponds to an hypothetical misfit of 0.1%.

Periodic changes are also observed in the slope of the stress curve in Fig. 8.9. MEED and stress oscillations have been reported before for Co/ Cu(001) [218] and FeMn/ Cu(001) [219]. The authors ascribe the MEED and stress oscillations to the film growth in a layer-by-layer mode. In Ref. [218] they conclude that the peaks of the MEED oscillations of Co/ Cu(001) is the signature of a filled layer. Therefore, we ascribe the oscillations in MEED and in the stress curve to the layer-by-layer growth of Au/ Au(001).

The tensile stress of +1.2 GPa comes as a surprise. It is known that Au on Au(001) self-diffuses to minimize the energy of the system [173, 235, 236]. The predominant growth mechanism is an atomic exchange, where the deposited Au atoms diffuse under the surface. Therefore, we assign the stress of +1.2 GPa for Au/Au(001) to the self-diffusion of the system, and not to strain. This finding sheds light on the tensile stress observed in the Au film on
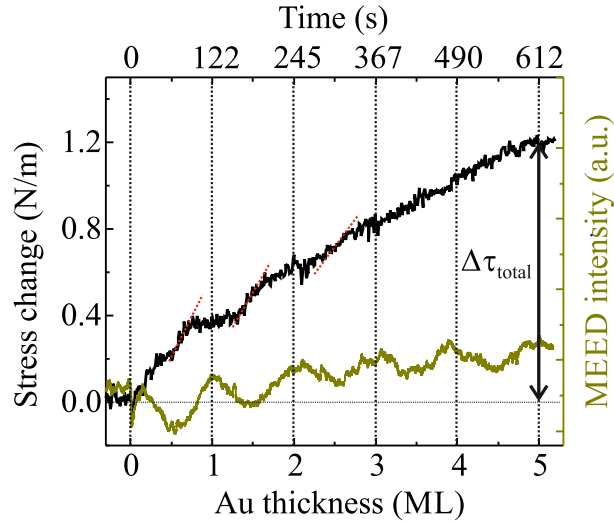
Figure 8.9: Stress change during deposition of Au on Au(001) at 298 K. MEED oscillations are presented in dark yellow, they show pronounced monolayers oscillations. The ML periodicity is independently checked from deposition onto a quartz crystal thickness monitor.

Fe/Au, region III in Fig. 7.1b. The measured tensile stress of +1.8 GPa may tentatively be ascribed to self-diffusion of Au on the reconstructed Au layer. This view does not rely on strain, and we treat the Fe film as being fully epitaxially strained on Au(001). This self-diffusion of deposited Au atoms takes place after the reappearance of the Au-(1×5) reconstructed surface.

In the trilayer Fe/Au/Fe/Au(001) samples, the Au/Fe ratio in the AES results remain constant for all Au thickness. This indicates a constant amount of Au segregated to the surface. The Au spacer layer thickness does not affect the amount of Au floating on top. From Section 8.2.2 we know that at 298 K 0.5 ML Au segregates on top of the 25 ML Fe film.

In conclusion, the results of film stress during preparation of the trilayer system Fe(15 ML)/ Au(X ML)/ Fe(10 ML) on Au(001) offers exciting new insights. Fe in the top layer induces a similar stress as observed for Fe growth on Au(001). The small change of maximum stress at 1.5 ML is ascribed to a change of the substrate surface, from the well ordered bulk Au(001) to the Au film surface. The deposition of Au on Fe/Au(001) was analyzed. The stress curve identifies a compressive stress ≈ -1.1 N/m, and this provides the signature of the formation of the (1×5) surface reconstruction. The stress change during film growth offers a new approach to quantify surface stress changes in reconstruction. This is the first demonstration, where previously

electrochemistry was employed. After the formation of the surface reconstruction, the stress changes to a tensile. This tensile stress is attributed to the diffusion of Au atoms under the Au-(1×5) surface. The tensile stress of +1.8 GPa after 3 ML of Au is comparable to the tensile stress of +1.2 GPa measured for homoepitaxial growth of Au on Au-(1×5) (001). In conclusion, the stress measured during film growth resembles a powerful technique to quantify stress signatures of interdiffusion and surface reconstruction processes.

8.3   Influence of interfacial intermixing on the magnetoelastic coupling of Fe films

In this Section, I discuss the results of the magnetoelastic coupling of Fe films on Ag(001) and Au(001), which were presented in Chapters 5 and 6, respectively. We have seen, in Sections 5.1 and 6.1, that for Fe films on Ag(001) and on Au(001), the surface segregation and interfacial intermixing are present for a distinct range of growth temperature. The change of stress during growth for these systems has been discussed in Sections 8.2.1 and 8.2.2 in view of Fe interdiffusion. Here, we discuss the impact of different deposition temperature on the magnetoelastic coupling. Remarkably, for Fe/Au(001) a corresponding growth temperature effect on the magnetoelastic coupling is not observed, see in Fig. 6.8. The results of the magnetoelastic coupling measurements of Fe/Ag(001) reveal a drastic variation with growth temperature, see Fig. 5.6. I ascribe these changes of ME to the change of the interface structure, which is discussed next.

Fe on Ag(001)

The stress during deposition of Fe on Ag(001) is strongly affected by the growth temperature. We attributed this change to different diffusion-mediated processes. At 200 K the exchange of Fe and Ag is kinetically hindered, and only a reduced interfacial intermixing is expected [56, 163]. In contrast, for depositions at 298 K, the diffusion results in interfacial intermixing and Ag surface segregation.

The film morphologies/intermixing for these two growth temperatures, 200 and 298 K of Fe on Ag(001), are different. This conclusion is supported by the distinct AES ratio results shown in Fig. 5.3b. These changes in morphology may affect magnetoelasticity. The results for B_2 of Fe on Ag(001) were presented in Section 5.2.

The magnetoelastic stress results of films grown at different temperature were shown in Fig. 5.6a. The value of B_2 clearly changes in dependence on the preparation temperature. The film deposited at 298 K shows a large magnetoelastic coupling coefficient B_2 as compared to growth at 200 K.

Modifications on magnetic properties due to the intermixing between Fe and Ag at the interface have been reported [34, 59, 163, 209]. Interfacial intermixing has been proposed to increase the orbital moment of Fe [163]. The orbital moment plays a role for the magnetic-crystalline anisotropy of the system [172, 237]. A magnetic hyperfine splitting into majority- and minority-spin states was also observed due to two distinct Fe interactions (Fe-Fe and Fe-Ag) [34, 59]. This magnetic splitting was enhanced for Fe atoms near the interface.

The variations on the magnetic properties of Fe due to atomic scale proximity to Ag was also investigated for Fe-Ag alloys [210, 214, 215]. Alonso and co-authors [214] reported the impact of Ag atoms near Fe atoms on the magnetic properties of Fe. They used a thin film of Fe-Ag alloy, in a crystalline and amorphous phase. In both phases they found evidence that the Ag atoms were magnetically polarized. These polarized Ag atoms increase the magnetic contribution with increasing intermixing with Fe atoms.

A change in the magnetic moment and/or magnetic-crystalline anisotropy may affect the magnetoelastic coupling, as the magnetoelatic coupling is the strain derivative of the magnetic-crystalline anisotropy [28]. Interestingly, our results show an increase of ME for films grown at higher temperature. We suggest this increase of ME to be related to the increased interfacial intermixing due to high temperature and the resulting modifications of the magnetic properties of Fe.

To gain further insights into the impact of high growth and/or annealing temperature on B_2, identical thermal treatments were performed in both films, Fe/Ag(001) grown at 298 K and at 200 K. The magnetoelastic stress results are shown in Fig. 5.6b. After annealing, both films show a similar magnetoelastic response. A mild annealing up to 343 K during 30 min promotes diffusion in the systems. More Ag atoms are expected to diffuse into the Fe film [154]. The annealing treatment, in my understanding, induces an increased interfacial intermixing in both films (grown at 298 K and 200 K).

A variation of B_2 from 1.3 to 3.3 MJ/m^3 for the film grown at 200 K and from 2.4 to 3.2 MJ/m^3 for the film deposited at 298 K is observed upon annealing, see Fig. 5.6b. This modifications of B_2 upon mild annealing suggests that interfacial intermixing can increase the magnetoelasticity of the Fe films, and Ag segregation seems to have a comparably smaller impact.

The resulting structural and chemical modifications are accessed by Auger and LEED measurements. The LEED measurements before and after an-
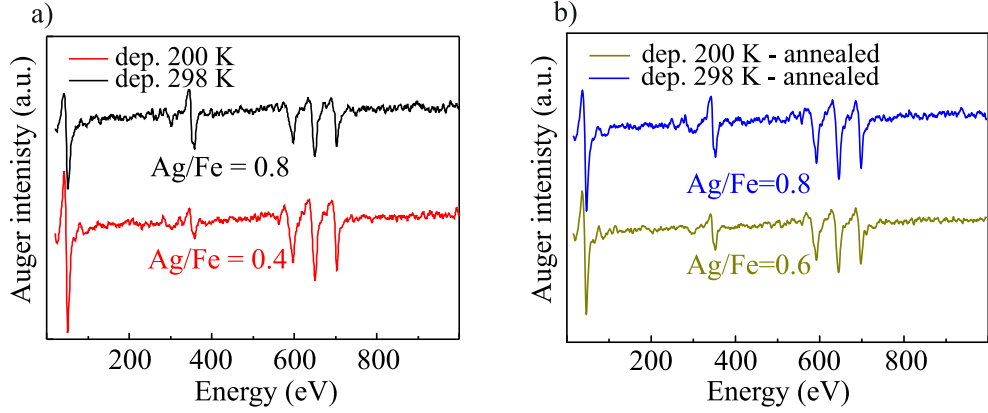
Figure 8.10: a) Auger spectra of Fe(13 ML)/Ag(001) grown at 298 K and 200 K. b) AES of the films after annealing of 30 minutes at 343 K. The as-grown AES have been shown in Fig. 5.3b.The Auger spectra are vertically shifted for sake of visualization.

nealing do not show any significant change and will not be discussed further. However, the AES reveals a considerable change. Figure 8.10a shows AES of the Fe films as-grown, and Fig. 8.10b presents the Auger spectra of the films after annealing.

The AES peak ratio Ag/Fe reveals a significant change for film deposited at 200 K. The change in intensity of the AES peaks indicates a redistribution of Fe and Ag atoms. After annealing the ratio increases for film deposited at 200 K. This suggests a higher Ag content in the Fe film. I assume that the surface morphology does not drastically change upon this mild annealing, as LEED does not present any obvious change. We believe that upon annealing the interfacial intermixing is facilitated for both films. But for the 200 K deposited film, the annealing triggers also the Ag surface segregation. Limited by the annealing temperature, this Ag segregation is quantitatively analyzed by the increased AES ratio, from 0.4 to 0.6. In contrast, the film deposited at 298 K shows no change in the Ag/Fe AES ratio before and after annealing. Even though, the magnetoelastic coupling of both films changed upon annealing, shown in Fig. 5.6b. We ascribe this increase of B_2 to the change of interfacial intermixing due to the induced diffusion upon annealing. This suggests a significant interface effect on the ME rather than a surface influence.

Transition metal alloys, in particular Fe-Ga, have been intensively investigated [11, 12, 14, 18–21, 80–83, 238–241]. Reference [66] investigates the driving force for the large magnetostriction observed in Galfenol (Fe-Ga) us-

108

ing density-functional theory (DFT). The authors found that the change of the magnetostriction of Fe-Ga is enhanced due to a change of the elastic constants. A decrease in the elastic constant C_{44} and in the shear modulus C'' with increasing Ga concentration results from the change of the electronic states [66]. The presence of Ga atoms also change the d-orbitals in the Fe. This contributes more than 70 % to the enhancement of the magnetostriction, in particular from the minority channel, according to Ref. [66].

Therefore, an enhancement in the magnetoelastic coupling due to Fe alloy formation should be taken into account. In the interface region electronic and structural changes in the Fe film due to the intermixing are proposed. We ascribe the modified ME upon annealing to these phenomena.

Fe on Au(001)

In contrast, the magnetoelastic measurements of Fe/Au(001), presented in Section 6.2, reveal no change with growth temperature, see Fig. 6.8. I apply a similar analysis as done for Fe/Ag. For this analysis we recall the film structure results discussed in Section 8.2.2.

The stress during growth of Fe on Au(001) at different growth temperature was shown in Fig. 6.3. In the previous Section 8.2.2, we discussed the change of film structure due to growth temperature. And we conclude that the interfacial intermixing in Fe/Au is a significant process for all growth temperature investigated, $200-375$ K. The variation of the stress was attributed to changes in film roughness and to variations of Au surface segregation.

The interfacial intermixing of Fe/Au(001) has been investigated by LEED, in Ref. [61]. They studied the impact of a post annealing on the interface of Fe/Au. They observed that the interface features did not change with increasing temperature up to 385 K. Based on this finding, we assume that the interfaces of the Fe/Au films for all growth temperature studied in this thesis have a similar degree of intermixing. Thus, my observation of fairly constant ME upon different growth temperature is in line with the result of an unchanged interfacial structure upon annealing.

In conclusion, a variation of growth temperature or annealing of Fe/Ag(001) reveals a drastic impact on the magnetoelasticity of these films. However, this impact is not observed for Fe films on Au(001) under the same thermal conditions. We suggest that a change of the interface intermixing is the main driving force for the modification on the magnetoelastic coupling, and the effect of substrate segregation is comparably weaker. A further contribution may be ascribed to the magnetic susceptibility of Ag atoms in proximity to Fe.

8.4 Ion implantation effects on magnetoelastic coupling of Fe films

In this Section, I discuss the influence of surface modification in the Fe/Au system. The direct influence of Au segregation on ME was investigated with the removal of the top Au layer by sputtering, presented in Chapter 6, Section 6.2. A short sputtering was carried out with different ions. After the removal of the top most layer, the magnetoelastic stress was measured. The results are shown in Fig. 6.9b and c. A trend of the magnitude of the measured B_1 with the mass of the sputtering gas is observed. The removal of the top segregated Au layer may impact B_1 as the interface and its contribution to ME is changed. However, I find that B_1 varies differently for each sputter gas element. Therefore, we follow the hypothesis that the ME change is not given by the removal of Au segregation, rather it may result from the sputtering itself.

Sputtering involves ions, which are accelerated onto the sample. This results in several effects: erosion [181], ion implantation [242], radiation damage [243]. Ion beam sputtering is also used to manipulate the surface morphology [181, 244–247]. Sputtering can either smooth the surface [244] or increase its roughness [181, 245]. The manipulation of the surface morphology by sputtering depends on a set of parameters, such as ion species, ion energy, angle of incidence, ion flux, and sample temperature [181]. The resulting surface morphology modification can impact the magnetic anisotropy by tuning an uniaxial anisotropy [246, 247]. This tuning is achieved by the formation of self-organized periodic patterns upon sputtering under an incident angle of 80° with respect to the surface normal [246, 247]. Our experiments are performed with an incident angle normal to the surface, and no tuning of uniaxial anisotropy is expected, and it was not observed. This rules out the possibility of the formation of self-organized surface patterns upon sputtering.

Sputtering leads to the removal of the topmost layers, as evidenced by AES in Fig. 6.9a, but it also leads to increased surface roughness and ion implantation. Even though no evidences of ion implantation is observed in AES. The implantation of noble gas ions is usually regarded as small. However, the influence of implanted ions of noble gas on the sputtering yield has been reported before [242, 248, 249]. The density and depth of the ion implantation on the surface depends on the ratio of ion-to-target mass. An analytical model for ion implantation and removal is used in Ref. [183]. These authors investigated the stress during sputtering of a Cu(100) single crystal with Ar, Ne, and He. They conclude that the implantation depth of He

Table 8.6: Atomic mass of the noble gases used in this work for sputtering, and the mass ratio in relation to Fe. All masses were extracted from Ref. [251].

Property	Helium	Neon	Argon	Krypton	Xenon
Atomic mass (amu)	4.00	20.18	39.95	83.80	131.29
M_{ion}/M_{Fe}	0.07	0.361	0.715	1.500	2.351

is one order of magnitude larger than for Ar, and Ne. It is approximately 10 nm for He at E_{He} of 2200 eV [183]. This indicates a larger number of He ions implanted over a region. They also measured the stress during the sputtering process, and found that Ne and He gives a stress 3 times larger than Ar, from 20 N/m for Ne and He, and 5 N/m for Ar [183]. They relate this to the smaller surface damage by Ar-sputtering. However, there is no clear explanation for the origin of the stress during sputtering. The stress could be related to the pressure induced by the implanted gas atoms, or due to ion radiation damage [250].

Mutzke and co-authors [249] calculate the ion implantation depth of He, Ne, Ar, and Xe in Si. They observed that there is a strong influence of the mass ratio of the involved elements. They compare the damage in the surface for each sputtering gas. And they conclude that for a heavy element such as Xe, sputtered onto a target with a mass smaller than Xe, gives rise to a reduced depth of implantation and an increased surface damage, as compared to a light sputtering element. Therefore, sputtering with a light incident element onto a heavy target results in a deeper ion implantation with reduced damage in the surface area. The same result is found for He, Ar, and Xe on Mo or W, discussed in Ref. [180].

Therefore, the ratio M_{ion}/M_{target} determines the resulting process on the surface upon sputtering. Table 8.6 shows the atomic mass of each noble gas and the mass ratio of each element with respect to the target mass ($M_{Fe} = 55.84$ amu).

We conclude that He, Ne, and Ar sputtering of Fe corresponds to a light incident element sputtered onto a heavy target ($M_{ion}/M_{target} < 0$). This will increase the depth of ion implantation and decreases the damage near the surface. However, for Kr and Xe the situation is inverse, $M_{ion}/M_{target} > 0$. In this case, the depth of implantation ions will be reduced, but the recoil scattering is increased. This indicates that the surface region will be more damaged, and the impact on the inner Fe layers is expected to be smaller. From our magnetoelastic coupling results, in Fig. 6.9b and c, we observe, indeed, a distinct difference for sputtering with heavy and light elements. We have observed that after sputtering by light ions the magnetoelasticity

111

increases. We assign this result to the presence of implanted ions, which also increase the strain in the film lattice. On the other side, the magnitude of magnetoelastic coupling after sputtering with heavy elements is decreased. This is ascribed to the surface damage. The sputtering leaves craters on the surface. This allows atoms to relax, and an induced ME stress is not fully transferred to the substrate.

These results shed first light on the importance of the sputtereing-induced modified surface structure on the magnetoelastic coupling. The impact of the submonolayer amount of segregated Au floating on top is comparably weak. The destructive aspect of the sputtering gives rise to several side effects. The mass ratio gives a good qualitative estimate for the resulting quality of the sputtered surface. An ion implantation is proposed to drive the change in ME by sputtering with light elements. Surface damage by sputtering with heavy ions reduces the magnitude of the magnetoelastic coupling due to an incomplete stress transfer to the substrate.

8.5   Film thickness dependence of the magnetoelastic coupling

In this Section I discuss the main results of the magnetoelastic coupling for Fe films at different thickness ($6-30$ ML). The results are presented in Section 5.2 and Section 6.2, for Fe films on Ag and Au(001), respectively. A most striking result is that the magnetoelastic coupling measurements of Fe films on Ag(001) reveal a novel, previously not reported, oscillatory behavior of the magnetoelastic coupling B_2 with increasing Fe thickness, as shown in Fig. 5.5. We ascribe this to the influence of QWS in the Fe films. In contrast, my results for Fe films on Au(001) do not show a comparable oscillatory behavior. Rather, the data suggest a dependence on film strain, see Fig. 6.7.

In Fe(15 ML)/ Au(X ML)/ Fe(10 ML)/ Au(001) films we observe an oscillatory variation of B_1 upon varying the Au thickness, see Fig. 7.4. The oscillation period correspond to that of the interlayer exchange coupling (IEC) mediated by Au [97,104–106]. The oscillatory variation of the magnetoelastic coupling is ascribed to QWS in Au, which impacts on the electronic states of Fe/Au/Fe near the Fermi energy.

Fe on Au(001)

The thickness dependent magnetoelastic coupling B_1 of Fe/Au(001) is presented in Chapter 6, Section 6.2. The change of B_1 with increasing Fe thickness is shown in Fig. 6.7 as a function of film strain. We describe the apparent thickness dependence of B_1 to a strain-dependent correction of B_1^{eff}, as presented in Section 2.2 ($B_1^{eff} = B_1 + D\epsilon$) [26, 51, 143].

As described in Section 6.2, the results can be separated into two regions. Region I displays a linear increase with increasing film strain, as indicated by the linear fit (red dashed line). The slope of the dashed curve gives $D = 11.1 \pm 1$ MJ/m^3 and the curve intercept the y-axis at $\epsilon = 0$ at $B_1 = -3$ MJ/m^3.

Magnetoelastic coupling of Fe thin films has been investigated before on different substrates [22, 26, 252]. In Fe on Ir(001) [26] the authors found a linear relation of B_1 with film strain as $B_1^{eff} = -3.6$ MJ/m^3+155ϵ. However, no linear dependence of strain was found for B_2. They conclude that this approach gives a reasonable description of experimental observation only in some cases. The failure of the phenomenological description of the data could be related to the adopted strain analysis [26]. The film strain calculated from the stress measurements neglects a possible spatial variation throughout the film volume. This consideration of film strain worked well for ultrathin films, but it is not precise for thicker films [51].

An incomplete description of the magnetoelastic coupling of thin films by this strain-dependent correction was also observed for Fe on W(001). In the Fe/W [252] system, B_1 has been measured. A peculiar behavior was found, the variation of the value of B_1 can also be separated into two regions. B_1 shows a change of sign, from negative to positive, with increasing film strain. A linear dependence of B_1 was observed mainly for small strain, with strain below 0.6%. The linear fit between B_1 and ϵ in the low strain region results in $B_1^{eff} = -1.2$ MJ/m^3+200ϵ [252].

The strain-dependent B_1^{eff} of Fe films on different substrates can be compared. From the linear fit in Region I, see Fig. 6.7, the coefficient B_1 is obtained as -3 MJ/m^3. This value of B_1 is between the values obtained for Fe films on Ir(001) and W(001), -3.6 and -1.2 MJ/m^3, respectively [26, 252]. However, the coefficient D was found an order of magnitude smaller. Fe/Au(001) shows $D = 11.1 \pm 1$ MJ/m^3, in comparison with Fe/Ir, and Fe/W of $D = 155$ MJ/m^3 [26], and 200 MJ/m^3 [252], respectively. Fe/MgO(001) [22] showed also a huge difference of D as compared to Fe/W or Fe/Ir. The value of the D for Fe on MgO was found to be 1100 MJ/m^3, summarized in [26]. The deviations observed for D, where addressed in Ref. [26], and attributed to the different response of magnetoelastic coupling

to varying magnitudes of strain.

The value of D indicates how B_1^{eff} changes upon variations of film strain. D with 2-3 orders of magnitude larger than B_1 reveals a pronounced variation of B_1^{eff} upon small changes of strain. For Fe/Au the small magnitude of D suggests a minor variation of B_1^{eff} with strain. Specificities of the film growth, such as misfit dislocations for thicker film, relaxation process due to the growth mode, and intermixing at the interface should be taken into account to obtain the definitive reason for the difference of strain dependence of B_1^{eff}. This calls also for a more sophisticated way to analyze the strain of the film.

Our experimental data for strain larger than 0.3%, shown in region II in Fig. 6.7, shows an almost constant B_1 of -1.3 ± 0.4 MJ/m^3. The reference bulk Fe has a value of $B_1 = -3.4$ MJ/m^3. A break of the linear strain dependence of B_1 for larger strains has been observed in Fe/W [252] and Fe/MgO [22]. They attributed the failure of the phenomenological model to experimental and/or physical based effects, such as roughness, change in magnetization, and surface and interface effects [22]. Note, the magnetoelastic coupling of Fe on Au(001) is found to deviate from the bulk bcc Fe value even for a 30 ML thick film.

Recently, a study investigated the impact of variation of applied magnetic field on the electronic states of Fe/Au(001) [253]. The change in the electronic states was investigated upon different magnetization directions by angle-resolved photoemission spectroscopy (ARPES). The authors found a change in the bulk electronic bands by switching the applied magnetic field direction. They attributed this to changes of bulk electronic bands, as an effect of the symmetry breaking at the surface [253]. This points at the role of the surfaces and interfaces on the magnetic anisotropy of thin films. This finding speaks in favor of the different magnetoelastic coupling coefficient for Fe bulk and the observed values for Fe thin films on Au(001).

In conclusion, for films of Fe on Au(001) with low strain the phenomenological correction of strain-dependent B_1 can be applied successfully. The linear relation shows a weak relation of strain and B_1^{eff} due to the small value of the coefficient D, as compared with other systems. This linear relation changes to a constant B_1 for films with large strain. The deviation of experimental results from the linear correction model indicates the limitations of this phenomenological approach. Systems of multilayers, grains, and even thin films present a distinctly more complicated correlation between strain and magnetoelasticity [23, 26, 254]. This implies that more factors than only film strain need to be considered. Quantum well states are another factor, and this is discussed next.

Fe on Ag(001)

Fe/Ag(001) shows no linear dependence of B_2 with film strain, see Fig. 5.5a. Rather, an oscillatory non-monotonic variation of B_2 is observed with increasing Fe thickness, see Fig. 5.5b. Here, I discuss how quantum well states may induce a distinct variation of the magnetic properties of the Fe film.

Quantum confinement in ferromagnetic layers, like Co/Cu, Co/Pd and Fe/Ag has been reported before [10, 103, 168–171]. Electron confinement along the film thickness impacts the magnetic-crystalline anisotropy of these systems [168, 172]. However, the implication for magnetoelasticity has been not studied before. It is a novel result. Now, I present the analysis of Fe/Ag(001) in view of quantum well states in the Fe layer. I measured the magnetoelastic coefficient B_2 of Fe films independence of Fe film thickness, as presented in Chapter 5.

Figure 5.5a shows B_2 in dependence of film strain. A random scattering of data points is observed. This suggests that the phenomenological model of a strain correction of B_2 is not applicable. In Fig. 5.5b we do observe a thickness-dependence of B_2. The magnetoelastic coefficient B_2 of Fe on Ag(001) shows an oscillatory variation with Fe thickness.

An oscillatory magnetic-crystalline anisotropy variation has been observed for ferromagnetic thin films with increasing film thickness. It has been ascribed to the influence of quantum confinement in the films on magnetic anisotropy [103, 168, 169, 171, 255–257].

In view of these findings it is reasonable that the magnetoelastic coupling also varies in an oscillatory manner with increasing Fe thickness. The results of B_2 can be fitted by a periodic function. The red dashed line, presented in Fig. 8.11, shows such a fit. The fit gives an oscillation period of 10.3±0.4 ML.

The direct comparison of magnetic anisotropy variations induced by QWS in Fe on Ag, Ref. [103], reveals that the period of $\approx$10 ML is almost double of the period observed for the magnetic-crystalline anisotropy, which was reported as 5.5 ML [103]. The authors used several techniques to support that the oscillatory behavior of MA is induced by QWS in the ferromagnetic film. They found a period of 4.5 ML for the spin polarization of the QWS by spin-resolved photoemission spectroscopy (PES), comparable to the 5.5 ML period of the magnetic-crystalline anisotropy measurements obtained by MOKE, and 4 ML for the in-plane orbital moment observed in the X-ray magnetic circular dichroism (XMCD) measurements.

The factor of two between the periodicity found in magnetoelastic coupling and magnetic-crystalline anisotropy is surprising at first sight. It could be an effect of the sample preparation.

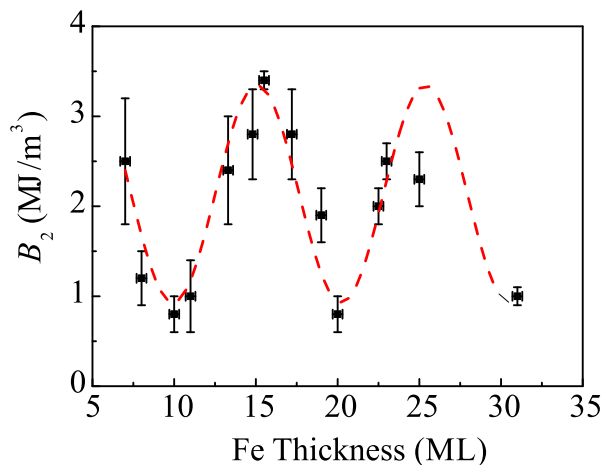The Fe film in Ref. [103] were prepared by deposition at room temperature

Figure 8.11: Magnetoelastic coupling coefficient B_2 as a function of Fe thickness on Ag(001). The red dashed line is a fit by $B_2 = A + B sin(k \cdot t_{\text{Fe}} + \varphi)$, with $A = 2.137$, $B = -1.204$, $k = 0.610$, and $\varphi = -10.77$. The period extracted from this fit is 10.3 ± 0.4 ML Fe.

and measured at 5 K. In order to obtain a flat film the authors improved the film quality by a post-deposition annealing at 500 K. In contrast, my samples were deposited at 298 K with no post-deposition annealing. The higher temperature has not been applied to avoid increasing interfacial intermixing. Section 8.3 showed that annealing induces significant changes of the film structure, where interfacial intermixing increases.

As discussed in Section 8.3, the intermixing between Fe and Ag at the interface can modify the magnetic properties of Fe [34,59,163,209]. The intermixing results in distinct Fe interactions (Fe-Fe and Fe-Ag) [34,59], which can change the orbital moment of Fe [163] and impact Ag atoms to become magnetically polarized [210, 214, 215]. At higher temperature ($T_s \geq 450$ K) the diffusion results in a dissolution of Fe in the bulk of the Ag crystal [153–156]. Therefore, the annealing at such higher temperature as 500 K could strongly affect the magnetic properties of the Fe film. As magnetoelastic coupling is seriously affected by the change of interface of the epitaxial film, the "alloy" formed by the increased temperature could affect the magnetoelastic response, as seen for Fe-Ga alloys and discussed in Section 8.3.

The roughness of the film is also a matter to be taken into consideration. The growth of Fe on Ag at 298 K gives rise to a relative rough surface due to the SK growth mode. Our film is likely to have imperfections such as atomic steps or layer thickness fluctuations.

Therefore, the direct comparison of the oscillations observed in ME with

116

the oscillations of MA from Ref. [103] is not correct qualitatively. A necessary condition for a meaningful comparison is that the sample should be prepared under the same conditions. However, it is conceivable that QWS in the Fe layer affect the magnetic properties of the film. The period of oscillation of ME presented here differs from the period observed in previous measurements on different properties of different prepared samples. Remarkably, for Fe films on Au(001) I find no indications of an oscillaroty variation of ME with Fe thickness. Possibly, a weak influence of QWS in Fe layers on the ME in Fe/Au is suppressed by the influence of film strain in this case.

Further experiments are require to identify the origin of the difference in the oscillatory period of $B - 2$ in Fe/Ag(001). The behavior of the ME of Fe/Ag(001) upon higher annealing tempereture should be investigated for further insights.

Fe(15 ML)/Au(X ML)/Fe(10 ML) on Au(001)

A strong influence of electronic confinement on magnetic properties has been observed in trilayers, superlattices, and multilayers of FM/NM/FM systems [258, 259]. An oscillatory interlayer exchange coupling (IEC) upon increasing the non-magnetic layer thickness was attributed to a spin-polarized confinement effect in the NM layer [7, 8, 34, 89, 91, 92, 100, 102, 114, 184, 224, 260–263]. Other magnetic properties also show an oscillatory behavior with increasing spacer thickness, such as the anisotropic magnetoresistence [91, 264], magneto-optical anisotropy [9, 44–46], local magnetic polarization [256, 265], and magnetic-crystalline anisotropy [10, 47, 141, 170, 266].

The trilayer system Fe/Au/Fe on Au(001) is a promising candidate to investigate the impact of electronic confinement on magnetoelastic coupling. This system shows a well-studied oscillatory IEC, and its impact on magnetoelastic coupling needs to be explored. The oscillatory IEC leads to a variation of relative magnetization direction of the two Fe films, which are separated by Au. A variation from parallel to antiparallel in-plane magnetic alignment of the ferromagnetic layers is observed at room temperature upon variation of the Au thickness [97, 104–106]. A long and short periodicity of 8 and 2 ML of Au [97], respectively, were experimentally found.

The antiparallel magnetization configuration of the Fe layers yields a different response in magneto-optical Kerr effect (MOKE) measurements. At a distinct Fe thickness two distinct saturation magnetic fields are observed. These two saturation fields are expected due to the antiparallel magnetization configuration [186]. An example of MOKE in the antiparallel alignment was shown in Fig. 7.3. In this case, the Fe layers achieve a parallel configuration for a higher applied magnetic field. This result confirms the presence of

117

an antiparallel magnetization alignment. By contrast, the parallel alignment was identified by a single square hysteresis loop and a single saturation field.

The modifications of the magnetic configurations of the Fe films due to QWS in the Au layers were discussed before [89, 102]. The period of the oscillations of the QWS depends on the Fermi surface of Au(001). The Fermi surface of a noble metal is presented in Chapter 2.

The period Λ is directly related to the wave vector of the confined electronic state. It is determined as $\Lambda = 2\pi/ak_{\mathrm{env}}$, where a is the lattice constant and k_{env} is the wave vector spanning the crossing point of the electronic band at a given energy and the nearest high-symmetry point of the Brillouin zone (BZ). A multiperiodic oscillation is expected due to the shape of the Fermi surface. The high symmetry planes of Au(001) give rise to two contributions from the edges of the s,p band to the Fermi surface ("dog bone" shape) [9,34], see Fig. 2.5.

As described in Chapter 2, the wave vector k_{env} for the (100) orientation is $(k_{\mathrm{ZB}} - k_{\mathrm{F}})$, where k_{F} is the Fermi wave vector and k_{ZB} is the wave vector at the Brillouin zone boundary ($k_{\mathrm{ZB}} = 2\pi/a$). One cross section of the Fermi surface of Au fcc is with the k_{env} at $\mathbf{k}_{||} = 0$ and $E = E_{\mathrm{F}}$, named k_1. The calculated result of Au(001) is $k_1 = 0.76k_{\mathrm{ZB}}$ [102], for which a long period of 8.3 ML is predicted. The second period is a contribution from the states near the end of the "dog bone" shaped Fermi surface. This larger $\mathbf{k}_{||}$ results in a $k_2 = 2.54k_{\mathrm{ZB}}$ [102], and a short period of 2.5 ML is predicted.

The results of magnetoelastic coupling measurements of Fe/Au/Fe trilayers were presented in Fig. 7.4. The results of the magnetoelastic coupling coefficient B_1 show an oscillatory behavior with a period of approximately 2 ML Au. Here, I advance the analysis to quantitatively extract the periodicities involved. The data of B_1 for Au thicker than 2 ML is fitted by a function with two periodicities. The best fit is presented in Fig. 8.12. The idea of two periodicities comes from the multiperiod obtained for QWS in Au(001) [89]. Therefore, from the best fit, see in Fig. 8.12, the long and short periods of the ME measurements are extracted. The short period is 2.18±0.03 ML and the long period is 8.2±0.9 ML. These periodicities agree with the expectations from the analysis of the Fermi surface characteristics.

Structural changes are ruled out as driving force of these oscillations. Another point to consider is pointed out by Refs. [267,268]. The roughness at the interface of trilayers and multilayers plays an important role for the magnetoelasticity. However, we have no indications that the quality of the interface changes with increasing Au thickness. This statement is corroborated by the stress measurements during growth. The stress curves in Fig. 7.4a have the same slopes, with a peak at 1.5 ML Fe, which varies only little in magnitude by 0.084 N/m for the complete range of Au thickness (1-12 ML). This small
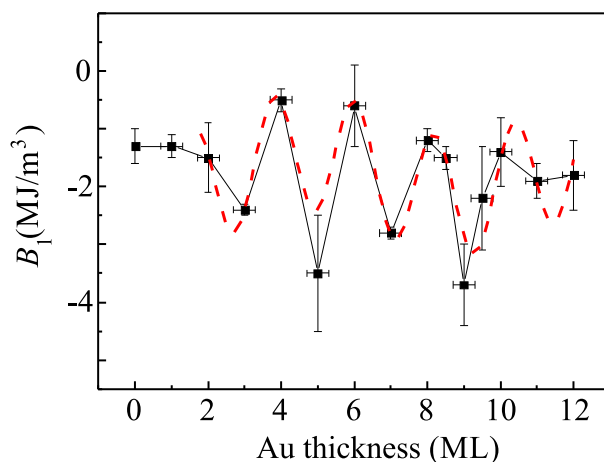
Figure 8.12: Magnetoelastic coupling coefficient B_1 as a function of Au thickness on Fe(15 ML)/ Au(X ML)/ Fe(10 ML) on Au(001). The red dashed line is the best fit for the function, by $B_1 = A + B sin(k_1 \cdot t_{Au} + \varphi_1) + C sin(k_2 \cdot t_{Au} + \varphi_2)$, with $A = -1.762$, $B = 1.034$, $k_2 = 2.874$, and $\varphi_2 = 3.156$, $C = -0.390$, $k_1 = 0.764$, and $\varphi_1 = 19.938$. The long and short period are extracted from k_1 and k_2 as 8.2 ± 0.9 and 2.18 ± 0.03 ML of Au, respectively.

stress change appears to be insufficient to suspect a significant change of the interface. An oscillatory magnetic anisotropy has been observed on Cu/Co system in Ref. [141] due to incomplete Cu layer. The influence of the incomplete layer gives rise to an oscillations with a period of 1 ML, which is not observed in our data.

The periodicity obtained from the ME measurements is consistent with the periods obtained for the interlayer exchange coupling of the same system [34, 89, 97, 102, 104–106, 184, 269].

The consistency between magnetoelastic coupling results and the IEC periodicity suggests a strong link between these two properties. The IEC is described by bilinear (J_1) and biquadratic terms (J_2), which determine the strength of the coupling. J_1 is responsible for a collinear coupling, J_2 favors perpendicular coupling. The latter term is normally much smaller. It is responsible for small deviations from collinear configurations, and this impacts magnetic anisotropy. I review the origins of effect next.

Disorder in the films, such as thickness fluctuation, pin-hole coupling, loose spins, and magnetostatic coupling, gives rise to a slight rotation of the magnetization of the films. In the phenomenological picture described above, J_2 is responsible for this rotation [7, 97, 98, 109–113, 269–272]. An oscillatory behavior of J_2 has been reported and predicted in several systems, Fe/Cu/Fe,

Fe/Cr/Fe, Fe/Au/Fe, Fe/Al/Fe, Fe/Ag/Fe [110–114]. Theoretically [112], an intrinsic J_2 is expected to oscillate with the non-magnetic spacer layer thickness. These oscillations of J_2 turn out to be incommensurate with the oscillations of the bilinear term J_1, and J_2 only dominates in the nodes of J_1 [112]. However, this is not observed in our case. An external disorder could be the reason for a contribution by J_2 in our system. Magnetostatic coupling disorder was observed in the Fe/Au sandwiches in Ref. [109]. This effect is observed for rough interfaces. The appearance of magnetic dipoles on a rough interface may increase the strength of the J_2 term. However, it fails to describe a concise oscillation with J_1 like what is found in my results on B_1.

The magnetoelastic coupling may also be affected by a change of magnetic-crystalline anisotropy. The link between the two is obvious from the definition of ME as the strain derivative of magnetic-crystalline anisotropy [28, 51]. In order to investigate the link between ME and MA, I performed MOKE experiments to obtain the magnetic-crystalline anisotropy constant K by inducing an uniaxial anisotropy, see Fig. 7.5. Here, I create an uniaxial anisotropy by applying a constant external magnetic field perpendicular to the sweeping magnetic field in the LMOKE geometry.

Indeed, the results of magnetic-crystalline anisotropy K, presented in Section 7.2 Fig. 7.5b, reveal a non-monotonic behavior as a function of Au thickness. This result corroborates that the influence of the electronic modifications impacts the magnetic anisotropy, and consequently, the magnetoelastic coupling. Figure 7.5b depicted the direct comparison of K and the magnitude of B. We see that the oscillatory behavior observed on the magnetic-crystalline anisotropy constant is in phase with the oscillations of magnetoelastic coupling coefficient B_1.

The driving force behind both variations, ME and MA, may be the QWS, which change the electronic density of states of the non-magnetic layer. This impacts the magnetic anisotropy due to SOC [237]. Electronic confinement leads to discrete energy levels in the electronic density of states. These energy levels of QWS modulate the electronic density of states near the Fermi level. The interlayer exchange coupling is governed by the electronic states at the Fermi surface. On the other hand, the magnetic anisotropy is generally determined by the electronic states of the entire Brillouin zone. Therefore, the hybridization of the electronic states at the interface plays the role of polarizing the bands accordingly, and this impacts the magnetic anisotropy. From a careful inspection of the Kerr effect in a paramagnetic overlayer Bruno and co-authors [9] noticed a spin-dependend electron reflectivity at the NM/FM interface. In the case of the Au/Fe interface the authors conclude that the reflections at the interface has a significant contributions from the

$\bar{\Gamma}$ and $\bar{M}$ high symmetry points in the 2-D Brillouin zone [9].

Fe/Cu/Fe and Co/Cu/Co also reveal an oscillatory magnetic anisotropy with increasing the non-magnetic spacer layer (Cu film) [47]. The authors conclude that the magnetic-crystalline anisotropy oscillations arise in small regions in the 2-D Brillouin zone which QWS cross Fermi energy. In this case, the period of MA oscillations shows identical value in both systems, because the confinement in Cu matters. The maximum impact on MA is observed for a thickness, at which QWS cross the Fermi level. This impact on the MA results from spin-orbit coupling, which is mediated by the QWS-driven change in the electronic states. The period agrees with period observed for Cu QWS [273] and IEC of Co/Cu/Co [92]. This suggests oscillation of IEC and MA with a constant phase relation due to QWS in the non-magnetic layer.

Magnetoelastic coupling and magnetic-crystalline anisotropy have a common origin, namely spin-orbit coupling. We suggest that the observed modulation of MA is due to QWS in the Au layers. Consequently, a strong thickness-dependence of ME in the trilayer Fe/Au/Fe is observed. The oscillatory variation of ME B_1 agrees impressively with the periodicity of IEC. My results suggests strongly that both phenomena are driven by QWS.

To conclude this Section, the magnetoelastic coupling results of Fe/Au(001) show a linear dependence on film strain. A comparable dependence is not observed for Fe/Ag(001). In contrast, the magnetoelastic coupling of Fe on Ag(001) exhibits an oscillatory-like behavior with increasing Fe film thickness. An oscillatory variation of magnetoelasticity of Fe/Au/Fe trilayers with increasing Au thickness is observed. The reason for this novel finding of an oscillatory variation of ME are QWS in the Au layers. In the Fe/Ag system, the electron confinement in the Fe layer changes the electronic states with Fe thickness, which may contribute to the oscillatory variation of B_2. However, in the epitaxial FM/NM/FM trilayer system, the electrons are confined in the non-magnetic layer. Thus, here, the oscillatory ME is due to electron confinement in Au. The origin of the influence of QWS on MA and ME is proposed to be via SOC through the hybridization at the interfaces.

Chapter 9

Conclusions and outlook

The main topic of this thesis is the investigation of the relation between atomic and electronic structure for the magnetic properties of epitaxial thin films. The central experimental technique is an optical bending beam method, which has a high sensitivity on the sub-monolayer coverage regime to measure stress. The measurement of the stress change through a bending cantilever is a powerful technique to study structural changes in corroboration with complementary AES and LEED experiments. I use this technique also to investigate the magnetoelasticity of Fe films and Fe/Au/Fe trilayers on Ag(001) and Au(001). Here, we advance the understanding of the underlying physics. My results identify the role of quantum well states for a modified magnetoelastic coupling.

In this thesis, I reveal the first stress measurements during deposition of Fe on a layered topological insulator (TI). Deposition of Fe on Bi_2Se_3 was investigated by stress measurements for different growth temperature. Our results present a clear indication of the limitations of the role of stress change due to epitaxial strain in orthorhombic FeSe. We found that the growth is dominated by thermal assisted formation of α-FeSe-like nanocrystals on $Bi_2Se_3(0001)$. This gives arise to a characteristic compressive stress of -23 GPa, in contrast to the calculated misfit stress of $+0.94$ GPa. Furthermore, our structural analysis indicates the replacement of Bi with Fe even at low temperature [189]. We found that upon deposition of Fe a substantial structural disorder is induced. We assign this to atomic replacement. The surface order is, then, reestablished upon thermal treatment, either by annealing or higher growth temperature, and this leads to the formation of the FeSe nanocrystals. The FeSe nanocrystals grow in three rotational domains [63]. From a quantitative analysis of the stress results we conclude that the stress observed during Fe growth results from structural and atomic rearrangements rather than from epitaxial misfit strain.

I also investigate the stress during deposition of Fe atomic layers on Ag(001) and Au(001). Our stress measurements identify different modes of interface formation during Fe growth, which affect the film morphology. With complementary structural analysis we characterize the structure of the Fe films on Ag and Au for each growth temperature presented in this thesis. Measurements at different growth temperature provide new insights into the interdiffusion process, and its impact on growth mode, interfacial intermixing, surface segregation, and the impact on film stress.

The temperature-dependent stress measurements identify different processes in both systems. The morphology of the Fe film on Ag(001) shows a drastic influence of temperature on the interface formation, and on the magnetoelasticity. This difference is attributed to the change of the elemental distribution near the interface with temperature. In the case of Fe on Au(001), the influence of growth temperature is comparably smaller. The most pronounced finding is here, as the growth temperature is reduced, the relative amount of substrate segregation on top of Fe film decreases. From the analyses of the stress measurements made in this thesis we could provide an advanced understanding of interfacial atomic exchange processes for stress and magnetic properties.

Another significant aspect of this work is the stress involved in the lifting and formation of the Au surface reconstruction. Au(001) presents a well known (1×5) surface reconstruction. My thesis provides the first data on the correlation between lifting a surface reconstructions and corresponding surface stress change. Furthermore, the stress change during formation of its reconstruction is also presented. The stress results during growth of Au on the strained Fe film on Au(001) allowed to quantify the surface stress involved in the formation of a surface reconstruction. Our results present the first stress data on Au surface reconstruction under clean ultra high vacuum conditions. The reconstruction of Au induces a compressive stress change of -1.1 N/m, which is comparable to the calculated stress of -1.79 N/m [50].

Our magnetoelastic stress measurements of Fe/Au(001) show that the magnetoelastic coupling coefficient (B_1) can be ascribed to a strain-dependence for epitaxial strained films [22, 26, 252]. Our results also reveal that the magnetoelasticity is independent of the growth temperature for this system. This indicates that the magnetoelastic properties here are not governed by interface effects. The impact on ME due to a submonolayer coverage of segregated Au floating on top is comparably week. This result was confirmed by removing Au by sputtering the top layer of the Fe film. I find that sputtering gives rise to several side effects. A clear dependence of the magnetoelastic coupling on the mass of the sputter ion is observed. These novel results shed light on the importance of the modified surface and bulk structure on the magne-

toelasticity properties. Systematic studies are called for to obtain the critical temperature where the intermixing at the interface is drastically reduced in order to observe the impact of the interface on ME for this system. The magnetoelastic coupling coefficient B_2 of Fe on Ag(001), on the other hand, shows an increase of the magnitude with increasing growth temperature. Our results suggest that a change of the interface intermixing is the driving force for the modification on the magnetoelastic coupling, and the surface segregation does not play a fundamental role for the magnetic properties of the Fe film. A secondary contribution to the magnetic response may come from the induced magnetization of Ag atoms in proximity to Fe [210, 214, 215].

The main results of my thesis are related to the impact of changes of the electronic structure on the magnetoelasticity. It is known that electron confinement strongly influences the magnetic properties of thin films, super-lattices, and multilayers systems [258, 259]. However, up to now the effect on magnetoelasticity has not been identified yet.

I find an oscillatory variation of the magnetoelastic coupling coefficient B_2 with increasing Fe thickness on Ag(001). This suggests that QWS impact the magnetoelastic coupling of thin films significantly. The B_1 oscillations are ascribed to the formation of QWS in the Fe film. Theory-based insights into the understanding physics are called for.

Based on the influence of QWS on the ME, I exploit the prototypical tri-layer system Fe(15 ML)/ Au(X ML)/ Fe(10 ML) on Au(001) as a platform to study the link between the modified electronic states and the magnetoelastic property. This system shows a well-studied interlayer exchange coupling (IEC), characterized by an oscillatory behavior of the coupling of the fer-romagnetic Fe layers upon increasing the nonmagnetic Au layer thickness. These oscillations have been attributed to a spin-polarized QWS in the NM layer [7, 8, 34, 89, 91, 92, 100, 102, 114, 184, 224, 260–263]. The here presented effect of QWS on magnetoelasticity is a novel physical phenomenon to be taken into account for magnetoelastic coupling in ultra thin films.

The results of magnetoelastic stress on the trilayer system, Fe(15 ML)/ Au(X ML)/ Fe(10 ML) on Au(001), identify the interplay between QWS and ME of thin films. In the magnetoelastic stress we observe an oscillatory variation of B_1 upon varying the Au thickness. The oscillation periods obtained for B_1 correspond to that observed for IEC [97, 104–106], and are measured as 2.1 ML and 8.2 ML. The excellent agreement of the periodicity suggests strongly that the two properties, IEC and ME, are driven by a common origin. We have confirmed this result by comparing the magnetic-crystalline anisotropy K obtained by MOKE. We found that K oscillates with increasing Au thickness, in-phase with B_1. These results indicate that the QWS in the Au layer impacts ME and MA. Our work presents a novel mechanism

that can be used to tune the magnetoelaticity of thin films through control of QWS-modulated electronic states. Following the idea of this study, investigations of the ME of more systems where QWS have strong influence on the magnetic anisotropy appear promising. With the help of theory a new model to describe the magnetielasticity of thin films may be proposed, which considers the impact of QWS on ME.

Finally, many experimental aspects of film structure and magnetic properties have been addressed. Thanks to the stress measurements a reliable characterization of growth processes is possible. Interdiffusion, change of growth mode, and surface reconstruction are identified by stress measurements. A novel effect on the ME is presented for the prototypical system of Fe/Au/Fe. The results of this thesis suggest the modulation of the magnetoelastic coefficient B_1 by the QWS on the spacer layer Au. These novel results advance the understanding of modified magnetoelastic effects in thin films.

Bibliography

[1] E. Menéndez, M. O. Liedke, J. Fassbender, T. Gemming, A. Weber, L. J. Heyderman, K. V. Rao, S. C. Deevi, S. S. nach, M. D. Baró, J. Sort, and J. Nogués, "Direct magnetic patterning due to the generation of ferromagnetism by selective ion irradiation of paramagnetic FeAl alloys," *Small*, vol. 5, no. 2, pp. 229–234, 2009.

[2] P. Grünberg, R. Schreiber, Y. Pang, M. B. Brodsky, and H. Sowers, "Layered magnetic structures: Evidence for antiferromagnetic coupling of Fe layers across Cr interlayers," *Phys. Rev. Lett.*, vol. 57, pp. 2442–2445, Nov 1986.

[3] Y. Shiota, T. Nozaki, F. Bonell, S. Murakami, T. Shinjo, and Y. Suzuki, "Induction of coherent magnetization switching in a few atomic layers of FeCo using voltage pulses," *Nature Materials*, vol. 11, pp. 39–43, 2012.

[4] S. S. P. Parkin, M. Hayashi, and L. Thomas, "Magnetic domain-wall racetrack memory," *Science*, vol. 320, no. 5873, pp. 190–194, 2008.

[5] S. Bader, "Magnetism in low dimensionality," *Surface Science*, vol. 500, no. 1, pp. 172 – 188, 2002.

[6] S. Blügel and G. Bihlmayer, *Handbook of Magnetism and Advanced Magnetic Materials: Magnetism of Low-dimensional Systems: Theory.* John Wiley and Sons, Inc., 2007.

[7] S. Blizak, G. Bihlmayer, S. Blügel, and S. E. H. Abaidia, "Interlayer exchange coupling between FeCo and Co ultrathin films through Rh(001) spacers," *Phys. Rev. B*, vol. 91, p. 014408, Jan 2015.

[8] C.-H. Chang, K.-P.Dou, Y.-C. Chen, T.-M.Hong, and C.-C. Kaun, "Engineering the interlayer exchange coupling in magnetic trilayers," *Scientific Reports*, vol. 5, 2015.

127

[9] P. Bruno, Y. Suzuki, and C. Chappert, "Magneto-optical Kerr effect in a paramagnetic overlay on a ferromagnetic substrate: A spin-polarized quantum size effect," *Phys. Rev. B*, vol. 53, no. 14, p. 9214, 1996.

[10] S. Manna, M. Przybylski, D. Sander, and J. Kirschner, "The role of electron confinement in Pd films for the oscillatory magnetic anisotropy in an adjacent Co layer," *Journal of Physics: Condensed Matter*, vol. 28, no. 45, p. 456001, 2016.

[11] Z. Yao, X. Tian, L. Jiang, H. Hao, G. Zhang, S. Wu, Z. Zhao, and N. Gerile, "Influences of rare earth element Ce-doping and melt-spinning on microstructure and magnetostriction of $Fe_{83}Ga_{17}$ alloy," *Journal of Alloys and Compounds*, vol. 637, pp. 431 – 435, 2015.

[12] W. Wu, J. Liu, and C. Jiang, "Tb solid solution and enhanced magnetostriction in $Fe_{83}Ga_{17}$ alloys," *Journal of Alloys and Compounds*, vol. 622, pp. 379 – 383, 2015.

[13] H. L. Zhuang, P. R. C. Kent, and R. G.vHennig, "Strong anisotropy and magnetostriction in the two-dimensional stoner ferromagnet Fe_3GeTe_2," *Phys. Rev. B*, vol. 93, p. 134407, Apr 2016.

[14] A. Zorko, M. Pregelj, M. Gomilsek, Z. Jaglicic, D. Pajic, M. Telling, I. Arcon, I. Mikulska, and M. Valant, "Strain-induced extrinsic high-temperature ferromagnetism in the Fe-doped hexagonal barium titanate," *Scientific Reports*, vol. 5, no. 7703, 2015.

[15] J. Heidler, M. Fechner, R. V. Chopdekar, J. Piamonteze, J. Dreiser, C. A. Jenkins, E. Arenholz, S. Rusponi, H. Brune, N. A. Spaldin, and F. Nolting, "Magnetoelectroelastic control of magnetism in an artificial multiferroic," *Phys. Rev. B*, vol. 94, p. 014401, Jul 2016.

[16] D. L. González, Y. Shirahata, B. V. de Wiele, K. J. A. Franke, A. Casiraghi, T. Taniyama, and S. van Dijken, "Electric-field-driven domain wall dynamics in perpendicularly magnetized multilayers," *AIP Advances*, vol. 7, no. 3, p. 035119, 2017.

[17] H.-C. Chang, S.-C. Liao, H.-S. Hsieh, J.-H. Wen, C.-H. Lai, and W. Fang, "Magnetostrictive type inductive sensing pressure sensor," *Sensors and Actuators A: Physical*, vol. 238, pp. 25 – 36, 2016.

[18] C. Yuan, J. Li, W. Zhang, X. Bao, and X. Gao, "Sharp goss orientation and large magnetostriction in the rolled columnar-grained Fe–Ga alloys," *Journal of Magnetism and Magnetic Materials*, vol. 374, pp. 459 – 462, 2015.

[19] J. H.-G. Ng, P. M. Record, X. Shang, K. L. Wlodarczyk, D. P. Hand, G. Schiavone, E. Abraham, G. Cummins, and M. P. Desmulliez, "Optimised co-electrodeposition of Fe–Ga alloys for maximum magnetostriction effect," *Sensors and Actuators A: Physical*, vol. 223, pp. 91 – 96, 2015.

[20] Y. N. Zhang and R. Q. Wu, "Large magnetostriction in Fe-based alloys predicted by density functional theory," *Phys. Rev. B*, vol. 82, pp. 224415–, Dec. 2010.

[21] R. Wu, "Origin of large magnetostriction in FeGa alloys," *Journal of Applied Physics*, vol. 91, no. 10, pp. 7358–7360, 2002.

[22] G. Wedler, J. Walz, A. Greuer, and R. Koch, "Stress dependence of the magnetoelastic coupling constants B1 and B2 of epitaxial Fe(001)," *Phys. Rev. B*, vol. 60, pp. R11313–R11316, Oct 1999.

[23] H. Szymczak, R. Żuberek, and J. Gonzalez, "Mechanisms responsible for magnetostriction in heterogeneous magnetic systems," *Journal of Magnetism and Magnetic Materials*, vol. 191, no. 1–2, pp. 199 – 202, 1999.

[24] T. Gutjahr-Loeser, D. Sander, and J. Kirschner, "Magnetoelastic Coupling in Ni and Fe monolayers on Cu (001)," *Journal of appplied physics*, vol. 87, p. 5920, 2000.

[25] M. Ciria, J. I. Arnaudas, A. del Moral, and R. C. O′Handley, "Magnetoelastic stress in Cu/Ni/Cu/Si(100) epitaxial thin films," *Phys. Rev. B*, vol. 70, p. 054431, Aug 2004.

[26] Z. Tian, D. Sander, and J. Kirschner, "Nonlinear magnetoelastic coupling of epitaxial layers of Fe, Co, and Ni on Ir(100)," *Phys. Rev. B*, vol. 79, p. 024432, Jan 2009.

[27] N. Ekreem, A. Olabi, T. Prescott, A. Rafferty, and M. Hashmi, "An overview of magnetostriction, its use and methods to measure these properties," *Journal of Materials Processing Technology*, vol. 191, no. 1–3, pp. 96 – 101, 2007. Advances in Materials and Processing Technologies, July 30th - August 3rd 2006, Las Vegas, Nevada.

[28] K. Dahmen, H. Ibach, and D. Sander, "A finite element analysis of the bending of crystalline plates due to anisotropic surface and film stress applied to magnetoelasticity," *Journal of Magnetism and Magnetic Materials*, vol. 231, no. 1, pp. 74 – 84, 2001.

[29] D. Sander and J. Kirschner, "Cantilever stress measurements of ferro-magnetic monolayers," *Applied Physics A*, vol. 87, pp. 419–425, Jun 2007.

[30] J. Premper, D. Sander, and J. Kirschner, "A combined surface stress and magneto-optical Kerr effect measurement setup for temperatures down to 30 K and in fields of up to 0.7 T," *Rev. Sci. Instrum.*, vol. 83, pp. 073904–1–073904–8, 2012.

[31] H. Zhang, C.-X. Liu, X.-L. Qi, X. Dai, Z. Fang, and S.-C. Zhang, "Topological insulators in Bi_2Se_3, Bi_2Te_3 and Sb_2Te_3 with a single dirac cone on the surface," *Nature Physics*, vol. 5, pp. 438–442, 2009.

[32] L. Miao, Z. F. Wang, W. Ming, M.-Y. Yao, M. Wang, F. Yang, Y. R. Song, F. Zhu, A. V. Fedorov, Z. Sun, C. L. Gao, C. Liu, Q.-K. Xue, C.-X. Liu, F. Liu, D. Qian, and J.-F. Jia, "Quasiparticle dynamics in reshaped helical dirac cone of topological insulators," *Proceedings of the National Academy of Sciences*, vol. 110, no. 8, pp. 2758–2762, 2013.

[33] F. Bonell, D. Lam, S. Yoshida, Y. Takahashi, Y. Shiota, S. Miwa, T. Nakamura, and Y. Suzuki, "Investigation of Au and Ag segregation on Fe(001) with soft X-ray absorption," *Surface Science*, vol. 616, pp. 125 – 130, 2013.

[34] J. E. Ortega, F. J. Himpsel, G. J. Mankey, and R. F. Willis, "Quantum-well states and magnetic coupling between ferromagnets through a noble-metal layer," *Phys. Rev. B*, vol. 47, pp. 1540–1552, Jan 1993.

[35] T. Berdot, A. Hallal, P. Dey, L. T. Bismaths, L. Joly, A. Bourzami, H. Bulou, F. Scheurer, J. Henk, M. Alouani, and W. Weber, "Influence of lattice relaxation on the electron-spin motion in ferromagnetic films: experiment and theory," pp. 81000Z–81000Z–12, 2011.

[36] L. T. Bismaths, L. Joly, F. Scheurer, and W. Weber, "Morphology- and quantum-size induced oscillations of the electron-spin precession in Fe films on Ag(001)," *IEEE Transactions on Magnetics*, vol. 44, pp. 2879–2882, Nov 2008.

[37] L. T. Bismaths, L. Joly, A. Bourzami, F. Scheurer, and W. Weber, "Morphology-induced oscillations of the electron-spin precession in Fe films on Ag(001)," *Phys. Rev. B*, vol. 77, p. 220405, Jun 2008.

[38] R. Opitz, S. Loebus, A. Thissen, and R. Courths, "An angle-scanned photoelectron diffraction (XPD) study of the growth and structure of ultrathin Fe films on Au (001)," *Surface Science*, vol. 370, p. 293, 1997.

[39] M. M. J. Bischoff, T. Yamada, A. J. Quinn, R. G. P. van der Kraan, and H. van Kempen, "Direct observation of surface alloying and interface roughening: Growth of Au on Fe(001)," *Phys. Rev. Lett.*, vol. 87, p. 246102, Nov 2001.

[40] R. Belkhou, R. Flamminia, M. Marsib, A. Taleb-Ibrahimia, L. Gregorattib, A. Barinovb, and M. Kiskinova, "Role of gold segregation in the growth mode and the morphology of Fe/Au(001) magnetic thin films," *Surface Science*, vol. 532, p. 63, 2003.

[41] V. Blum, C. Rath, S. Müller, L. Hammer, K. Heinz, J. M. García, J. E. Ortega, J. E. Prieto, O. S. Hernán, J. M. Gallego, A. L. V. de Parga, and R. Miranda, "Fe thin-film growth on Au(100): A self-surfactant effect and its limitations," *Phys. Rev. B*, vol. 59, pp. 15966–15974, Jun 1999.

[42] D. W. Ślęzak, K. Freindl, A. Kozioł, K. Matlak, M. Rams, N. Spiridis, M. Ślęzak, T. Ślęzak, M. Zając, and J. Korecki, "Thickness-driven polar spin reorientation transition in ultrathin Fe/Au(001) films," *Phys. Rev. B*, vol. 81, p. 064421, Feb 2010.

[43] J. Korecki, M. Kubiak, T. Ślęzak, and N. Spiridis, "From monoatomic multilayers to ordered alloys," *Acta Physica Polonica. Series A*, vol. 97, p. 129, 2000.

[44] J. Gřondilová, M. Rickart, J. Mistrík, K. Postava, Š. Višňovský, T. Yamaguchi, R. Lopušník, S. O. Demokritov, and B. Hillebrands, "Anisotropy of magneto-optical spectra in ultrathin Fe/Au/Fe bilayers," *Journal of Applied Physics*, vol. 91, no. 10, pp. 8246–8248, 2002.

[45] L. Uba, S. Uba, V. N. Antonov, A. N. Yaresko, T. Ślęzak, and J. Korecki, "Magneto-optical anisotropy study of Fe_n/Au_n superlattices," *Phys. Rev. B*, vol. 62, pp. 13731–13747, Nov 2000.

[46] Y. Suzuki, T. Katayama, P. Bruno, S. Yuasa, and E. Tamura, "Oscillatory magneto-optical effect in a Au (001) film deposited on Fe: Experimental confirmation of a spin-polarized quantum size effect," *Phys. Rev. Lett.*, vol. 80, pp. 5200–5203, Jun 1998.

[47] S. Manna, P. L. Gastelois, M. Dąbrowski, P. Kuswik, M. Cinal, M. Przybylski, and J. Kirschner, "Effect of quantum well states in Cu overlayer on magnetic anisotropy of Fe and Co films revisited," *Phys. Rev. B*, vol. 87, p. 134401, Apr 2013.

[48] J. Gibbs, *The scientifis papers of J. Willard Gibbs.* Dover, 1961.

[49] D. Sander and H. Ibach, *4.4 Surface free energy and surface stress*, pp. 303–312. Berlin, Heidelberg: Springer Berlin Heidelberg, 2002.

[50] H. Ibach, "The role of surface stress in reconstruction, epitaxial growth and stabilization of mesoscopic structures," *Surface Science Reports*, vol. 29, pp. 195–263, 1997.

[51] D. Sander, "The correlation between mechanical stress and magnetic anisotropy in ultrathin films," *Reports on Progress in Physics*, vol. 62, no. 5, p. 809, 1999.

[52] D. Sander, Z. Tian, and J. Kirschner, "The role of surface stress in structural transitions, epitaxial growth and magnetism on the nanoscale," *Journal of Physics: Condensed Matter*, vol. 21, no. 13, p. 134015, 2009.

[53] D. Sander, Z. Tian, and J. Kirschner, "Cantilever measurements of surface stress, surface reconstruction, film stress and magnetoelastic stress of monolayers.," *Sensors (Basel, Switzerland)*, vol. 8, p. 4466, 2008.

[54] H. Li, Y. S. Li, J. Quinn, D. Tian, J. Sokolov, F. Jona, and P. M. Marcus, "Quantitative low-energy electron-diffraction study of the epitaxy of Fe on Ag(001): Questions about the growth mode," *Phys. Rev. B*, vol. 42, pp. 9195–9198, Nov. 1990.

[55] G. Smith, H. Padmore, and C. Norris, "The growth of Fe overlayers on Ag(100)," *Surface Science*, vol. 119, pp. L287–L291, July 1982.

[56] M. Canepa, S. Terreni, P. Cantini, A. Campora, and L. Mattera, "Initial growth morphology in a heteroepitaxial system at low temperature: Fe on Ag(100)," *Phys. Rev. B*, vol. 56, pp. 4233–4242, Aug. 1997.

[57] P. J. Schurer, Z. Celinski, and B. Heinrich, "Mössbauer investigation of the growth of the fe multilayer in Fe(100)/Ag(100) structures," *Phys. Rev. B*, vol. 51, pp. 2506–2514, Jan 1995.

[58] M. Canepa, E. Magnano, A. Campora, P. Cantini, M. Salvietti, and L. Mattera, "Diffusion by atomic place exchange in ultrathin iron films on Ag(100): an ion scattering spectroscopy study," *Surface Science*, vol. 352-354, no. 0, pp. 36 – 40, 1996. Proceedings of the 15th European Conference on Surface Science.

[59] I. Bézsi, C. Fetzer, I. Szűcs, B. Degroote, A. Vantomme, T. Kobayashi, and A. Nakanishi, "Ultrathin Fe layers on Ag (100) surface," *Surface Science*, vol. 601, pp. 2525–2531, June 2007.

[60] N. Spiridis and J. Korecki, "Influence of Au reconstruction on growth of Fe on Au(100)," *Applied Surface Science*, vol. 141, no. 3, pp. 313 – 318, 1999.

[61] Y.-L. He and G.-C. Wang, "Observation of atomic place exchange in submonolayer heteroepitaxial Fe/Au(001) films," *Phys. Rev. Lett.*, vol. 71, pp. 3834–3837, Dec 1993.

[62] A. M. Begley, S. K. Kim, J. Quinn, F. Jona, H. Over, and P. M. Marcus, "Growth of ultrathin films of Fe on Au(001)," *Phys. Rev. B*, vol. 48, pp. 1779–1785, Jul 1993.

[63] A. Cavallin, V. Sevriuk, K. N. Fischer, S. Manna, S. Ouazi, M. Ellguth, C. Tusche, H. L. Meyerheim, D. Sander, and J. Kirschner, "Preparation and characterization of Bi_2Se_3(0001) and of epitaxial FeSe nanocrystals on Bi_2Se_3(0001)," *Surface Science*, vol. 646, pp. 72 – 82, 2016. Surface science for heterogeneous catalysis, a special issue in Honour of Richard Lambert.

[64] E. W. Lee, "Magnetostriction and magnetomechanical effects," *Reports on Progress in Physics*, vol. 18, no. 1, p. 184, 1955.

[65] C. Kittel, "Physical Theory of Ferromagnetic Domains," *Rev. Mod. Phys.*, vol. 21, pp. 541–583, Oct 1949.

[66] Y. Zhang and R. Wu, "Mechanism of large magnetostriction of galfenol," *IEEE Transactions on Magnetics*, vol. 47, pp. 4044–4049, Oct 2011.

[67] M. Fähnle, M. Komelj, R. Q. Wu, and G. Y. Guo, "Magnetoelasticity of Fe: Possible failure of ab initio electron theory with the local-spin-density approximation and with the generalized-gradient approximation," *Phys. Rev. B*, vol. 65, p. 144436, Apr 2002.

[68] H. Ibach and H. Lueth, *Solid-State Physics: An Introduction to Principles of Materials Science.* Springer Berlin Heidelberg, 2009.

[69] É. Du Tremolet de Lacheisserie, *Magnetostriction: theory and applications of magnetoelasticity.* CRC Press, 1993.

[70] J.-P. Jay, F. L. Berre, S. Pogossian, and M. Indenbom, "Direct and inverse measurement of thin films magnetostriction," *Journal of Magnetism and Magnetic Materials*, vol. 322, no. 15, pp. 2203 – 2214, 2010.

[71] A. Hernando, M. Vázquez, V. Madurga, and H. Kronmüller, "Modification of the saturation magnetostriction constant after thermal treatments for the $Co_{58}Fe_5Ni_{10}B_{16}Si_{11}$ amorphous ribbon," *Journal of Magnetism and Magnetic Materials*, vol. 37, no. 2, pp. 161 – 166, 1983.

[72] M. Ciria, J. I. Arnaudas, A. del Moral, G. J. Tomka, de C. la Fuente, P. A. J. de Groot, M. R. Wells, and R. C. C. Ward, "Determination of magnetostrictive stresses in magnetic rare-earth superlattices by a cantilever method," *Phys. Rev. Lett.*, vol. 75, pp. 1634–1637, Aug 1995.

[73] D. Sander and J. Kirschner, "Non-linear magnetoelastic coupling in monolayers: Experimental challenges and theoretical insights," *Phys. Status Solidi B*, vol. 248, no. 10, pp. 2389–2397, 2011.

[74] L. Benito, C. Ballesteros, and R. C. C. Ward, "In-plane uniaxial magnetic anisotropy induced by anisotropic strain relaxation in high lattice-mismatched Dy/Sc superlattices," *Phys. Rev. B*, vol. 89, p. 134421, Apr 2014.

[75] H. Szymczak and R. Żuberek, "Surface magnetostriction," *Acta Physica Polonica A*, vol. 83, p. 651, 1993.

[76] T. Gutjahr-Loeser, D. Sander, and J. Kirschner, "Magnetoelastic coupling in Co thin films on W (001)," *Journal of Magnetism and Magnetic Materials*, vol. 220, pp. L1–L7, 2000.

[77] G. Wedler, J. Walz, A. Greuer, and R. Koch, "The magnetoelastic coupling constant B2 of epitaxial Fe(001) films," *Surface Science*, vol. 454-456, no. 0, pp. 896 – 899, 2000.

[78] P. M. Shepley, A. W. Rushforth, M. Wang, G. Burnell, and T. A. Moore, "Modification of perpendicular magnetic anisotropy and domain wall velocity in Pt/Co/Pt by voltage-induced strain," *Scientific Reports*, vol. 5, no. 7921, 2015.

[79] I. Lucas, D. Ciudad, M. Plaza, S. Ruiz-Gómez, C. Aroca, and L. Pérez, "Assessment of layer thickness and interface quality in CoP electrodeposited multilayers," *ACS Applied Materials and Interfaces*, vol. 8, no. 29, pp. 18930–18934, 2016. PMID: 27381897.

[80] H. L. Gall, J. B. Youssef, N. Tiercelin, V. Preobrazhsensky, P. Pernod, and J. Ostorero, "Giant magnetostriction of exchange-coupled (TbFe/Fe) ML with high sensitivity after heat treatment," *IEEE Transactions on Magnetics*, vol. 37, pp. 2699–2701, Jul 2001.

[81] C. de la Fuente, J. I. Arnaudas, M. Ciria, A. del Moral, C. Dufour, and K. Dumesnil, "Magnetic and magnetoelastic properties of epitaxial SmFe$_2$ thin film," *Journal of Physics: Condensed Matter*, vol. 22, no. 4, p. 046004, 2010.

[82] J. Liu, C. Jiang, and H. Xu, "Giant magnetostrictive materials," *Science China Technological Sciences*, vol. 55, no. 5, pp. 1319–1326, 2012.

[83] H. D. Chopra and M. Wuttig, "Non-joulian magnetostriction," *Nature*, vol. 521, p. 430, 2015.

[84] A. Khachaturyan and D. Viehland, "Structurally heterogeneous model of extrinsic magnetostriction for Fe-Ga and similar magnetic alloys: Part I. decomposition and confined displacive transformation," *Metallurgical and Materials Transactions A*, vol. 38, no. 13, pp. 2308–2316, 2007.

[85] D. Hunter, W. Osborn, K. Wang, N. Kazantseva, J. Hattrick-Simpers, R. Suchoski, R. Takahashi, M. L. Young, A. Mehta, L. A. Bendersky, S. E. Lofland, M. Wuttig, and I. Takeuchi, "Giant magnetostriction in annealed Co$_{1-x}$Fe$_x$ thin-films," *Nature Communications*, vol. 2, no. 518, 2011.

[86] H. Wang, Y. N. Zhang, R. Q. Wu, L. Z. Sun, D. S. Xu, and Z. D. Zhang, "Understanding strong magnetostriction in Fe$_{100-x}$Ga$_x$ alloys," *Scientific Reports*, vol. 3, no. 3521, 2013.

[87] O. M. Chumak, A. Nabialek, R. Zuberek, I. Radelytskyi, T. Yamamoto, T. Seki, K. Takanashi, L. T. Baczewski, and H. Szymczak, "Magnetoelastic properties of epitaxially grown Co$_2$Fe$_{0.4}$Mn$_{0.6}$Si and Co$_2$FeGa$_{0.5}$Ge$_{0.5}$ heusler alloys thin films," *IEEE Transactions on Magnetics*, vol. PP, no. 99, pp. 1–1, 2017.

135

[88] D. Apalkov, B. Dieny, and J. M. Slaughter, "Magnetoresistive random access memory," *Proceedings of the IEEE*, vol. 104, pp. 1796–1830, Oct 2016.

[89] P. Bruno, "Theory of interlayer exchange interactions in magnetic multilayers," *Journal of Physics: Condensed Matter*, vol. 11, no. 48, p. 9403, 1999.

[90] S. S. P. Parkin, "Systematic variation of the strength and oscillation period of indirect magnetic exchange coupling through the 3d, 4d, and 5d transition metals," *Phys. Rev. Lett.*, vol. 67, pp. 3598–3601, Dec 1991.

[91] S. S. P. Parkin, N. More, and K. P. Roche, "Oscillations in exchange coupling and magnetoresistance in metallic superlattice structures: Co/Ru, Co/Cr, and Fe/Cr," *Phys. Rev. Lett.*, vol. 64, pp. 2304–2307, May 1990.

[92] A.Fert and P. Bruno, *Ultrathin Magnetic Structures II: Measurement Techniques and Novel Magnetic Properties*. Springer-Verlag, 2005.

[93] P. Bruno, "Theory of interlayer magnetic coupling," *Phys. Rev. B*, vol. 52, pp. 411–439, Jul 1995.

[94] S. Amasaki, M. Tokunaga, K. Sano, K. Fukui, K. Kodama, and N. Hosoito, "Induced spin polarization in the Au layers of Fe/Au multilayer in an antiparallel alignment state of Fe magnetizations by resonant X-ray magnetic scattering at the Au L3 absorption edge," *Journal of the Physical Society of Japan*, vol. 84, no. 6, p. 064704, 2015.

[95] X. Jiang, Z. Li, Y. Zheng, C. Kaiser, Z. Diao, J. Fang, and Q. Leng, "Modulation of interlayer exchange coupling strength in magnetic tunnel junctions via strain effect," *AIP Advances*, vol. 5, no. 9, p. 097221, 2015.

[96] B. Heinrich and J. Cochran, "Ultrathin metallic magnetic films: magnetic anisotropies and exchange interactions," *Advances in Physics*, vol. 42, no. 5, pp. 523–639, 1993.

[97] A. Fuss, S. Demokritov, P. Grünberg, and W. Zinn, "Short- and long period oscillations in the exchange coupling of Fe across epitaxially grown Al- and Au-interlayers," *Journal of Magnetism and Magnetic Materials*, vol. 103, no. 3, pp. L221 – L227, 1992.

136

[98] S. O. Demokritov, "Biquadratic interlayer coupling in layered magnetic systems," *J. Phys. D: Appl. Phys.*, vol. 31, p. 925, 1998.

[99] E. D. Hansen, T. Miller, and T.-C. Chiang, "Quantum-well or bulklike behaviour of Cu layers on Co," *Journal of Physics: Condensed Matter*, vol. 9, no. 32, p. L435, 1997.

[100] Z. Q. Qiu and N. V. Smith, "Quantum well states and oscillatory magnetic interlayer coupling," *Journal of Physics: Condensed Matter*, vol. 14, no. 8, p. R169, 2002.

[101] K. Medjanik, O. Fedchenko, S. Chernov, D. Kutnyakhov, M. Ellguth, A. Oelsner, B. Schönhense, T. R. F. Peixoto, P. Lutz, C.-H. Min, F. Reinert, S. Däster, Y. Acremann, J. Viefhaus, W. Wurth, H. J. Elmers, and G. Schönhense, "Direct 3D mapping of the Fermi surface and Fermi velocity," *nature materials*, vol. 16, p. 615, 2017.

[102] R. Hafner, D. Spisák, R. Lorenz, and J. Hafner, "Ab initio local-spin-density study of oscillatory exchange coupling in Fe/Au multilayers," *Journal of Physics: Condensed Matter*, vol. 14, no. 17, p. 4297, 2002.

[103] M. Dąbrowski, T. R. F. Peixoto, M. Pazgan, A. Winkelmann, M. Cinal, T. Nakagawa, Y. Takagi, T. Yokoyama, F. Bisio, U. Bauer, F. Yildiz, M. Przybylski, and J. Kirschner, "Oscillations of the orbital magnetic moment due to d-band quantum well states," *Phys. Rev. Lett.*, vol. 113, p. 067203, Aug 2014.

[104] J. Unguris, R. J. Celotta, and D. T. Pierce, "Oscillatory exchange coupling in Fe/Au/Fe(100)," *Journal of Applied Physics*, vol. 75, no. 10, pp. 6437–6439, 1994.

[105] J. Unguris, S.-H. Chung, and D. T. Pierce, "SEMPA imaging for spintronics applications," *AIP Conference Proceedings*, vol. 931, no. 1, pp. 472–476, 2007.

[106] J. Unguris, R. J. Celotta, and D. T. Pierce, "Determination of the exchange coupling strengths for Fe/Au/Fe," *Phys. Rev. Lett.*, vol. 79, pp. 2734–2737, Oct 1997.

[107] M. Schäfer, S. Demokritov, S. Müller-Pfeiffer, R. Schäfer, M. Schneider, P. Grünberg, and W. Zinn, "Investigation of 90° coupling in Fe/Ag/Fe structures: Loose spins and fluctuation mechanism," *Journal of Applied Physics*, vol. 77, no. 12, pp. 6432–6438, 1995.

137

[108] J. de Vries, G. Strijkers, M. Johnson, A. Reinders, and W. de Jonge, "Loose spins in Co/Cu(100)," *Journal of Magnetism and Magnetic Materials*, vol. 148, no. 1, pp. 187 – 188, 1995.

[109] U. Rücker, S. Demokritov, E. Tsymbal, P. Grünberg, and W. Zinn, "Biquadratic coupling in Fe/Au/Fe trilayers: Experimental evidence for the magnetic-dipole mechanism," *Journal of Applied Physics*, vol. 78, no. 1, pp. 387–391, 1995.

[110] B. Heinrich, J. F. Cochran, T. Monchesky, and R. Urban, "Exchange coupling through spin-density waves in Cr(001) structures: Fe-whisker/Cr/Fe(001) studies," *Phys. Rev. B*, vol. 59, pp. 14520–14532, Jun 1999.

[111] D. Pierce, J. Unguris, R. Celotta, and M. Stiles, "Effect of roughness, frustration, and antiferromagnetic order on magnetic coupling of Fe/Cr multilayers," *Journal of Magnetism and Magnetic Materials*, vol. 200, no. 1–3, pp. 290 – 321, 1999.

[112] R. P. Erickson, K. B. Hathaway, and J. R. Cullen, "Mechanism for non-heisenberg-exchange coupling between ferromagnetic layers," *Phys. Rev. B*, vol. 47, pp. 2626–2635, Feb 1993.

[113] A. J. R. Ives, J. A. C. Bland, R. J. Hicken, and C. Daboo, "Oscillatory biquadratic coupling in Fe/Cr/Fe(001)," *Phys. Rev. B*, vol. 55, pp. 12428–12438, May 1997.

[114] Y. Roussigné, F. Ganot, C. Dugautier, P. Moch, and D. Renard, "Brillouin scattering in Co/Cu/Co and Co/Au/Co trilayers: Anisotropy fields and interlayer magnetic exchange," *Phys. Rev. B*, vol. 52, pp. 350–360, Jul 1995.

[115] B. Heinrich, Z. Celinski, L. X. Liao, M. From, and J. F. Cochran, ""loose spins" in Fe/Cu/Fe(001) structures," *Journal of Applied Physics*, vol. 75, no. 10, pp. 6187–6189, 1994.

[116] W. Ding, L. Calabri, X. Chen, K. M. Kohlhaas, and R. S. Ruoff, "Mechanics of crystalline boron nanowires," *Composites Science and Technology*, vol. 66, p. 1112, 2006.

[117] M. A. Hopcroft, W. D. Nix, and T. W. Kenny, "What is the young's modulus of silicon?," *Journal of Microelectromechanical Systems*, vol. 19, pp. 229–238, April 2010.

138

[118] E. M. L. L. Landau, *Theory of Elasticity, second, revised and enlarged Edition*, vol. Vol. 7 of *Course of Theoretical Physics*. Pergamon Press, 1970.

[119] W. Schnell, D. Gross, and W. Hauger, *Technische Mechanik*, vol. 2 of *Elastostatik*. Springer-Verlag 1985, 6 ed., 1998.

[120] B.-L. Huang and M. Kaviany, "Ab initio," *Phys. Rev. B*, vol. 77, p. 125209, Mar 2008.

[121] T. Pritz, "Measurement methods of complex poisson's ratio of viscoelastic materials," *Applied Acoustics*, vol. 60, no. 3, pp. 279 – 292, 2000.

[122] H. Koc, A. M. Mamedov, and E. Ozbay, "Structural, elastic, and electronic properties of topological insulators: Sb_2Te_3 and Bi_2Te_3," in *2013 Joint IEEE International Symposium on Applications of Ferroelectric and Workshop on Piezoresponse Force Microscopy (ISAF/PFM)*, pp. 41–44, July 2013.

[123] R. Mahesh, D. Sander, S. M. Zharkov, and J. Kirschner, "Stress and growth of Ag monolayers on a Fe(100) whisker," *Phys. Rev. B*, vol. 68, p. 045416, July 2003.

[124] C. Birleanu, M. Pustan, V. Merie, R. Müller, R. Voicu, A. Baracu, and S. Craciun, "Temperature effect on the mechanical properties of gold nano films with different thickness," *IOP Conference Series: Materials Science and Engineering*, vol. 147, no. 1, p. 012021, 2016.

[125] C. Davisson and L. H. Germer, "Diffraction of electrons by a crystal of nickel," *Phys. Rev.*, vol. 30, pp. 705–740, Dec 1927.

[126] H. W. Haak, G. A. Sawatzky, and T. D. Thomas, "Auger-photoelectron coincidence measurements in copper," *Phys. Rev. Lett.*, vol. 41, pp. 1825–1827, Dec 1978.

[127] G. D. Filippo, M. I. Trioni, G. Fratesi, F. O. Schumann, Z. Wei, C. H. Li, L. Behnke, S. Patil, J. Kirschner, and G. Stefani, "The LVV Auger line shape of sulfur on copper studied by Auger photoelectron coincidence spectroscopy," *Journal of Physics: Condensed Matter*, vol. 27, no. 8, p. 085003, 2015.

[128] W. S. M. Werner, W. Smekal, H. Störi, H. Winter, G. Stefani, A. Ruocco, F. Offi, R. Gotter, A. Morgante, and F. Tommasini,

"Emission-depth-selective Auger photoelectron coincidence spectroscopy," *Phys. Rev. Lett.*, vol. 94, p. 038302, Jan 2005.

[129] D. A. Arena, R. A. Bartynski, and S. L. Hulbert, "A method for determining intrinsic shapes of overlapping spectral lines in Auger-photoelectron coincidence spectroscopy," *Review of Scientific Instruments*, vol. 71, no. 4, pp. 1781–1787, 2000.

[130] T. E. Madey and J. T. J. Yates *Surf. Sci.*, vol. 63, p. 203, 1977.

[131] C. J. Jones and D. L. Kirk, "Some considerations of the limitations of the auger-depth-profiling technique as applied to silver metal and (100) surfaces of indium phosphide," *Journal of Physics D: Applied Physics*, vol. 12, no. 6, p. 837, 1979.

[132] E. R. Moog, C. Liu, S. D. Bader, and J. Zak, "Thickness and polarization dependence of the magnetooptic signal from ultrathin ferromagnetic films," *Phys. Rev. B*, vol. 39, pp. 6949–6956, Apr 1989.

[133] S. Bader, "Smoke," *Journal of Magnetism and Magnetic Materials*, vol. 100, no. 1, pp. 440 – 454, 1991.

[134] P. N. Argyres, "Theory of the Faraday and Kerr effects in ferromagnetics," *Phys. Rev.*, vol. 97, pp. 334–345, Jan 1955.

[135] Z. Q. Qiu and S. D. Bader, "Surface magneto-optic Kerr effect," *Review of Scientific Instruments*, vol. 71, no. 3, pp. 1243–1255, 2000.

[136] M. Parker, "The kerr magneto-optic effect (1876-1976)," *Physica B+C*, vol. 86, pp. 1171 – 1176, 1977.

[137] H. P. Oepen, C. M. Schneider, D. S. Chuang, C. A. Ballentine, and R. C. O'Handley, "Magnetic anisotropy in epitaxial fcc Co/Cu (1 1 13)," *Journal of Applied Physics*, vol. 73, no. 10, pp. 6186–6188, 1993.

[138] K. L. Dang, P. Veillet, G. Suran, and K. Ounadjela, "Study of induced uniaxial anisotropy in magnetic thin films by transverse susceptibility," *Journal of Applied Physics*, vol. 62, no. 8, pp. 3328–3330, 1987.

[139] D. Sander, "The magnetic anisotropy and spin reorientation of nanostructures and nanoscale films," *Journal of Physics: Condensed Matter*, vol. 16, no. 20, p. R603, 2004.

[140] W. Weber, R. Allenspach, and A. Bischof, "Determining magnetic an-isotropies from hysteresis loops," *Applied Physics Letters*, vol. 70, no. 4, pp. 520–522, 1997.

[141] W. Weber, C. H. Back, A. Bischof, C. Würsch, and R. Allenspach, "Morphology-induced oscillations of the magnetic anisotropy in ul-trathin Co films," *Phys. Rev. Lett.*, vol. 76, pp. 1940–1943, Mar 1996.

[142] W. Weber, A. Bischof, R. Allenspach, C. Würsch, C. Back, and D. Pes-cia, "Oscillatory magnetic anisotropy and quantum well states in Cu /Co /Cu(100) films," *Phys. Rev. Lett.*, vol. 76, pp. 3424–3427, Apr 1996.

[143] W. Wulfhekel, T. Gutjahr-Löser, F. Zavaliche, D. Sander, and J. Kirschner, "Relation between structure, stress, and magnetism in Co/W(001)," *Phys. Rev. B*, vol. 64, p. 144422, Sep 2001.

[144] S. Mallik, N. Chowdhury, and S. Bedanta, "Interplay of uniaxial and cubic anisotropy in epitaxial Fe thin films on MgO (001) substrate," *AIP Advances*, vol. 4, no. 9, p. 097118, 2014.

[145] K. Marre and H. Neddermeyer, "Growth of ordered thin films of NiO on Ag(100) and Au(111)," *Surface Science*, vol. 287, pp. 995 – 999, 1993.

[146] Y. Jiang, X. Liang, S. Ren, C.-L. Chen, L.-J. Fan, Y.-W. Yang, J.-M. Tang, and D.-A. Luh, "The growth of sulfur adlayers on Au(100)," *The Journal of Chemical Physics*, vol. 142, no. 6, p. 064708, 2015.

[147] O. Binnig, H. Rohrer, C. Gerber, and E. Stoll, "Real-space observation of the reconstruction of Au(100)," *Surface Science*, vol. 144, no. 2, pp. 321 – 335, 1984.

[148] D. Gibbs, B. M. Ocko, D. M. Zehner, and S. G. J. Mochrie, "Structure and phases of the Au(001) surface: In-plane structure," *Phys. Rev. B*, vol. 42, pp. 7330–7344, Oct 1990.

[149] J. de la Figuera, M. A. González, R. García-Martínez, J. M. Rojo, O. S. Hernán, A. L. V. de Parga, and R. Miranda, "STM characterization of extended dislocation configurations in Au(001)," *Phys. Rev. B*, vol. 58, pp. 1169–1172, Jul 1998.

[150] A. Trembulowicz, G. Ehrlich, and G. Antczak, "Surface diffusion of gold on quasihexagonal-reconstructed Au(100)," *Phys. Rev. B*, vol. 84, p. 245445, Dec 2011.

[151] J. Wendelken and D. Zehner, "Au(100): Characterization of reordered and normal surfaces via LEED, AES, and ELS," *Surface Science*, vol. 71, no. 1, pp. 178 – 184, 1978.

[152] T. W. Haas, J. T. Grant, and G. J.Dooley, "Auger-electron spectroscopy of transition metals," *Phys. Rev. B*, vol. 1, pp. 1449–1459, Feb 1970.

[153] M. Canepa, M. Salvietti, A. Campora, and L. Mattera, "Interdiffusion and segregation in the growth of thin Fe films on Ag(100): an ARUPS-MDS study," *Journal of Electron Spectroscopy and Related Phenomena*, vol. 76, pp. 471–476, Dec. 1995.

[154] M. Canepa, P. Cantini, O. Ricciardi, S. Terreni, and L. Mattera, "Temperature effects on morphology and composition of ultrathin heteroepitaxial films: Fe on Ag(100)," *Surface Science*, vol. 429, pp. 34–45, June 1999.

[155] S. D. Rossi and F. Ciccacci, "Interdiffusion at the FeAg(100) interface studied by spin-resolved IPES," *Surface Science*, vol. 307-309, Part A, pp. 496–500, Apr. 1994.

[156] D. E. Burgler, C. M. Schmidt, D. M. Schaller, F. Meisinger, R. Hofer, and H.-J. Güntherodt, "Optimized epitaxial growth of Fe on Ag(001)," *Phys. Rev. B*, vol. 56, pp. 4149–4158, Aug 1997.

[157] D. Kumar and A. Gupta, "Interface study of Ag/^{57}Fe/Ag trilayer using Mössbauer and X-ray standing wave analysis," *Hyperfine Interactions*, vol. 185, no. 1, pp. 29–32, 2008.

[158] G. Sharma, R. Gupta, D. Kumar, and A. Gupta, "Anomalous evolution of interfaces in Fe/Ag magnetic multilayer," *Journal of Physics D: Applied Physics*, vol. 46, no. 50, p. 505302, 2013.

[159] R. J. Hicken, S. J. Gray, A. Ercole, C. Daboo, D. J. Freeland, E. Gu, E. Ahmad, and J. A. C. Bland, "Magnetic anistropy in ultrathin epitaxial Fe/Ag(100) films with overlayers," *Phys. Rev. B*, vol. 55, pp. 5898–5907, Mar. 1997.

[160] B. Heinrich, S. T. Purcell, J. R. Dutcher, K. B. Urquhart, J. F. Cochran, and A. S. Arrott, "Structural and magnetic properties of ultrathin Ni/Fe bilayers grown epitaxially on Ag(001)," *Phys. Rev. B*, vol. 38, pp. 12879–12896, Dec. 1988.

[161] D. Briggs and M. Seah, *Practical Surface Analysis: Auger and X-ray photoelectron spectroscopy.* Practical Surface Analysis, Wiley, 1990.

[162] M. Salvietti, R. Moroni, M. Canepa, and L. Mattera, "Surface magnetism of Fe on Ag(100): a He-spin polarized study," *Journal of Electron Spectroscopy and Related Phenomena*, vol. 76, pp. 677–681, Dec. 1995.

[163] A. Hahlin, C. Andersson, J. H. Dunn, B. Sanyal, O. Karis, and D. Arvanitis, "Structure and magnetism of ultrathin epitaxial Fe on Ag(100)," *Phys. Rev. B*, vol. 73, p. 134423, Apr 2006.

[164] X.-D. Ma, T. Nakagawa, and T. Yokoyama, "Effect of surface chemisorption on the spin reorientation transition in magnetic ultrathin Fe film on Ag(001) ," *Surface Science*, vol. 600, no. 19, pp. 4605 – 4612, 2006.

[165] C. Sommers, J. Zabloudil, C. Uiberacker., P. Weinberger, and L. Szunyogh, "Multiple reorientation transition of the magnetization of free surfaces of Fe on Ag(100)," *Phys. Rev. B*, vol. 58, pp. 5539–5543, Sep 1998.

[166] Z. Q. Qiu, J. Pearson, and S. D. Bader, "Asymmetry of the spin reorientation transition in ultrathin Fe films and wedges grown on Ag(100)," *Phys. Rev. Lett.*, vol. 70, pp. 1006–1009, Feb. 1993.

[167] A. Hahlin, C. Andersson, J. H. Dunn, O. Karis, and D. Arvanitis, "Structure and magnetism on in situ ultrathin epitaxial films: XMCD and EXAFS on Fe/Ag(100)," *Surface Science*, vol. 532-535, pp. 76–81, 2003.

[168] M. Przybylski, M. Dąbrowski, U. Bauer, M. Cinal, and J. Kirschner, "Oscillatory magnetic anisotropy due to quantum well states in thin ferromagnetic films (invited)," *Journal of Applied Physics*, vol. 111, no. 7, p. 07C102, 2012.

[169] U. Bauer and M. Przybylski, "Large amplitude oscillation of magnetic anisotropy engineered by substrate step density," *Phys. Rev. B*, vol. 81, p. 134428, Apr 2010.

[170] M. Cinal, "Analysis of magnetocrystalline anisotropy oscillations in Co/Pd thin films," *Journal of Physics: Condensed Matter*, vol. 13, no. 5, p. 901, 2001.

[171] W. Geerts, Y. Suzuki, T. Katayama, K. Tanaka, K. Ando, and S.Yoshida, "Thickness-dependent oscillation of the magneto-optical properties of Au-sandwiched (001) Fe films," *Phys. Rev. B*, vol. 50, pp. 12581–12586, Nov 1994.

[172] L. M. Sandratskii, "Correlated oscillations of the magnetic anisotropy energy and orbital moment anisotropy in thin films: The role of quantum well states," *Phys. Rev. B*, vol. 92, p. 134414, Oct 2015.

[173] O. Hernán, A. V. de Parga, J. Gallego, and R. Miranda, "Self-surfactant effect on Fe/Au(100): place exchange plus Au self-diffusion," *Surface Science*, vol. 415, no. 1–2, pp. 106 – 121, 1998.

[174] Kaye and Laby, "Tables of physical and chemical constants 16th edition," 1995.

[175] P. Estrup and E. McRae, "Surface studies by electron diffraction," *Surface Science*, vol. 25, no. 1, pp. 1 – 52, 1971.

[176] M. Brockmann, S. Miethaner, R. Onderka, M. Köhler, F. Himmelhuber, H. Regensburger, F. Bensch, T. Schweinböck, and G. Bayreuther, "In-plane spin reorientation transition in ultrathin epitaxial Fe(001) films," *Journal of Applied Physics*, vol. 81, no. 8, pp. 5047–5049, 1997.

[177] Y.-L. He and G.-C. Wang, "Roughness dependent magnetic hysteresis of a few monolayer thick Fe films on Au(001)," *Journal of Applied Physics*, vol. 76, no. 10, pp. 6446–6448, 1994.

[178] C. Liu and S. D. Bader, "Perpendicular surface magnetic anisotropy in ultrathin epitaxial Fe films," *Journal of Vacuum Science & Technology A: Vacuum, Surfaces, and Films*, vol. 8, no. 3, pp. 2727–2731, 1990.

[179] I. Reichl, A. Vernes, P. Weinberger, L. Szunyogh, and C. Sommers, "Reorientation transition in fe_n/Au(100)," *Phys. Rev. B*, vol. 71, p. 214416, Jun 2005.

[180] E. Taglauer, "Surface cleaning using sputtering," *Applied Physics A*, vol. 51, no. 3, pp. 238–251, 1990.

[181] M. A. Makeev, R. Cuerno, and A.-L. Barabási, "Morphology of ion-sputtered surfaces," *Nuclear Instruments and Methods in Physics Research Section B: Beam Interactions with Materials and Atoms*, vol. 197, no. 3–4, pp. 185 – 227, 2002.

[182] L. S. Dake, D. E. King, J. R. Pitts, and A. W. Czanderna, *Ion Beam Bombardment Effects on Solid Surfaces at Energies Used for Sputter Depth Profiling*, pp. 97–274. Boston, MA: Springer US, 2002.

[183] K. Dahmen, M. Giesen, J. Ikonomov, K. Starbova, and H. Ibach, "Steady-state surface stress induced in noble gas sputtering," *Thin Solid Films*, vol. 428, no. 1–2, pp. 6 – 10, 2003. Proceedings of Symposium J on Growth and Evolution of Ultrathin Films: Surface and Interface Geometric and Electronic Structure, of the E-MRS Spring Conference.

[184] J. Opitz, P. Zahn, J. Binder, and I. Mertig, "Interlayer exchange coupling in Fe/Au multilayers," *Journal of Applied Physics*, vol. 87, no. 9, pp. 6588–6590, 2000.

[185] C. E. Bach, M. Giesen, H. Ibach, and T. L. Einstein, "Stress relief in reconstruction," *Phys. Rev. Lett.*, vol. 78, pp. 4225–4228, Jun 1997.

[186] T. L. Monchesky, A. Enders, R. Urban, K. Myrtle, B. Heinrich, X.-G. Zhang, W. H. Butler, and J. Kirschner, "Spin-dependent transport in Fe and Fe/Au multilayers," *Phys. Rev. B*, vol. 71, p. 214440, Jun 2005.

[187] H. P. Oepen, Y. T. Millev, H. F. Ding, S. Pütter, and J. Kirschner, "Field-driven reorientation in ultrathin ferromagnetic films with uniaxial anisotropy," *Phys. Rev. B*, vol. 61, pp. 9506–9512, Apr 2000.

[188] S. Sakshath, S. V. Bhat, P. S. A. Kumar, D. Sander, and J. Kirschner, "Enhancement of uniaxial magnetic anisotropy in Fe thin films grown on GaAs(001) with an MgO underlayer," *Journal of Applied Physics*, vol. 109, no. 7, p. 07C114, 2011.

[189] A. Polyakov, H. L. Meyerheim, E. D. Crozier, R. A. Gordon, K. Mohseni, S. Roy, A. Ernst, M. G. Vergniory, X. Zubizarreta, M. M. Otrokov, E. V. Chulkov, and J. Kirschner, "Surface alloying and iron selenide formation in Fe/Bi_2Se_3(0001) observed by X-ray absorption fine structure experiments," *Phys. Rev. B*, vol. 92, p. 045423, Jul 2015.

[190] W. Zhang, Z. Li, F. Li, H. Zhang, J. Peng, C. Tang, Q. Wang, K. He, X. Chen, L. Wang, X. Ma, and Q.-K. Xue, "Interface charge doping effects on superconductivity of single-unit-cell FeSe films on $SrTiO_3$ substrates," *Phys. Rev. B*, vol. 89, p. 060506, Feb 2014.

[191] C.-L. Song, Y.-L. Wang, Y.-P. Jiang, Z. Li, L. Wang, K. He, X. Chen, X.-C. Ma, and Qi-KunvXue, "Molecular-beam epitaxy and robust

superconductivity of stoichiometric FeSe crystalline films on bilayer graphene," *Phys. Rev. B*, vol. 84, p. 020503, Jul 2011.

[192] S. Margadonna, Y. Takabayashi, M. T. McDonald, K. Kasperkiewicz, Y. Mizuguchi, Y. Takano, A. N. Fitch, E. Suard, and K. Prassides, "Crystal structure of the new $FeSe_{1-x}$ superconductor," *Chem. Commun.*, pp. 5607–5609, 2008.

[193] F.-C. Hsu, J.-Y. Luo, K.-W. Yeh, T.-K. Chen, T.-W. Huang, P. M. Wu, Y.-C. Lee, Y.-L. Huang, Y.-Y. Chu, D.-C. Yan, and M.-K. Wu, "Superconductivity in the PbO-type structure α-FeSe," *Proceedings of the National Academy of Sciences*, vol. 105, no. 38, pp. 14262–14264, 2008.

[194] S. Chandra and A. Islam, "Elastic properties of mono- and poly-crystalline PbO-type $FeSe_{1-x}Te_x$ (x = 0–1.0): A first-principles study," *Physica C: Superconductivity*, vol. 470, no. 22, pp. 2072 – 2075, 2010.

[195] P. Gumbsch and M. S. Daw, "Interface stresses and their effects on the elastic moduli of metallic multilayers," *Phys. Rev. B*, vol. 44, pp. 3934–3938, Aug 1991.

[196] G. J. Ackland, G. Tichy, V. Vitek, and M. W. Finnis, "Simple n-body potentials for the noble metals and nickel," *Philosophical Magazine A*, vol. 56, no. 6, pp. 735–756, 1987.

[197] S. Schönecker, S. K. Kwon, B. Johansson, and L. Vitos, "Surface parameters of ferritic iron-rich Fe–Cr alloy," *Journal of Physics: Condensed Matter*, vol. 25, no. 30, p. 305002, 2013.

[198] M. Punkkinen, Q.-M. Hu, S. Kwon, B. Johansson, J. Kollár, and L. Vitos, "Surface properties of 3d transition metals," *Philosophical Magazine*, vol. 91, no. 27, pp. 3627–3640, 2011.

[199] A. U. Nilekar, A. V. Ruban, and M. Mavrikakis, "Surface segregation energies in low-index open surfaces of bimetallic transition metal alloys," *Surface Science*, vol. 603, pp. 91–96, Jan. 2009.

[200] L. Vitos, A. Ruban, H. Skriver, and J. Kollár, "The surface energy of metals," *Surface Science*, vol. 411, no. 1, pp. 186 – 202, 1998.

[201] W. Tyson and W. Miller, "Surface free energies of solid metals: Estimation from liquid surface tension measurements," *Surface Science*, vol. 62, no. 1, pp. 267 – 276, 1977.

[202] L. Z. Mezey and J. Giber, "The surface free energies of solid chemical elements: Calculation from internal free enthalpies of atomization," *Japanese Journal of Applied Physics*, vol. 21, no. 11R, p. 1569, 1982.

[203] S. Schönecker, X. Li, B. Johansson, S. K. Kwon, and L. Vitos, "Thermal surface free energy and stress of iron," *Scientific Reports*, vol. 5, no. 14860, 2015.

[204] P. Błoński and A. Kiejna, "Structural, electronic, and magnetic properties of bcc iron surfaces," *Surface Science*, vol. 601, no. 1, pp. 123 – 133, 2007.

[205] M. J. Spencer, A. Hung, I. K. Snook, and I. Yarovsky, "Density functional theory study of the relaxation and energy of iron surfaces," *Surface Science*, vol. 513, no. 2, pp. 389 – 398, 2002.

[206] A. V. Ruban, H. L. Skriver, and J. K. Nørskov, "Surface segregation energies in transition-metal alloys," *Phys. Rev. B*, vol. 59, pp. 15990–16000, June 1999.

[207] A. Christensen, A. V. Ruban, P. Stoltze, K. W. Jacobsen, H. L. Skriver, J. K. Nørskov, and F. Besenbacher, "Phase diagrams for surface alloys," *Phys. Rev. B*, vol. 56, pp. 5822–5834, Sept. 1997.

[208] M. Langelaar and D. Boerma, "Fe adatoms on Ag(100): site exchange and mobility," *Surface Science*, vol. 395, no. 2, pp. 131 – 137, 1998.

[209] M. Salvietti, R. Moroni, M. Canepa, P. Ferro, and L. Mattera, "Thermal effects on the surface magnetism of a 10 ML Fe/Ag(100) film studied by spin polarized metastable deexcitation spectroscopy (SPMDS), journal = Journal of Magnetism and Magnetic Materials," vol. 165, pp. 230–233, Jan. 1997.

[210] K. Santhi, E. Thirumal, S. Karthick, H.-J. Kim, V. Narayanan, and A. Stephen, "Structural and magnetic investigations on metastable Ag-Fe nanophase alloy," *Journal of Alloys and Compounds*, vol. 557, pp. 172 – 178, 2013.

[211] R. Zong, S. Wen, F. Zeng, Y. Gao, C. Song, B. He, and F. Pan, "fcc solid solution alloy films formed in immiscible Fe-Ag system and their mechanical behaviors," *Applied Surface Science*, vol. 253, no. 6, pp. 2993 – 2998, 2007.

[212] Z. G. Li, H. Wan, J. Liu, A. Tsoukatos, G. C. Hadjipanayis, and L. Liang, "Microstructural investigation of granular Ag-Fe and Ag-Co thin films by atomic resolution and nanochemical analysis electron microscopy," *Applied Physics Letters*, vol. 63, no. 22, pp. 3011–3013, 1993.

[213] C. Alof, B. Stahl, M. Ghafari, and H. Hahn, "Interface contribution to giant magnetoresistance in granular AgFe studied with Mössbauer spectroscopy," *Journal of Applied Physics*, vol. 88, no. 7, pp. 4212–4215, 2000.

[214] J. Alonso, M. L. Fdez-Gubieda, G. Sarmiento, J. Chaboy, R. Boada, A. G. Prieto, D. Haskel, M. A. Laguna-Marco, J. C. Lang, C. Meneghini, L. F. Barquín, T. Neisius, and I. Orue, "Interfacial magnetic coupling between Fe nanoparticles in Fe-Ag granular alloys," *Nanotechnology*, vol. 23, no. 2, p. 025705, 2012.

[215] J. M. Soares, J. H. de Araújo, F. A. O. Cabral, T. Dumelow, F. L. A. Machado, and A. E. P. de Araújo, "Giant magnetoimpedance in FeAg granular alloys," *Applied Physics Letters*, vol. 80, no. 14, pp. 2532–2534, 2002.

[216] H. Krebs, M. Störmer, S. Fähler, O. Bremert, M. Hamp, A. Pundt, H. Teichler, W. Blum, and T. Metzger, "Structural properties of laser deposited metallic alloys and multilayers," *Applied Surface Science*, vol. 109, pp. 563 – 569, 1997.

[217] G. Chiaia, S. D. Rossi, L. Mazzolari, and F. Ciccacci, "Thin Fe films grown on Ag(100) studied by angle- and spin-resolved inverse-photoemission spectroscopy," *Phys. Rev. B*, vol. 48, pp. 11298–11304, Oct 1993.

[218] D. Sander, S. Ouazi, A. Enders, T. Gutjahrlöser, V. S. Stepanyuk, D. I. Bazhanov, and J. Kirschner, "Stress, strain and magnetostriction in epitaxial films," *Journal of Physics: Condensed Matter*, vol. 14, no. 16, p. 4165, 2002.

[219] W. Pan, D. Sander, M.-T. Lin, and J. Kirschner, "Stress oscillations and surface alloy formation during the growth of FeMn on Cu(001)," *Phys. Rev. B*, vol. 68, p. 224419, Dec 2003.

[220] P. W. Palmberg, *Handbook of Auger Electron Spectroscopy: A Reference Book of Standard Data for Identification and Interpretation of Auger Electron Spectroscopy Data*. Physical Electronics Industries, 1972.

[221] K. Takanashi, S. Mitani, M. Sano, H. Fujimori, H. Nakajima, and A. Osawa, "Artificial fabrication of an $l1_0$-type ordered FeAu alloy by alternate monatomic deposition," *Applied Physics Letters*, vol. 67, no. 7, pp. 1016–1018, 1995.

[222] D. Favez, J.-D. Wagniére, and M. Rappaz, "Au-Fe alloy solidification and solid-state transformations," *Acta Materialia*, vol. 58, no. 3, pp. 1016 – 1025, 2010.

[223] V. I. Gavrilenko and R. Wu, "Magneto-optical properties of FeAu alloys and Fe/Au superlattices," *Journal of Applied Physics*, vol. 85, no. 8, pp. 5112–5114, 1999.

[224] M. Sternik, K. Parlinski, and J. Korecki, "Fe_m/Au_n multilayers from first principles," *Phys. Rev. B*, vol. 74, p. 195405, Nov 2006.

[225] Q. Jiang, Y.-L. He, and G.-C. Wang, "Thermal stability and intermixing of ultrathin Fe films on a Au(001) surface," *Surface Science*, vol. 295, no. 1, pp. 197 – 212, 1993.

[226] T. Kawagoe, T. Kotaki, T. Shibasaki, Y. Ohmori, and A. Itoh, "The temperature-dependent growth of Fe submonolayer film on Au(001) studied by barrier height imaging using scanning tunneling microscopy," *Surface Science*, vol. 468, no. 1, pp. 1 – 9, 2000.

[227] P. Gospodaric, E. Mlynczak, M. Eschbach, M. Gehlmann, G. Zamborlini, V. Feyer, L. Plucinski, and C. M. Schneider, "Localized segregation of gold in ultra-thin Fe films on Au(001)." arXiv 1705.06464 Phys. Rev. B (accepted), 2018.

[228] H. Wormeester, E. Hüger, and E. Bauer, "Growth and electronic structure of thin epitaxial Pd and Co films on W(100)," *Phys. Rev. B*, vol. 54, pp. 17108–17117, Dec 1996.

[229] H. Wormeester, E. Hüger, and E. Bauer, "hcp and bcc Cu and Pd films," *Phys. Rev. Lett.*, vol. 77, pp. 1540–1543, Aug 1996.

[230] P. T. Sprunger, E. Lægsgaard, and F. Besenbacher, "Growth of Ag on Cu(100) studied by STM: From surface alloying to Ag superstructures," *Phys. Rev. B*, vol. 54, pp. 8163–8171, Sep 1996.

[231] J. E. Black, Z.-J. Tian, and T. S. Rahman, "Structure and dynamics of an Ag overlayer on Cu(100): a study using the embedded atom method," *Surface Science*, vol. 291, no. 1, pp. 215 – 225, 1993.

[232] S. Mróz and Z. Jankowski, "Properties of ultrathin silver films on the Ni(001) face," *Surface Science*, vol. 349, no. 2, pp. 111 – 118, 1996.

[233] D. Lucic, N. Cramer, R. Camley, Z. Celinski, P. Kabos, and C. Patton, "Influence of the interface morphology on the exchange coupling in Fe/Pd/Fe(001) structures," *Journal of Magnetism and Magnetic Materials*, vol. 198, pp. 418 – 420, 1999.

[234] V. Fiorentini, M. Methfessel, and M. Scheffler, "Reconstruction mechanism of fcc transition metal (001) surfaces," *Phys. Rev. Lett.*, vol. 71, pp. 1051–1054, Aug 1993.

[235] G. Boisvert and L. J. Lewis, "Self-diffusion on low-index metallic surfaces: Ag and Au (100) and (111)," *Phys. Rev. B*, vol. 54, pp. 2880–2889, Jul 1996.

[236] K. Pötting, W. Schmickler, and T. Jacob, "Self-diffusion on Au(100): A density functional theory study," *ChemPhysChem*, vol. 11, pp. 1395–1404, 5 2010.

[237] P. Bruno, "Tight-binding approach to the orbital magnetic moment and magnetocrystalline anisotropy of transition-metal monolayers," *Phys. Rev. B*, vol. 39, pp. 865–868, Jan 1989.

[238] P. G. Gowtham, G. M. Stiehl, D. C. Ralph, and R. A.Buhrman, "Thickness-dependent magnetoelasticity and its effects on perpendicular magnetic anisotropy in Ta/CoFeB/MgO thin films," *Phys. Rev. B*, vol. 93, p. 024404, Jan 2016.

[239] A. F. May, S. Calder, D. S. Parker, B. C. Sales, and M. A. McGuire, "Competing magnetic ground states and their coupling to the crystal lattice in $CuFe_2Ge_2$," *Scientific Reports*, vol. 6, no. 35325, 2016.

[240] X. Z. Lu, X. Wu, and H. J.Xiang, "General microscopic model of magnetoelastic coupling from first principles," *Phys. Rev. B*, vol. 91, p. 100405, Mar 2015.

[241] M. R. Ibarra, R. Mahendiran, C. Marquina, B. García-Landa, and J. Blasco, "Huge anisotropic magnetostriction in $La_{1-x}Sr_xCoO_{3-\delta}$ ($x > sim0.3$): Field-induced orbital instability," *Phys. Rev. B*, vol. 57, pp. R3217–R3220, Feb 1998.

[242] P. Blank and K. Wittmaack, "Energy and fluence dependence of the sputtering yield of silicon bombarded with argon and xenon," *Journal of Applied Physics*, vol. 50, no. 3, pp. 1519–1528, 1979.

[243] P. Blank and K. Wittmaack, "Implications in the use of sputtering for layer removal: the system Au on Si," *Radiation Effects*, vol. 43, no. 3, pp. 105–110, 1979.

[244] M. Murty, "Sputtering: the material erosion tool," *Surface Science*, vol. 500, no. 1, pp. 523 – 544, 2002.

[245] J. Fassbender, T. Strache, M. O. Liedke, D. Markó, S. Wintz, K. Lenz, A. Keller, S. Facsko, I. Möch, and J. McCord, "Introducing artificial length scales to tailor magnetic properties," *New Journal of Physics*, vol. 11, no. 12, p. 125002, 2009.

[246] S. S. Ahmad, W. He, Y.-S. Zhang, J. Tang, Y. Li, Q. Gul, X.-Q. Zhang, and Z.-H. Cheng, "Effect of Ar^+ beam sputtering on the magnetic anisotropy of Fe thin films deposited on the MgO(0 0 1) substrate," *Results in Physics*, vol. 7, pp. 1531 – 1535, 2017.

[247] K. Zhang, F. Rotter, M. Uhrmacher, C. Ronning, J. Krauser, and H. Hofsäss, "Ion induced nanoscale surface ripples on ferromagnetic films with correlated magnetic texture," *New Journal of Physics*, vol. 9, p. 29, 2007.

[248] D. Rosenberg and G. K. Wehner, "Sputtering yields for low energy He+, Kr+, and Xe+ ion bombardment," *Journal of Applied Physics*, vol. 33, no. 5, pp. 1842–1845, 1962.

[249] A. Mutzke and W. Eckstein, "Ion fluence dependence of the Si sputtering yield by noble gas ion bombardment," *Nuclear Instruments and Methods in Physics Research Section B: Beam Interactions with Materials and Atoms*, vol. 266, no. 6, pp. 872 – 876, 2008.

[250] P. Johnson, R. Thomson, and K. Reader, "TEM and SEM studies of radiation blistering in helium-implanted copper," *Journal of Nuclear Materials*, vol. 273, no. 2, pp. 117 – 129, 1999.

[251] G. J. Schrobilgen, "noble gas," *Encyclopaedia Britannica*, 2017.

[252] D. Sander, A. Enders, and J. Kirschner, "Magnetoelastic coupling and epitaxial misfit stress in ultrathin Fe(1 0 0)-films on W(1 0 0)," *Journal of Magnetism and Magnetic Materials*, vol. 198, p. 519, 1999.

[253] E. Młyńczak, M. Eschbach, S. Borek, J. Minár, J. Braun, I. Aguilera, G. Bihlmayer, S. Döring, M. Gehlmann, P. Gospodarič, S. Suga, L. Plucinski, S. Blügel, H. Ebert, and C. M. Schneider, "Fermi surface ma-

nipulation by external magnetic field demonstrated for a prototypical ferromagnet," *Phys. Rev. X*, vol. 6, p. 041048, Dec 2016.

[254] Y. I. Bespyatykh, I. E. Dikshtein, V. P. Malt́zev, and S. A. Nikitov, "Inhomogeneous magnetoelastic states and magnetoelastic wave spectrum in a system consisting of magnetic/nonmagnetic multilayers," *Phys. Rev. B*, vol. 68, p. 144421, Oct 2003.

[255] G. Y. Guo, "Magnetocrystalline anisotropy oscillations predicted in Fe/Au(001) superlattices," *Journal of Physics: Condensed Matter*, vol. 11, no. 22, p. 4329, 1999.

[256] C. M. Fang, R. A. de Groot, M. M. J. Bischoff, and H. van Kempen, "Oscillatory behavior of the magnetic moments of gold-covered iron surfaces," *Phys. Rev. B*, vol. 58, pp. 6772–6774, Sep 1998.

[257] M. K. Dąbrowski, *Effect of quantum well states on the magnetic anisotropy of ferromagnetic films*. PhD thesis, Halle, Univ., Naturwissenschaftliche Fakultät II, Diss., 2014, 2014.

[258] S. Crampin, "Fe on Au(100): magnetism and band formation," *Journal of Physics: Condensed Matter*, vol. 5, no. 27, p. 4647, 1993.

[259] M. Benoit, C. Langlois, N. Combe, H. Tang, and M.-J. Casanove, "Structural and electronic properties of the Au(001)/Fe(001) interface from density functional theory calculations," *Phys. Rev. B*, vol. 86, p. 075460, Aug 2012.

[260] Z. Celinski and B. Heinrich, "Exchange coupling in Fe/Cu, Pd, Ag, Au/Fe trilayers," *Journal of Magnetism and Magnetic Materials*, vol. 99, no. 1, pp. L25 – L30, 1991.

[261] J. Opitz, P. Zahn, J. Binder, and I. Mertig, "Ab initio," *Phys. Rev. B*, vol. 63, p. 094418, Feb 2001.

[262] S. M. Jaya, M. C. Valsakumar, and W. Nolting, "Interlayer exchange coupling in M/N/M multilayers," *Journal of Physics: Condensed Matter*, vol. 14, no. 17, p. 4355, 2002.

[263] M. Sternik and K. Parlinski, "First-principles studies of the interlayer exchange coupling in fine-layered Fe/Au multilayers," *Phys. Rev. B*, vol. 75, p. 212406, Jun 2007.

[264] J. X. Li, M. W. Jia, L. Sun, Z. Ding, B. L. Chen, and Y. Z. Wu, "Oscillatory anisotropic magnetoresistance arising from quantum well states in Au/Fe(001) bilayers," *IEEE Magnetics Letters*, vol. 6, pp. 1–4, 2015.

[265] H. Luetkens, J. Korecki, E. Morenzoni, T. Prokscha, M. Birke, H. Glückler, R. Khasanov, H.-H. Klauss, T. Ślezak, A. Suter, E. M. Forgan, C. Niedermayer, and F. J. Litterst, "Observation of the conduction electron spin polarization in the Ag spacer of a Fe/Ag/Fe trilayer," *Phys. Rev. Lett.*, vol. 91, p. 017204, Jul 2003.

[266] C. H. Back, W. Weber, C. Würsch, A. Bischof, D. Pescia, and R. Allenspach, "Magnetic anisotropy oscillations (invited)," *Journal of Applied Physics*, vol. 81, no. 8, pp. 5054–5057, 1997.

[267] H. Szymczak, M. Rewieński, and R. Żuberek, "Effect of roughness on the surface anisotropy and magnetostriction of magnetic multilayers," *Journal of Magnetism and Magnetic Materials*, vol. 139, no. 1, pp. 151 – 156, 1995.

[268] A. Yamaguchi, S. Ogu, W.-H. Soe, and R. Yamamoto, "Theory of the strain-induced magnetic anisotropy of transition metal-noble metal multilayers," *Applied Physics Letters*, vol. 62, no. 9, pp. 1020–1022, 1993.

[269] M. Stiles, *Interlayer Exchange Coupling*, pp. 99–142. Berlin, Heidelberg: Springer Berlin Heidelberg, 2005.

[270] P. Grünberg, J. Barnas, F. Saurenbach, J. Fuss, A. Wolf, and M. Vohl, "Layered magnetic structures: antiferromagnetic type interlayer coupling and magnetoresistance due to antiparallel alignment," *Journal of Magnetism and Magnetic Materials*, vol. 93, pp. 58 – 66, 1991.

[271] M. Belmeguenai, T. Martin, G. Woltersdorf, M. Maier, and G. Bayreuther, "Frequency- and time-domain investigation of the dynamic properties of interlayer-exchange-coupled $Ni_{81}Fe_{19}/Ru/Ni_{81}Fe_{19}$ thin films," *Phys. Rev. B*, vol. 76, p. 104414, Sep 2007.

[272] B. Heinrich, Z. Celinski, J. F. Cochran, A. S. Arrott, K. Myrtle, and S. T. Purcell, "Bilinear and biquadratic exchange coupling in bcc Fe/Cu/Fe trilayers: Ferromagnetic-resonance and surface magneto-optical Kerr-effect studies," *Phys. Rev. B*, vol. 47, pp. 5077–5089, Mar 1993.

[273] Y. Z. Wu, C. Y. Won, E. Rotenberg, H. W. Zhao, F. Toyoma, N. V. Smith, and Z. Q. Qiu, "Dispersion of quantum well states in Cu/Co/Cu(001)," *Phys. Rev. B*, vol. 66, p. 245418, Dec 2002.

Publications and conference contributions

Publications

1. A. Cavallin, V. Sevriuk, K. Novakoski Fischer, S. Manna, S. Ouazi, M. Ellguth, C. Tusche, H. L. Meyerheim, D. Sander, and J. Kirschner, "Preparation and characterization of $Bi_2Se_3(0001)$ and of epitaxial FeSe nanocrystals on $Bi_2Se_3(0001)$", *Surface Science*, vol. 646, p. 72, 2016.

2. K. Novakoski Fischer, L. Sandratskii, and D. Sander, "The influence of QWS on the magnetoelastic coupling of a trilayer system". In preparation.

3. K. Novakoski Fischer, and D. Sander, "Stress change as a signature of surface reconstruction." In preparation.

Conference contribution

1. K. Novakoski Fischer, S. Ouazi, A. Cavallin, V. Sevriuk, D. Sander, and J. Kirschner, "Fe-induced stress on $Bi_2Se_3(0001)$ ", Talk, Deutschen Physikalischen Gesellschaft (DPG), 2015, Berlin, Germany.

2. K. Novakoski Fischer, D. Sander, and J. Kirschner, "Non bulk-like magnetoelastic coupling in Fe monolayers on Ag(001) ", Talk, Deutschen Physikalischen Gesellschaft (DPG), 2015, Berlin, Germany.

3. K. Novakoski Fischer, S. Ouazi, D. Sander, and J. Kirschner, "Structure and induced stress of Fe on $Bi_2Se_3(0001)$ ", Talk, International Workshop on Topological Structures in Ferroic Materials (TOPO), 2015, Sydney, Australia.

4. K. Novakoski Fischer, S. Ouazi, D. Sander, and J. Kirschner, "Structure and induced stress of Fe on $Bi_2Se_3(0001)$ ", Poster, 20th International Conference on Magnetism (ICM), 2015, Barcelona, Spain.

5. K. Novakoski Fischer, D. Sander, and J. Kirschner, "Interfacial intermixing of Fe on Ag (001) and the impact on magnetoelastic coupling", Poster, 22nd International Colloquium on Magnetic Films and Surfaces (ICMFS), Cracow, Poland.

6. K. Novakoski Fischer, D. Sander, and J. Kirschner, " Epitaxial growth of Fe on Ag (001) and magnetoelastic coupling in Fe", Talk, Deutschen Physikalischen Gesellschaft (DPG), 2016, Regensburg, Germany.

7. K. Novakoski Fischer, and D. Sander, "Impact of Au interlayer on magnetoelasticity of Fe/Au/Fe sandwiches", Talk, Deutschen Physikalischen Gesellschaft (DPG), 2017, Dresden, Germany.

8. K. Novakoski Fischer, D. Sander, and S. Parkin, "Impact of Au interlayer on magnetoelasticity of Fe/Au/Fe trilayer", Talk, MMM Conference, 2017, Pittsburg, USA.

Acknowledgments

Curriculum vitae

Personal details

Name:	Kenia Novakoski Fischer
Date of birth:	16 September 1986
Sex:	Female
Place of birth:	Criciuma (SC), Brazil
Nationality:	Brazilian
Marital status:	Married
Present address:	Graseweg 1, 06108, Halle (Saale), Germany
Email:	kfischer@mpi-halle.mgp.de

Education

08/2014 – present	Doctoral Fellow at Max Planck Institute of Microstructure Physics, Halle, Germany
03/2012 – 09/2014	Master in Physics of Condensed Matter, Santa Catarina Federal University, Florianopolis, Brazil. Title thesis: *Study of growth and magneto-elastic properties of thin films of Fe on Ag.*
01/2009 – 09/2011	Physics Licenciate, Santa Catarina Federal University, Florianopolis, Brazil

Erklärung an Eides statt

Hiermit erkläre ich, dass ich die vorliegende Arbeit selbstständig und ohne fremde Hilfe verfasst, andere als die von mir angegebenen Quellen und Hilfsmittel nicht benutzt und die den benutzten Werken wörtlich oder inhaltlich entnommenen Stellen als solche kenntlich gemacht habe.

Eine Anmeldung der Promotionsabsicht habe ich an keiner anderen Fakultät einer Universität oder Hochschule beantragt.

Halle (Saale), 24.10.2017

Kenia Novakoski Fischer